Politecnico di Milano

SCHOOL OF INDUSTRIAL AND INFORMATION ENGINEERING

Master of Science – Energy Engineering

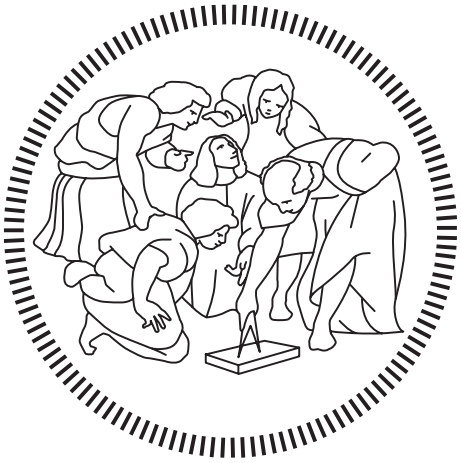

Dynamic modelling of a PEM Electrolysis System: optimal operation for coupling with Renewable Energy Sources

Supervisor

Prof. Giulio GUANDALINI

Co-Supervisor

Eng. Elena CRESPI

Candidate

Simone MOLHO – 928447

Academic Year 2020 – 2021

RINGRAZIAMENTI

Dedico questa tesi di laurea magistrale ai miei nonni Giulio e Dino Z"L, e al mio maestro spirituale Ariel. Da voi, che non vi siete mai stancati di rispondere alle mie domande e curiosità fin da quando ero bambino, ho ereditato la capacità di pensare in modo tecnico e scientifico.

Grazie al mio relatore e alla mia correlatrice, il Prof. Giulio Guandalini e l'Ing. Elena Crespi, mi ritengo infinitamente fortunato ad aver trovato persone come voi per lo svolgimento di questa tesi, con la vostra grande pazienza, fiducia e disponibilità. Desidero inoltre ringraziare tutte le persone che sono state supportive e mi sono state vicine con continuità, anche nei momenti più difficili, durante questo percorso fino al raggiungimento del traguardo, in particolare mia Mamma, mio Papà, Miriam e Sofia. Grazie a tutti i miei amici, che mi sono stati vicini e sono rimasti tali nonostante i miei lunghi silenzi.

Durante questo lavoro di tesi ho contemporaneamente cominciato un percorso lavorativo presso la En.It S.p.A. Qui ho avuto l'opportunità di cominciare ad avere un ruolo concreto nella transizione energetica e di toccare con mano il tema idrogeno, creando una potente sinergia tra tesi a lavoro, permettendo ad entrambi di beneficiare uno dell'altro. Desidero ringraziare Mattia e Salvatore per la fiducia datami, e per avermi permesso di conciliare il lavoro e lo studio con la vostra grande disponibilità ed umanità.

ABSTRACT

In a scenario of impressive growth in the installed capacity of electricity generation systems based on Renewable Energy Sources (RES), aiming at replacing the current carbon-intensive plants, the uncertainty and variability in the power generation is increasing, consequently requiring an increase in the flexibility of the power grid. Energy storage by means of hydrogen, produced from renewable power sources, could play a pivotal role in balancing inflexible or intermittent supply typical of these energy sources.
This work aims at finding and evaluating strategies for optimizing the operation of electrolyzers based on PEM technology when coupled with renewable energy sources, by exploiting a dynamic model of a PEM electrolyzer system.
In the first part of the work, an existing dynamic model of a PEM electrolyzer, realized in Simulink®, is improved, completed and validated. During this process, suggestions for the modelling of PEM electrolyzers are proposed. The model validation is carried out by using datasets from the operation of a 60 kW commercial unit tested at the University of California Irvine.
The second part regards the optimization of the system operation , with particular focus on the case of coupling with variable RES. The system properly follows dynamic loads and has fast start-ups. The optimization of the system startup revealed a potential increase in efficiency up to 13% in case of intermittent use. The system net efficiency is equal to 57% at full load, but drops significantly at partial load, with an efficiency of 27% at 20% of the rated power, mainly due to hydrogen losses in the drying system. The optimization of the use of this system led to an increase in efficiency at partial load up to 23%$_{pt.}$, while the optimization of the auxiliaries use carried an efficiency increase up to 12%$_{pt.}$. at partial load.
System operation at high pressure results to be the more convenient the higher the average load of use of the system. Hydrogen crossover and its dependence on pressure turned out to be a fundamental variable in the evaluation of high pressure performance, requiring further efforts in the modelling of this phenomenon.

KEYWORDS: electrolysis; PEM; simulation; optimization; hydrogen; renewable power

SOMMARIO

In un contesto di grandissima crescita della capacità rinnovabile installata, volta a sostituire gli attuali sistemi di generazione elettrica ad alta intensità di carbonio, l'incertezza e la variabilità della generazione di energia sono in aumento, richiedendo pertanto una maggiore flessibilità dei sistemi energetici.
L'immagazzinamento di energia mediante idrogeno prodotto da fonti di energia rinnovabile potrebbe svolgere un ruolo fondamentale nel bilanciare la produzione non programmabile ed intermittente tipica di queste fonti di energia.
Questo lavoro mira a trovare e valutare delle strategie per ottimizzare il funzionamento dei sistemi di elettrolisi basati su tecnologia PEM quando accoppiati a fonti di energia rinnovabile, sfruttando un modello dinamico di un elettrolizzatore.
Nella prima parte del lavoro, un modello dinamico esistente di un elettrolizzatore PEM, realizzato in Simulink®, è migliorato, completato e validato. Durante questo processo, vengono proposti suggerimenti per la modellazione di elettrolizzatori PEM. La validazione è effettuata utilizzando dati provenienti dal funzionamento di un elettrolizzatore PEM commerciale da 60 kW, testato presso l'Università della California Irvine.
La seconda parte riguarda l'ottimizzazione del funzionamento del sistema, con particolare attenzione al caso di accoppiamento con fonti di energia rinnovabile non programmabili. Il sistema segue adeguatamente i carichi dinamici ed ha transitori di avviamento veloci. L'ottimizzazione dell'avviamento ha rivelato un potenziale aumento di efficienza fino al 13% in caso di uso intermittente. L'efficienza netta del sistema è pari al 57% a carico nominale, ma scende significativamente a carico parziale, con un'efficienza del 27% al 20% del carico, principalmente a causa delle perdite di idrogeno nel sistema di purificazione dell'idrogeno. L'ottimizzazione dell'uso di tale sistema ha portato ad un incremento di efficienza a carico parziale fino a 23%$_{pt.}$, mentre l'ottimizzazione dell'uso degli ausiliari fino a 12%$_{pt.}$.
Il funzionamento del sistema ad alte pressioni risulta essere più conveniente tanto più alto è il carico. Conoscere il crossover di idrogeno e la sua dipendenza dalla pressione è fondamentale nella valutazione delle performance ad alta pressione, richiedendo maggiore ricerca nella modellizzazione di tale fenomeno.

PAROLE CHIAVE: elettrolisi; PEM; simulazione; ottimizzazione; idrogeno; energia rinnovabile

EXTENDED ABSTRACT

Introduction

In a scenario where falling costs of renewable energy systems and more effective policies on GHG emissions are driving impressive growth in the renewable capacity installed [1], energy storage could play a pivotal role in balancing inflexible or intermittent generation typical of these non-dispatchable systems [2], such as wind and solar power plants. Among power-to-gas applications, water electrolysis is gaining popularity, as hydrogen has been identified as an highly versatile energy carrier [3]. Different technologies of electrolyzers are commercialized, distinguished by the type of electrolyte, electrochemical reactions and operating conditions. This work focuses on PEM (Polymer Electrolyte Membrane) technology, identified as the most suitable for coupling with renewable sources and for grid balancing services, thanks to its high efficiency, flexibility, fast transients, and high load rangeability [4].

Thesis objectives

This work consists of two main parts. In the first part, an existing dynamic model of a PEM electrolyzer, realized in Simulink®, is completed, improved and validated using data from an experimental campaign carried out at the University of California Irvine [5]. In the second part of the work, the major sources of system inefficiency are identified, and the validated model is used to simulate the electrolysis system dynamic operation. The goal is to find and evaluate the benefits of different strategies for optimizing its operation in a context of coupling with RES or use for grid balancing services, characterized by intermittent and frequent partial load operation.

Electrolysis system layout

The system analyzed in this work is based on a 60 kW PEM electrolyzer commercial unit, following the layout shown in Figure 1.

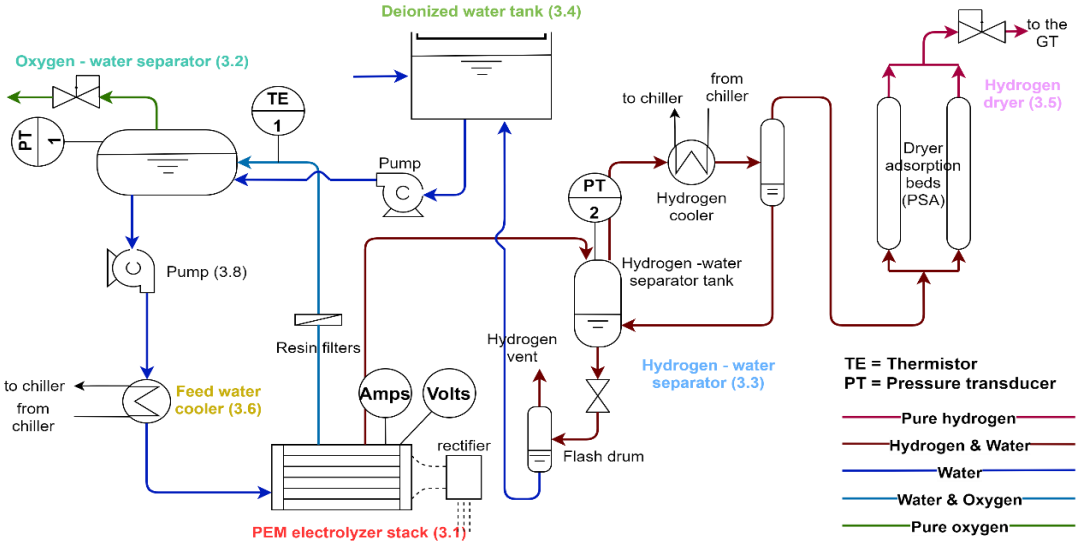

Figure 1 – Simplified scheme of the electrolysis system layout

The electrolyzer stack is composed by 65 electrochemical cells, fluid dynamically connected in parallel and electrically connected in series. Liquid water is supplied to the stack on the anode side, by means of a circulation pump. A heat exchanger allows to control the stack temperature following a PID controller approach, by removing heat from the water before it enters the stack. The water exits the stack enriched with oxygen, passes through resin filters which have the function of keeping the water conductivity below 1 µS/cm, and enters the oxygen–water phase separator, which collects the water in order to re-send it to the stack, realizing a loop. The oxygen-water separator pressure is kept slightly above atmospheric pressure (around 1.5 bar_g) by a backpressure valve regulating the oxygen flow exiting the tank and vented outside the system. The oxygen flow exiting the system is wet, thus the amount of water inside the oxygen–water separator is controlled by a pump, refilling it intermittently with deionized water from the deionized water tank. On the cathode side of the stack, a flow of water-saturated hydrogen gas is generated. This gas enters the hydrogen–water phase separator where it encounters a first drying process, by means of heat removal and gravimetric separation. The level of the liquid water collected on the bottom of the hydrogen–water phase separator is controlled by an intermittent purge of water, which is purified from the dissolved hydrogen in a flash drum and sent back to the deionized water tank. The partly-dried hydrogen reaches out a further drying process in a PSA (Pressure Swing Adsorption) system. The pressure in the PSA system and upstream units is maintained at 30 bar_g by a backpressure valve. The electrolysis system is supplied with 3-phase alternated current. Part of this current is sent to the auxiliaries of the system, as pumps and fans, working with AC current, while the rest is sent to the rectifier, which converts AC current into DC current to feed the stack.

Electrolysis System dynamic model

A dynamic model of the complete electrolysis system, including BoP components, realized with the software MATLAB Simulink®, is completed and improved. Gas properties are calculated with the hypothesis of ideal gas and ideal gas mixture, while liquid properties with the hypothesis of ideal liquid. PI-type and on-off controllers are implemented in order to simulate the control of the system operation.

PEM electrolyzer stack model

The PEM electrolyzer stack is modelled with a lumped-volume approach. The fluids entering the stack are assumed to reach immediate thermal equilibrium with it and the temperature dynamic is taken into account by the stack thermal capacity. The model receives as input the electrical current, the flow rate, temperature, pressure and composition of the inlet water, and the anodic and cathodic backpressures. Mass and energy balances are solved in order to determine the stack temperature and the flow rate, composition and temperature of the flows leaving the stack. The electrochemical behavior of the single cells is modelled through semi-empirical polarization curves, allowing to compute the cell voltage, reflecting voltage dependence on temperature, pressure and current density:

$$V_{cell}(T,p,i) = \frac{\Delta G_{rev}(T,p_{ref})}{nF} + \frac{RT}{nF}\ln\left(\frac{a_{H_2}\cdot a_{O_2}^{0.5}}{a_{H_2O}}\right) + \Delta V_{act} + R_{MEA}\cdot i\cdot A_{cell} + \frac{RT}{\alpha_{anode}nF} ln\left(\frac{i_L}{i_L - i}\right)$$

where the first two terms represent the open circuit voltage, the third term the activation overpotential, the fourth the ohmic overpotential and the fifth the concentration overpotential. Once the cell voltage is computed, considering the modularity of the stack, the overall stack voltage is computed. Improvements to the electrochemical model involved the evaluation of the activation overpotential, which is no more evaluated by means of the Tafel equation, demonstrated to be valid only for high current densities [6], but with an expression derived from the Butler-Volmer equation, assuming symmetry in the processes of electronic transfer and equally distributed charge [6], expressed as:

$$\Delta V_{act,X} = \frac{R \cdot T}{F} \cdot \sinh^{-1}\left(\frac{i_X}{2 \cdot i_{0,X}}\right)$$

where X is either the cathode or the anode, $i_{0,X}$ [A/cm^2] is the exchange current density of the half-reaction occurring at electrode X [7], and the implementation of an expression describing the dependence of the exchange current density from the temperature [39, 40]:

$$i_{0,X} = i_X^{ref} \cdot exp\left(-\frac{E_{act,X}}{R \cdot T}\right)$$

where i_X^{ref} is the pre-exponential factor and $E_{act,X}$ is the activation energy for anode and cathode, respectively. Semi-empirical correlations for natural convection are added to the original model in order to compute the heat losses towards the external environment, as well as a simplified correlation for the evaluation of the hydrogen crossover throughout the membrane, modelled through the calculation of the Faradaic efficiency as a function of the current density [9]:

$$\eta_F = 1 - \left(\frac{a}{i}\right)$$

where the a [A/cm^2] coefficient is proportional to the hydrogen crossover and estimated on the basis of the available data on the hydrogen net production.

Oxygen–water and hydrogen–water separators

In the separators, the liquid water is separated from the gas by gravimetric separation. In both the thanks liquid–vapor equilibrium is assumed, thus the gases are assumed to be saturated with water vapor. The gases are taken from the top of the tanks while the liquid is taken from the bottom. Relays control the intermittent flow rates of liquid water refill and liquid water purge to the oxygen–water separator and from the hydrogen–water separator tanks, respectively, while PI-type controllers regulate the gas flows in order to keep the tank pressures at the setpoint values, simulating the backpressure valves. The water condensing in the heat exchanger downstream of the hydrogen–water separator is computed assuming both the inlet and outlet gas flows to be saturated with water vapor. The models receive as input the inlet flows pressure, temperature, flow rates and composition and solve dynamic mass and energy balances in order to compute the compositions and the amount of liquid and gas in the tanks, their temperature, and the pressure, temperature and compositions of the outlet flows. Semi-empirical correlations for the computation of the convective heat losses towards the environment are added.

Hydrogen dryer (PSA)

A simplified model of the PSA drying system, which was not present in the original model, is introduced in this work. Being the hydrogen purity at the PSA outlet

>99.9998%, the outlet flow is assumed to be pure hydrogen, allowing to compute the amount of water entrained in the vessel. The hydrogen slipstream used to purge the regenerating bed, which is orifice driven, is computed by means of the "ASME" equation for an orifice [10], properly calibrated on the basis of the experimental data, as:

$$\dot{m}_{orifice} = (KY)A_0\sqrt{2g\rho_1\Delta p}$$

where KY [$m^{1/2}/s$] is the discharge coefficient, A_0 [m] is the orifice area, g [m/s^2] is the gravity acceleration, ρ_1 [kg/m^3] is the density of hydrogen upstream the valve and Δp [Pa] is the pressure difference across the orifice. The mass flow rate exiting the PSA is computed as the sum of the hydrogen purge mass flow rate and the mass flow rate of hydrogen passing through the backpressure valve, which allows to control the pressure. The hydrogen loss when the active vessel is sent into regeneration mode, due to depressurization, is computed as the difference between the hydrogen contained in the vessel at rated pressure and the hydrogen contained in the vessel at atmospheric pressure. The assumption of isothermal system is made since the latent heat of the condensing water is extremely low compared to the inertia of the system, as only traces of water are condensed. The dynamic of the PSA system, related to the gas accumulation in the active adsorption bed, is modelled by including in the hydrogen-water separator model the volume of the PSA bed itself.

Deionized water tank

The deionized water tank is modelled by solving dynamic energy and mass balances, assuming an uniform temperature inside the tank. Also in this case convective heat losses are introduced.

Feed water cooler

The cooler is modelled as a counter-current plate-type heat exchanger working with liquid streams on both the water (hot) and refrigerant (cold) sides. It is composed of parallel plates forming a modular structure, therefore, it is modelled as a sequence of identical sub-units composed by a single plate and half of the adjacent hot and cold channels. The heat transferred, the temperature of the plate and of the outlet streams are computed, discretizing the unit along the direction of the channels (1D-model). For each control volume, mass and energy balances are solved assuming a uniform temperature for the plate, neglecting heat transfer by conduction along the flow direction, fluid mass accumulation in the channels and heat losses to the environment. Temperature dynamic is related to the thermal capacity of the heat exchanger materials. Pressure losses are computed assuming laminar flow.

Pipes

The Simulink model computes the distributed pressure drops in the pipes as function of the volumetric flow rate and the concentrated pressure drops by means of corrective coefficients on the distributed pressure drops. Transport delays are also modelled by considering the volumetric flow rates and the cross sectional area of the pipes.

Pumps

A steady state model of the pumps is implemented. Their electrical consumption is computed by considering the head that they have to provide, the mass flow rate and

assuming constant isentropic, mechanical and electrical efficiencies, as well as the temperature and pressure of the outlet fluid.

Rectifier

The rectifier model block receives as input the electrical power (AC) supplied to the electrolyzer system and the stack voltage computed by the stack model block. After subtracting the auxiliaries consumption, it computes the electrical losses for conversion from AC to DC current and outputs the electrical current supplied to the stack.

Experimental campaign

For model validation, datasets from the running of the electrolyzer system during the University of California Irvine (UCI) power-to-gas demonstration project [11] have been used. During the experimental campaign the electrolyzer was operated in two different ways: imposing a variable in time hydrogen output while executing cold startups (first dataset, Figure 2) and reproducing the power input profile from solar PV (second dataset, Figure 3 left) and wind power (third dataset, Figure 3 right), in order to evaluate the system performances and dynamic dispatch capabilities.

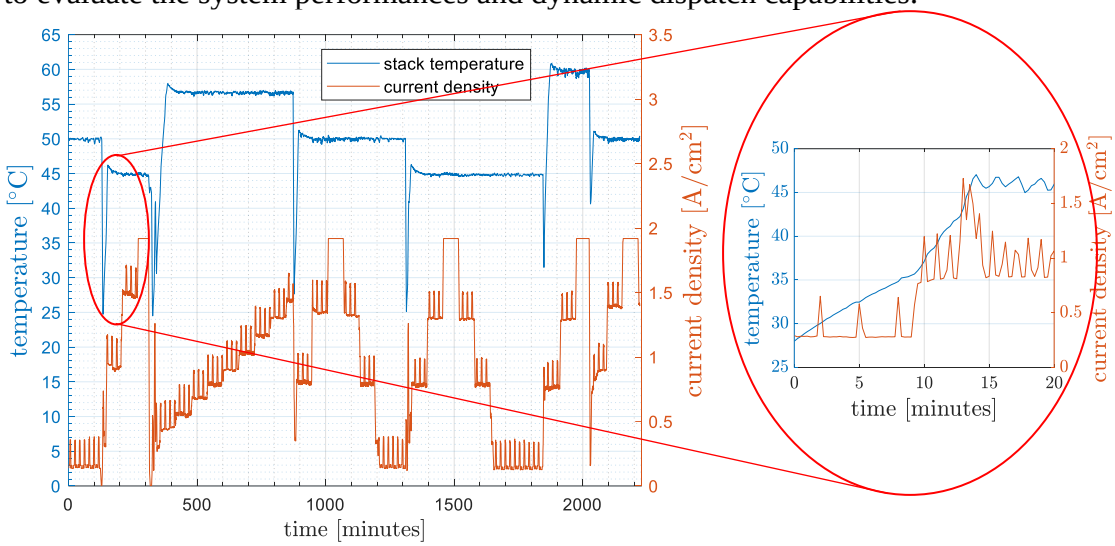

Figure 2 – General view of temperature and current density profiles from the first dataset and particular showing one of the six warmups

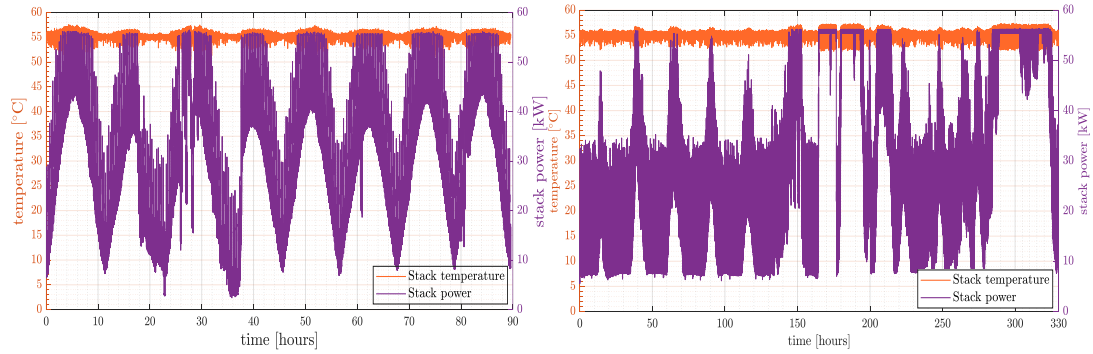

Figure 3 - Stack power and temperature over time in PV-coupling (left) and wind-coupling (right)

The data available for this work are the hydrogen pressure in the hydrogen–water separator, oxygen pressure in the oxygen–water phase separator, stack current, stack voltage and water temperature at the anode outlet, which are collected at 1 s intervals and averaged down to 15 seconds intervals.

Model validation

The first dataset is used for the validation of the electrochemical behavior of the stack (polarization curves) as it is the one with the widest range of temperatures and pressures. The i-V couples are clustered in 7 temperature intervals ranging from 23.5 °C to 62 °C and for each cluster the stack operation is simulated, changing the current from 0 to 2 A/cm^2 and setting the values of pressures and temperature to the average ones of each cluster, in order to reduce the error due to the dependence of the polarization curves from the other parameters (Figure 4). The results show a maximum error on the voltage of 3.9 %, verified in the temperature range of 37.2 ± 2.7 °C. In general the absolute error is higher at higher currents, and voltage results to be slightly overestimated at high operating temperatures and slightly underestimated at low temperatures, showing that there is still room for improvements in the polarization curves model. The cluster characterized by the minimum error is the one in the temperature range of 53.8 ± 2.7 °C, with a maximum error on all the currents range of the 1.37% and an average error of 0.2%.

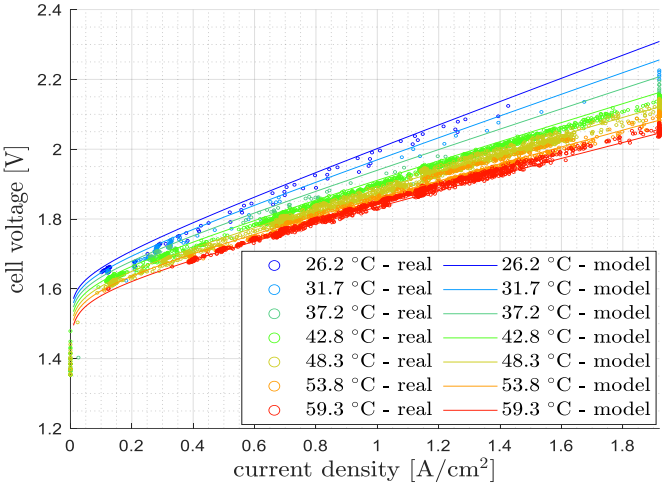

Figure 4 - Cell voltage vs. current density from model operation (continuous lines) and from the first dataset

It is not possible to execute the same procedure to validate the voltage dependence on pressure, as the available data were not taken at a sufficiently wide range of pressures, but from a comparison with experimental results available in the literature [12] it is possible to see a similar behavior in the curves predicted by the model at different pressures with respect to the experimental data, showing that the OCV is the main parameter determining the overall voltage increase with the pressure.

The second dataset is used to validate the capability of the model to follow dynamic loads, keeping low errors on the voltage. The first dataset is used also for the validation of the system thermal behavior, by fitting the stack thermal capacity with the thermal transients of the stack (Figure 5).

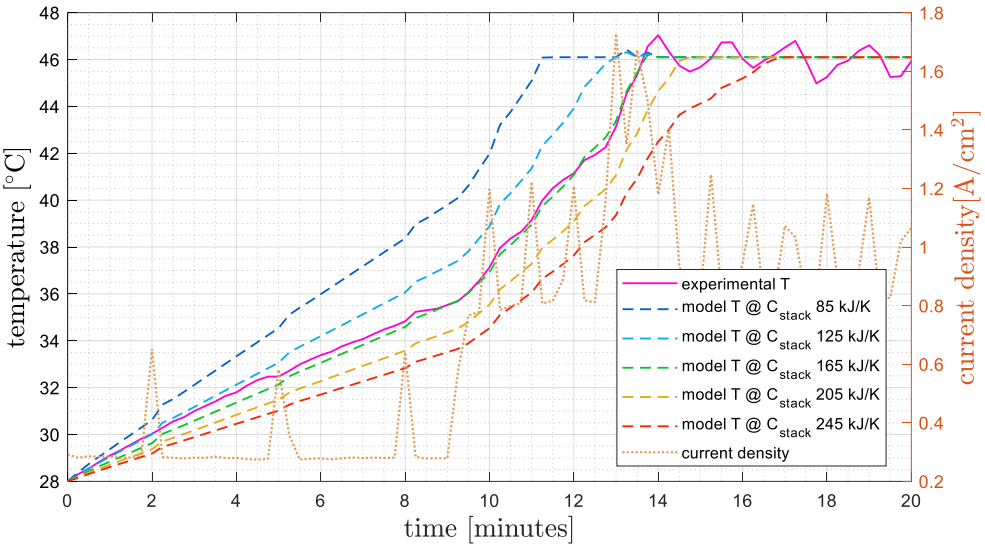

Figure 5 - Experimental current density and stack temperature over time and temperature profiles (dashed lines) resulting from simulations at different stack thermal capacities

Among the 6 transients available, 3 of them have a fitting stack thermal capacity close to 165 kJ/K, while the other 3 around 215 kJ/K. Some irregularities in temperature trend of the last three transients show that some external event, influencing the stack energy balances, occurred (such as a premature start of the cooler), leading to an overestimation of the thermal capacity. Hence, the stack thermal capacity is set to 165 kJ/K, value that allows to have a maximum error on the temperature of 6.4% in all the available transients.
The validation of the model capability to follow dynamic loads keeping low errors on the temperature is executed by simulating the third dataset. Finally, the first dataset is used for the validation of the cathode pressure evolution. The maximum error for the pressure transients time results to be equal to 15 s.

Being no data about hydrogen production and system performances available, the model performances are validated through the data available from [5], where the same system object of the analysis was studied. The comparison between the experimental results and the ones resulting from simulations is shown in figure 6:

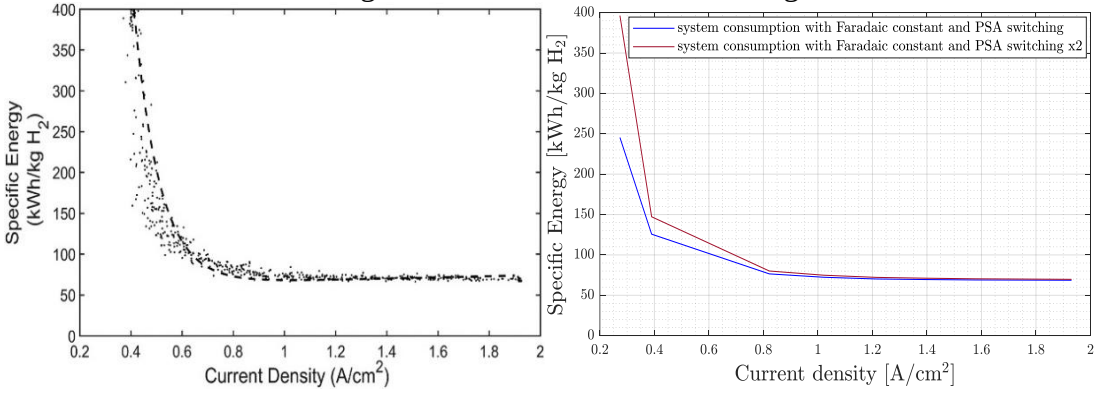

Figure 6 – System net consumption vs. current density experimentally measured (left chart) and resulting from model running

Finally, the different contributions of the consumption for producing a unit mass of hydrogen are evaluated from the model and compared to experimental calculations. Results from the simulations show a fixed 7% consumption for AC/DC conversion, ancillary power consumption ranging from 4% at nominal power to 18% at 15% of the nominal power, hydrogen losses from 7% to 32% and stack from 82% to 44%. Hydrogen loss contribution is slightly underestimated with respect to experimental results, but it's anyway the main loss when the system is operated at low load.

System optimization

Start-up optimization

System startup optimization is performed by simulating the system operation setting different constant power inputs. Base case analysis shows a startup time ranging from 7' at full load to 45' at 20% load. Different solutions are studied to decrease the warm-up time and improve the system efficiency. Delaying the oxygen–water separator refill allows to reduce the warm-up time, but no significant improvements in the average efficiency are reached. The implementation of hot standby results in an increase in the average efficiency at the end of the startup time around 2%$_{pt.}$ (Figure 7), resulting to be convenient only if the oxygen–water separator tank is thermally insulated. Finally, by using 'free' electricity sources (such as when the power supply is not sufficient to run the system) it is possible to pre-heat the system, allowing to reach an increase in hydrogen production up to 13% at the end of the warmup time.

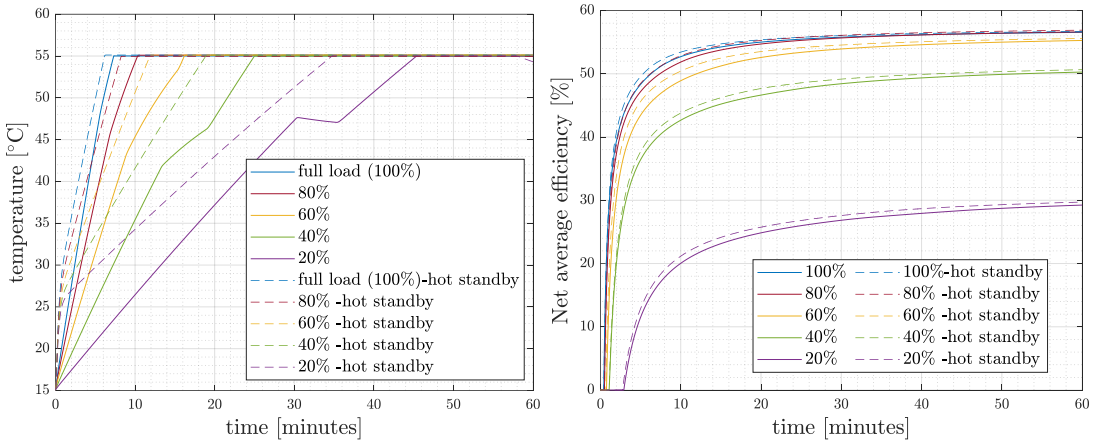

Figure 7 – Temperature evolution over time (left figure) and average efficiency over time (right figure) when implementing hot standby on the oxygen-water separator

Part-load operation optimization

As the main source of efficiency loss in partial load operation is the hydrogen lost in the drying system, different strategies for its reduction are analyzed (Figure 8 left). As the hydrogen purge flow sent from the active bed of the PSA system to the regenerating bed is independent from the amount of water entrained in the bed, a solution based on the installation of a control valve upstream the orifice is proposed, in order to stop the hydrogen purge flow when it's no more necessary. System consumption at part load shows a reduction up to 38%. A second solution focuses on the reduction in the hydrogen lost during the depressurization of the PSA beds, by increasing the time between two regenerations (which is fixed in the actual system) on the basis of the

estimation of the amount of moisture entrained in the bed. The system consumption decrease is estimated around 10%, while the contemporaneous implementation of both strategies leads to a net consumption reduction up to 42%.
Part-load operation optimization based on the implementation of a variable speed pump leads to a system consumption decrease up to 28% (Figure 8 right) and is proven to be feasible in terms of water utilization level at the anode.

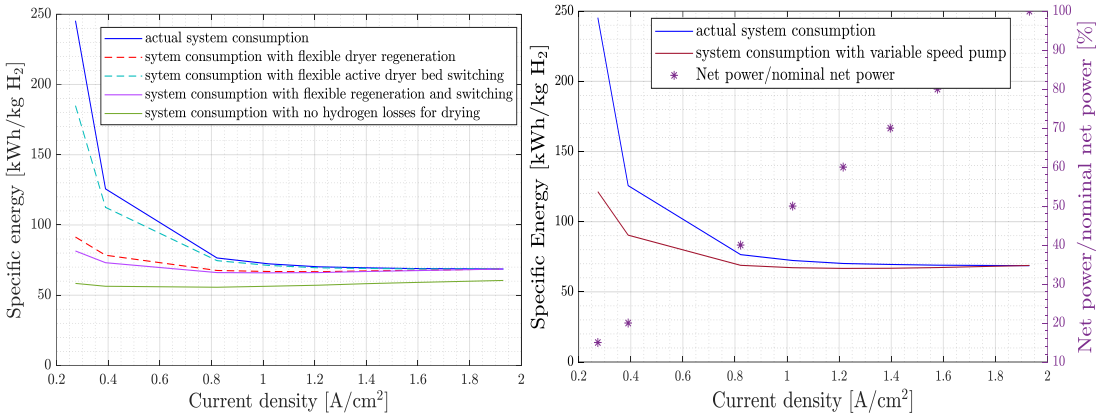

Figure 8 – System net consumption in the actual case and with different optimization strategies for the PSA operation (left) and with the use of a variable speed pump (right)

High pressure operation
The system operation at high pressure and the standard operation at 30 bar_g with subsequent compression in order to obtain in both cases 70, 140 and 210 bar_g of hydrogen delivery pressure are compared on an energy consumption point of view (Figure 9). High pressure operation results to be more convenient at higher loads with respect to the use of post-compression. In general, the reduction of the Faradaic efficiency with pressure results to be the main discriminant in the choice of one or the other type of compression. Only systems which are able to operate at high pressure maintaining very limited the hydrogen crossover across the membrane have the potentiality to compete with the classical compression systems by means of displacement inter-refrigerated compressors.

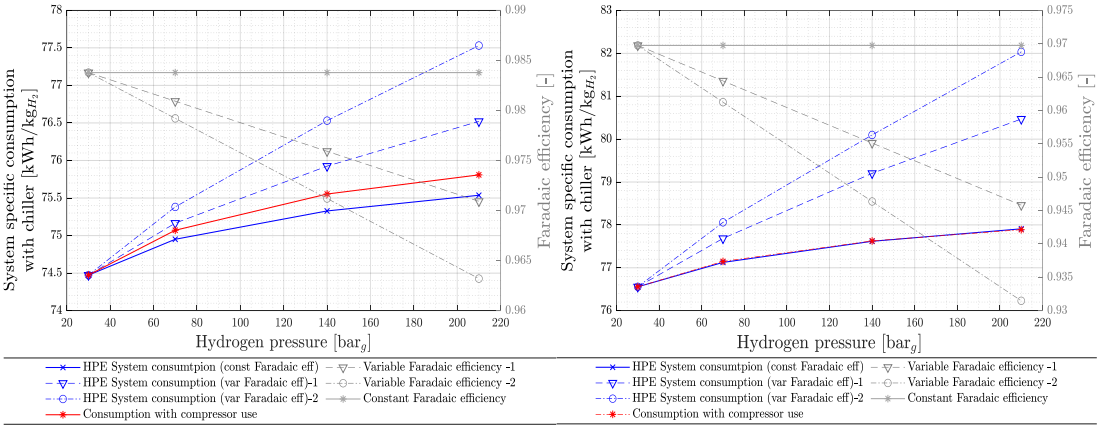

Figure 9 – System consumption for delivering hydrogen at different pressures with compressor use (red line) and high pressure electrolysis (blue lines) assuming different scenarios for Faradaic efficiency decay with pressure at full load (left) and 50% of the full load (right)

Conclusions

The modelling of the system has led to the development of a tool able to simulate the electrolyzer dynamic operation, maintaining limited errors on all the main operating parameters. The hydrogen losses in the drying system result to be slightly underestimated, but not sufficient information are provided to understand the reason of such high losses. In any case this deviation from the real case is not considered to be able to significantly affect the quality of the results and their meaning. On the contrary, who's writing believes that this error could lead the analysis into a conservative position, with real increases in system efficiency through the proposed improved operation strategies higher than estimated by the present analysis. Being not possible to validate the system operation at different pressures, because of the lack of data, a qualitative comparison with experimental data is performed, allowing to deduce that the model approximates in a realistic way the behavior at different pressures, but further experimental campaigns involving experiments at different pressures are necessary. Finally, the modelling of the hydrogen crossover by means of the Faradaic efficiency seems to match the results from the literature, but also in this case more accurate models that allow to predict its variation with pressure should be developed.

Among the analyzed operation strategies, hot startup implementation has the ability to improve the efficiency of about $2\%_{pt.}$ with respect to the cold startup when it involves only the oxygen-water separator tank, being convenient only for well thermally insulated tanks, but if the hot startup also involves the stack and is performed by using waste/unusable power (such as early morning solar PV power), it can lead to efficiency increases ranging from 9% to 13%.

Improved management of the drying system has proven to be able to reduce by 76% the losses of hydrogen associated with this system, without the need to replace the two-bed PSA, with a more performing 4-bed or more PSA system, which would certainly lead to a significant reduction in hydrogen losses, but also to higher investment costs.

The BoP components optimizations, regarding the centrifugal pump feeding the stack, allows to reduce system consumption at low load up to 28%, but may not be convenient if the system is operated mainly between 50% and 100% of the nominal power, as its benefit is low in this range of loads. Thus, the replacement of the fixed speed pump with a variable speed pump must be the result of a tradeoff taking into account the cost of the variable speed pump and the typical load at which the system will be operated.

The typical load at which the system is operated must also be taken into account when considering high pressure operation, which is more convenient with respect to compressor use for higher loads, as the cell efficiency is less affected by high pressure operation when operating at high current densities. The breakeven point, below which high pressure operation is no more convenient on an energy point of view depends on the characteristics of the compressor and on the efficiency decay due to hydrogen crossover increase, and results to be equal to 50% of the rated power for any delivery pressure considered when neglecting the Faradaic efficiency dependence on the pressure and assuming a constant polytropic efficiency of 75% for the compressor.

Possible future developments of this work could be the modelling of the behavior of the polarization curves at different pressures and the modelling and validation of the faradaic efficiency dependence on the pressure.

CONTENTS

LIST OF FIGURES

SYMBOLS AND ACRONYMS

Symbols

V	*V*	Voltage
ΔV	*V*	Overpotential
I	*A*	Current
i	A/cm^2	Current density
G	*J/mol*	Molar Gibbs free energy
H	*J/mol*	Molar enthalpy
S	*J/mol/K*	Molar entropy
T	*K*	Temperature
n	-	Number of electrons participating to the reaction
F	*C/mol*	Faraday's constant (*96485.33 C/mol*)
R	*J/mol/K*	Universal gas constant (*8314 J/mol/K*)
$\dot{m}_i$	*kg/s*	Mass flow rate of the species *i*
x_i	-	Molar fraction of the species *i*
y_i	-	Mass fraction of the species *i*
$\dot{V}$	m^3/s	Volumetric flow rate
p	*bar*	Pressure
Δp	*Bar*	Pressure drop
P	*W*	Power
Q	*J*	Heat
$\dot{Q}$	*W*	Heat flux
t	*s*	Time
D_i	cm^2/s	Diffusion coefficient of the species *i*
M	*kg*	Mass
V	m^3	Volume
A	m^2	Cross sectional area
η	-	Efficiency
η_F	-	Faradaic efficiency
ρ	kg/m^3	Density
a_i	-	Activity of species *i*
p_i	-	Partial pressure of the species *i*
σ	*S/cm*	Conductivity
MM_i	*g/mol*	Molar mass of the species *i*
C	*J/K*	Thermal capacity

Acronyms

AC	Alternating Current
BoP	Balance of Plant
CAPEX	CApital EXPenditure
DC	Direct Current
EC	Electrolysis Cell
ESS	Energy Storage System
EU	European Union
FC	Fuel Cell
GHG	GreenHouse Gases
HHV	Higher Heating Value
HPE	High Pressure Electrolysis
IEA	International Energy Agency
LHV	Lower Heating Value
MEA	Membrane Electrode Assembly
OCV	Open Circuit Voltage
OPEX	OPerating EXpense
P2G	Power-to-Gas
P2H	Power-to-Hydrogen
PEM	Polymer Electrolyte Membrane
PID	Proportional-Integral-Derivative control
PSA	Pressure Swing Adsorption
RES	Renewable Energy Sources
SoA	State of the Art
UCI	University of California Irvine
vRES	variable Renewable Energy Sources
WACC	Weighted Average Cost of Capital

1

CHAPTER 1 – INTRODUCTION

Facing climate change is one of the key challenges of our century. Human emissions of carbon dioxide and other greenhouse gases are reported to be a primary driver of climate change [13] and, as the global energy-related carbon dioxide emissions passed 33 billion tons in 2019 and are rebounding and growing in 2021 after the 2020 momentaneous decrease due to the Covid-19 pandemic [14], the international community is trying to limit the temperature anomaly "well below 2 °C", as laid out in the Paris Agreement.

The two main paths identified to reduce GHG energy-related emissions are the increase in the efficiency with which energy is used and/or produced and the exploitation of renewable sources, such as solar energy and wind energy, which are intermittent and unpredictable by nature ([15], Figure 1.1).

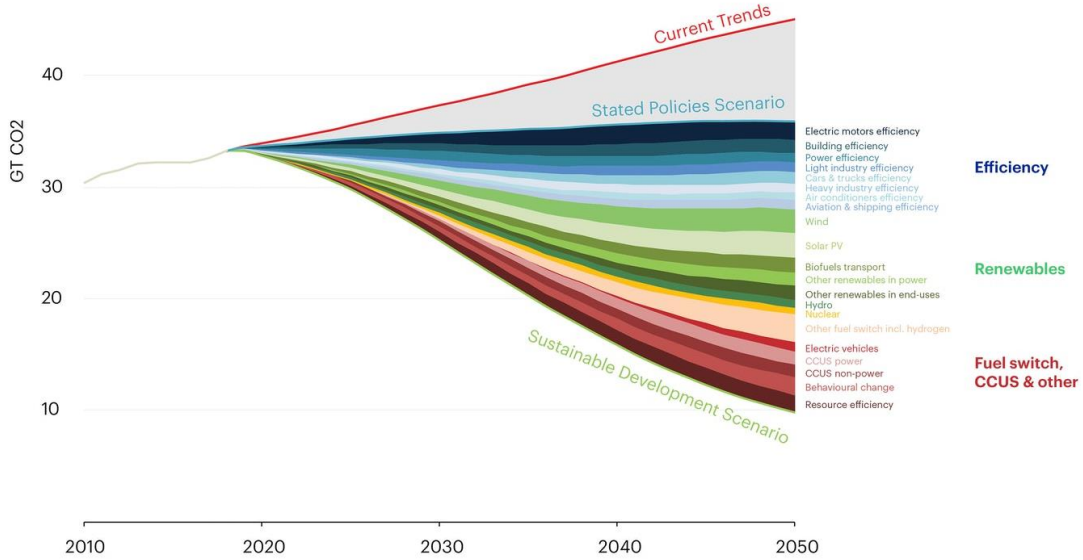

Figure 1.1 – 'Wedges' model showing yearly energy–related CO_2 emission following a business as usual scenario (red line), stated policies scenario (blue line) and a sustainable development scenario (green line) [15]

Falling costs and more effective policies are driving impressive growth rates in the new renewable capacity installed all over the world, greater than any other energy source [1]. Therefore, new critical issue that is arising from this continuous growth of the variable renewable energy sources (vRES) in the energy mix is how the electrical

grid can handle higher shares of non-dispatchable power, since security of electricity supply cannot be undermined [1]. This issue is seriously limiting the exploitation potential of renewables, whose installation requires to increase the grid flexibility to contrast the decrease in power dispatchability.

International Energy Association defines a power system flexibility as "The ability of a power system to reliably and cost-effectively manage the variability and uncertainty of demand and supply across all relevant timescales" [16]. Flexibility can be achieved using dispatchable power plants, such as gas turbines or hydro power, flexible demand (demand side management – DSM and demand response – DR practices), generator output curtailment and energy storage systems [2].

Energy storage has therefore been identified as one possible way for unlocking the potential of renewable sources, allowing a better integration of vRES by increasing their dispatchability and power system flexibility.

1.1 Energy storage systems

Energy storage systems (ESS) are used to convert the energy generated during periods of electricity surplus from vRES into a storable form of energy (e.g. chemical, thermal, kinetic, gravitational etc.) in order to reconvert it in electricity when needed, or more convenient. The ESS classification is usually based on the energy conversion mode:

- Electric systems: supercapacitors, superconducting magnetic energy storage;
- Mechanical systems: pumped hydroelectric storage (PHS), compressed air energy storage (CAES), flywheel energy storage (FES);
- Electrochemical Systems: batteries (mainly Li-ion batteries and flow batteries);
- Chemical systems: based on the conversion of electricity into chemical energy (Power-to-X, P2X), among which hydrogen based systems are located (P2H).

A comparison of the main ESS is illustrated in Figure 1.2.

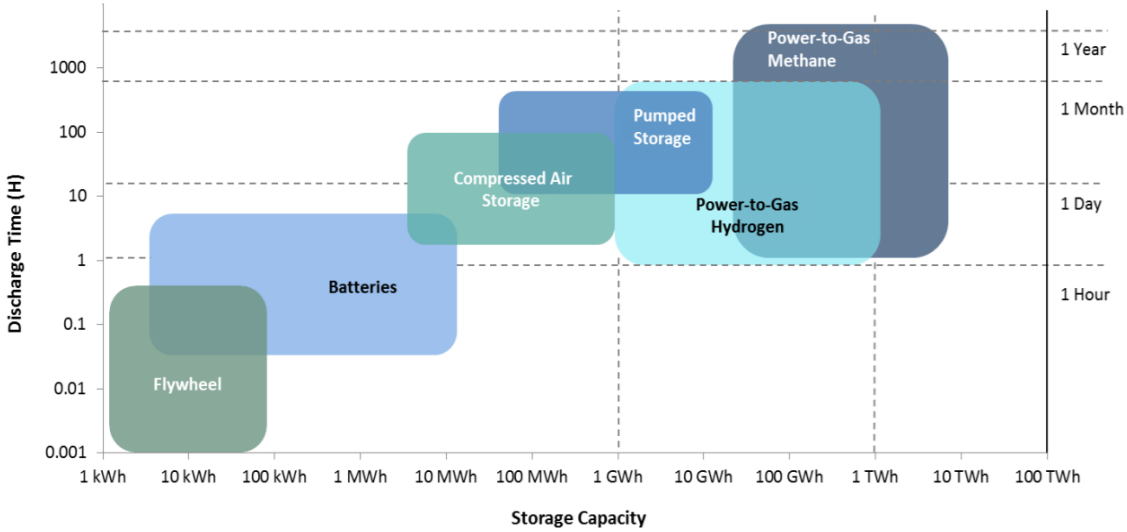

Figure 1.2 – Comparison of the different ESS in the discharge time vs. capacity plot [17]

1.2 The role of hydrogen

Hydrogen is gaining popularity as energy carrier all over the world and in particular in Europe, where it's been identified as an important player in the energy transition, supporting EU's commitment to reach carbon neutrality by 2050 [3]. Efforts are being done to encourage the development of the entire value chain of hydrogen (Figure 1.3) aiming at absorbing the electricity surplus from vRES, including the constitution of the "European Clean Hydrogen Alliance" [18], and the definition of a strategic roadmap for hydrogen and economic policies, such as investments and incentives. Excluding from this discussion the reasons of a strategic nature, such as the achievement of energy independence and the opportunity of developing valuable and exportable technologies, which are clearly present, hydrogen value chain certainly holds many advantages:

1. Power-to-gas (P2G) applications can, as it's possible to see in Figure 1.2, store huge amount of energy for long time periods, and therefore absorb the fluctuations of vRES not only on an hourly or daily basis, but also on seasonal basis;
2. Hydrogen can be used as energy carrier, by reconverting it in electricity by means of Fuel Cells or using it as clean fuel, but also as feedstock in many fields, from chemical, to oil & gas, to food industry and it holds a huge potential for the decarbonization of some industrial processes, e.g. the metallurgical sector;
3. The electricity conversion into hydrogen only requires pure water (water electrolysis) and with modern technologies it can be performed with high flexibility of operation and efficiencies;
4. Hydrogen is the chemical compound with the highest energy density (LHV = 120 MJ/kg) on a mass basis (but given its low density at ambient conditions the density on a volume basis is low and compression or liquefaction are required for storage).

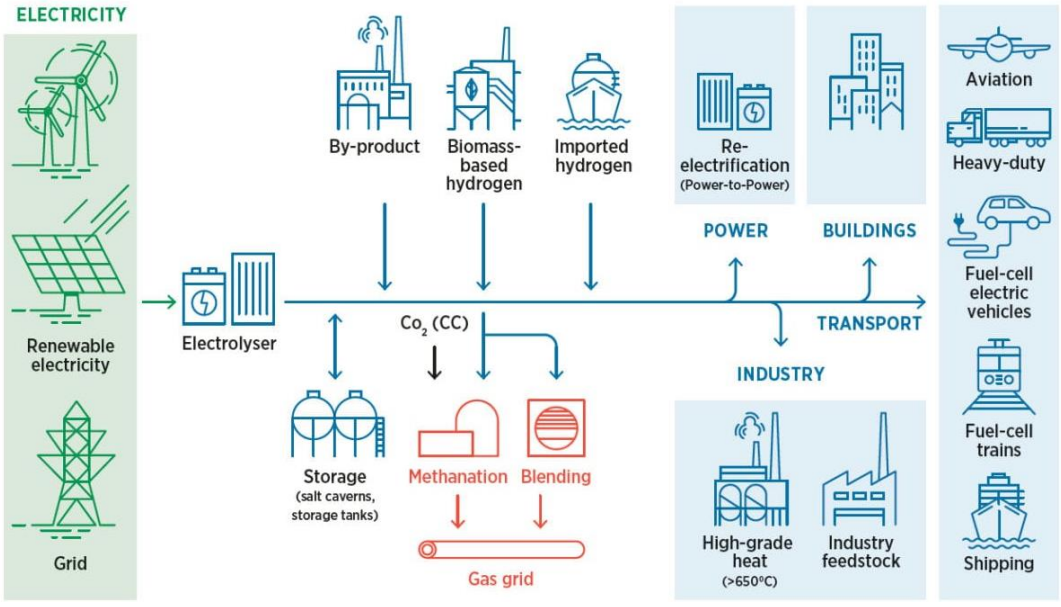

Figure 1.3 – Schematic of hydrogen value chain from integration with vRES to end use [19]

1.3 Green hydrogen technologies

Green hydrogen (hydrogen produced from renewable electricity) is produced by means of electrochemical devices, Electrolysis Cells (EC), and can be reconverted in electricity in different ways, among which electrochemical devices (Fuel Cells – FC) and gas turbines. In the EC, water electrolysis is carried on, so electricity (and heat) is used to provide the energy to split up the water molecules in hydrogen (H_2) and oxygen (O_2). In order to enable such electrochemical reactions to take place, electrolysis cells are provided with two electrodes, where the electrochemical reactions take place and electrons are free to flow, between which it is interposed an electrolyte, impermeable to electrons but permeable to ions. To enable the cells to correctly function, they are equipped with Balance of Plant components. In this work the assembly of the cell and all the BoP components will be referred to as 'System'.

The different electrolysis cell technologies are classified according to the nature of the electrolyte used, among which the three dominant technologies today are alkaline EC (AEC), Proton Exchange Membrane EC (PEMEC) cells and Solid Oxide EC (SOEC).

1.3.1 Alkaline electrolysis cells (AEC) technology

In alkaline cells the electrolyte is composed by a porous matrix saturated with an aqueous solution of potassium hydroxide (KOH), which is able to transport OH^- ions. AEC is a consolidated technology with long lifetime, cell efficiency up to 80% and system efficiency up to 67%. They operate at a temperature up to 80 – 100 °C and their main limitations are connected to the corrosive electrolyte, the startup time, which is longer than PEM ECs, and lower flexibility (min. load 20 – 40%) [13, 14], characteristics which make them less suitable for direct coupling with vRES.

1.3.2 Solid Oxide Electrolysis Cells (SOEC) technology

This electrochemical cells use solid oxides as electrolyte (generally Yttria-stabilized Zirconia) that allow the passage of $O^=$ ions. They are high temperature electrochemical cells, characterized by operating temperatures of 600 – 1000 °C. They are reversible, meaning that the same system can be used alternatively in FC or EC mode and, thanks to the high temperature they are suitable for cogeneration in FC mode and can use waste heat to increase the electrolysis efficiency in EC mode, reaching system efficiencies up to 90%. The system efficiency is reported to be around 80% at maximum [4]. On the other hand, the high operating temperature leads to long startup times (hours, from cold) and issues in temperature control in case of rapid load changes. Furthermore, this technology is immature, hence degradation issues which still need to be solved lead to short lifetime.

1.3.3 Proton Exchange Membrane (PEM) cells

Proton Exchange Membrane (or Polymer Electrolyte Membrane) cells use a solid polymer as electrolyte, generally Nafion®, which transports H^+ ions. These cells

feature high modularity and compactness thanks to the zero-gap architecture, made possible by the Membrane Electrode Assembly (MEA), namely the compact module that unites the two electrodes with the membrane [21]. PEM ECs have a system efficiency up to 70% and a cell efficiency of about 80% [22]. This kind of systems have an operating temperature around 60 – 80 °C [23]. They can work at very low partial loads (10%) and have a very fast startup time [4], which make them the most suitable technology for absorbing renewable electricity's peaks and in any case fast dynamics are involved. The main limitations of this technology are the low scalability and the high costs due to the membrane and the noble metals required on the electrodes as catalysts. Anyway, this technology is not as mature as alkaline cells and reduction in the production cost is forecasted.

1.4 PEM electrolysis technology

Among the various technologies to produce hydrogen from intermittent and fluctuating power sources as renewables, PEM Electrolysis (PEMEL) technology results to be the most suitable, thanks to its relatively high efficiency, flexibility, fast transients, the absence of environmental risks and the possibility to be operated at low partial loads (as discussed in section 1.3.3). Moreover, PEM electrolyzers present the possibility to be operated at high pressure, providing highly pressurized hydrogen without the need of a compressor (which also means lower acoustic pollution). Their main disadvantages are the high cost, due to the use of noble metal catalysts like iridium for anode and platinum for cathode, the cross permeation phenomena at high pressure and the fact that the hydrogen produced is water-saturated, requiring dehumidification [24]. Anyway, after drying the hydrogen has a very high purity, allowing direct injection in gas pipelines, gas turbines or fuel cells. While research in materials play an important role for making these devices cheaper, understanding their electrochemical and thermodynamic processes is fundamental to properly model and predict their behavior, in order to operate them in the most efficient way when coupled with variable electricity sources, which is finally the scope of this work.

1.4.1 Operating principle

The overall electrochemical nonspontaneous reaction of splitting water into hydrogen and oxygen, supplying energy (electrical and thermal), happening in a PEM electrolysis cell is given by:

$$H_2O_{(l)} \rightarrow H_{2(g)} + O_{2(g)} \tag{1.1}$$

which is divided into two semi-reactions happening at the electrodes, water oxidation at the anode **Errore. L'origine riferimento non è stata trovata.** and protons reduction at the cathode (1.3):

$$H_2O_{(l)} \rightarrow \frac{1}{2} O_{2(g)} + 2\, H^+_{(aq.)} + 2\, e^- \tag{1.2}$$

$$2\,H^{+}_{(aq.)} + 2\,e^{-} \rightarrow H_{2(g)} \tag{1.3}$$

A schematic of the working principle of a PEM electrolysis cell is shown in Figure 1.4. As oxygen is produced at the anode side, it leaves the cell, while protons flow through the proton-permeable membrane towards the anode. Direct current is supplied to the electrodes, and electrons flow through an external electrical circuit from the anode to the cathode, where they reduce the protons. The basic design of the cell consists in the MEA (Membrane Electrode Assembly), composed of a thin proton-exchange membrane with the two electrodes on each side. Each electrode is composed of an active layer (a porous catalyst layer where the reactions occur) and of a diffusion layer, which electrically connects the catalyst layer with the distribution plate (or bipolar plate). The bipolar plates have a structural role but also provide passage channels for products and reactants.

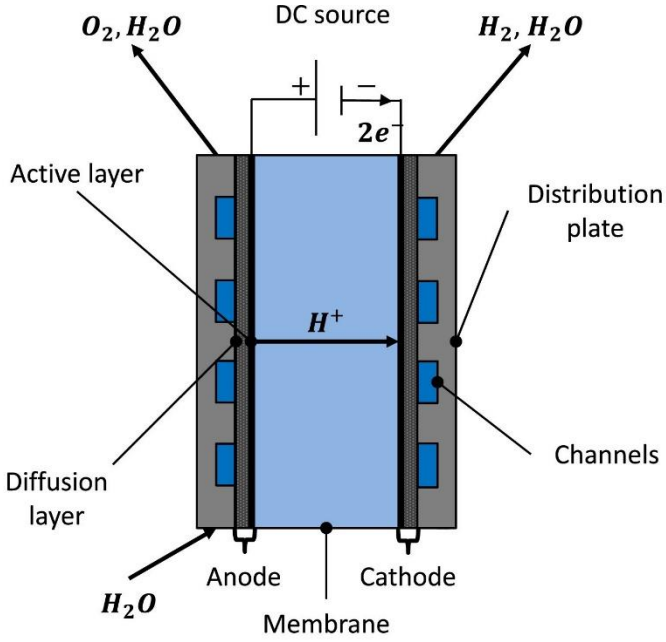

Figure 1.4 - Schematic of the operating principle of a PEM electrolysis cell [6]

The overall ideal energy that has to be supplied in order to make the reaction occur is equal to the heat of reaction (ΔH) of the (1.1), which can be split into two contributes, one that can be supplied by either heat or electricity (ΔQ) and one that has to be supplied by electricity (ΔG, the change in Gibbs free energy of the reaction).
The theoretical minimum voltage to be applied on the cell electrodes in order to make the reaction occur (thus, with the ΔQ contribute completely supplied as heat) and the ideal minimum cell voltage to be supplied without heat integration are called reversible cell voltage (V_{rev}) and thermoneutral voltage (V_{tn}), respectively, and are defined as:

$$V_{rev} = \frac{\Delta G}{zF} \tag{1.4}$$

$$V_{tn} = \frac{\Delta H}{zF} \tag{1.5}$$

where z is the number of electrons involved in the semi-reactions ($z = 2$) and F is the Faraday's constant (F = 96485 C/mol). Feeding liquid water below 100 °C to the cell (which is the case of PEMEL cells) the ΔH is in the range 284 – 286 kJ/kmol$_{H2}$, leading to a thermoneutral voltage of 1.47 – 1.48 V [25]. In particular, at standard conditions (p=1 atm, T=298.15 K) the change in the Gibbs free energy ΔG^0 is 236.483 kJ/kmol and the change in enthalpy under standard conditions ΔH^0 is 285.83 kJ/kmol, therefore, the reversible voltage at standard conditions to make the reaction occur is $V_{rev}^0 = 1.229\ V$ and the thermoneutral voltage at standard conditions is $V_{tn}^0 = 1.481\ V$ [26]. In reality, the cell voltage is always higher than the thermoneutral one, due to heat losses and thermodynamic irreversibilities, called overpotentials, which heat up the cell, making cooling required. These losses are divided into three types, activation, ohmic and concentration losses:

$$V = V_{rev} + V_{act} + V_{ohm} + V_{diff} \tag{1.6}$$

Activation losses V_{act} are due to the electrochemical reactions activation, which require a shift from the thermodynamic equilibrium [26] and are the main type of losses at low current density. Ohmic losses V_{ohm} are due to the ionic (mainly) and electric resistance of the cell. They are governed by Ohm's law and are predominant at intermediate currents. Concentration (or diffusion) losses V_{diff} are due to the mass transport limitations occurring at very high current densities, like gas bubbles that can block the active cell area. Generally, in PEM electrolyzers they are negligible. The current – voltage relationship is depicted by polarization curves (Figure 1.5).

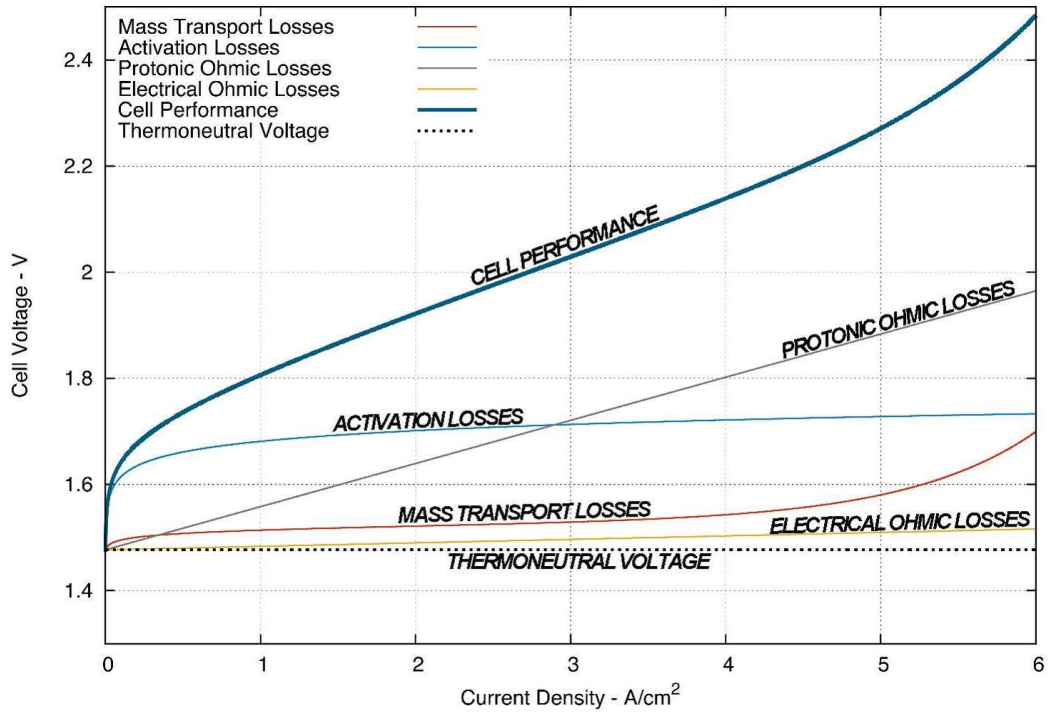

Figure 1.5 – Typical polarization curve of a PEM electrolyzer and its various contributions

The hydrogen production rate is proportional to the current density, according to the Faraday's law. Anyway, the ideal hydrogen production rate $\dot{n}_{H_2}$ [kmol/s] has to be corrected by means of the Faradaic efficiency η_F [-], defined as the ratio between the real hydrogen production rate and the ideal one:

$$\dot{n}_{H_2} = \eta_F \frac{I}{2F} \tag{1.7}$$

where I [A] is the cell current, computed as the current density times the cell area. Faradaic efficiency is lower than one because of the parasitic current losses along the gas ducts (not relevant for PEMEL) and product gases cross permeation [25], which is proportional to both the temperature and the pressure. This loss has a higher weight at low currents due to the lower hydrogen production [27].

1.4.2 State of the art and future perspectives

The Fuel Cells and Hydrogen Joint undertaking, under the EU's programme Horizon 2020 has defined key performance indicators for flexible electrolysis, in order to indicate how the technology is performing relatively to some specific targets that make up the challenge towards a fully operational and sustainable hydrogen economy [28].

Table 1.1 – SoA and future targets for PEM electrolysis using renewable electricity sources

No	Parameter	Unit	State of the art		FCH-JU target		
			2012	2017	2020	2024	2030
Generic system							
1	Electricity consumption @nominal capacity	kWh/kg	60	58	55	52	50
2	Capital cost	€/(kg/d) (€/kW)	8000 (~3000)	2900 (1200)	2000 (900)	1500 (700)	1000 (500)
3	O&M cost	€/(kg/d)/yr	160	58	41	30	21
Specific system							
4	Hot idle ramp time	sec	60	10	2	1	1
5	Cold start ramp time	sec	300	120	30	10	10
6	Footprint	m^2/MW	-	120	100	80	45
Stack							
7	Degradation	%/1000hrs	0,375	0,250	0,190	0,125	0,12
8	Current density PEM	A/cm^2	1,7	2,0	2,2	2,4	2,5
9	Use of critical raw materials as catalysts	mg/W	-	5,0	2,7	1,25	0,4

Great focus is placed on the cost reduction when talking about PEM electrolysis. In fact, while the targets on flexibility and operation are almost reached (PEM electrolyzer systems have been certified to provide primary reserves [21, 22]), hydrogen production from water electrolysis is still expensive from both CAPEX and OPEX perspectives if compared to fossil-fuel based hydrogen production. In 2020

hydrogen production cost from electrolysis is about 6 USD/kg_{H2} (assuming an electricity price of USD 50/MWh, 3200 equivalent hours for the electrolyzer and a WACC of 10%), while gray hydrogen from natural gas has a production cost oscillating between 1 and 2.5 USD/kg, mainly depending on the natural gas price [31]. According to IRENA, there is an unexploited potential for cost reduction up to 80% in the long term, and identified as main drivers the decrease in the electricity cost (reconfirming the need to exploit low-cost renewable sources), the reduction in the electrolyzer cost (achievable by the introduction of economies of scale, automation, technological progresses and increase in the components availability) and the increase in the electrolyzer efficiency [32], which is the main topic of this work.
Nowadays, the main R&D areas on PEM electrolyzers are catalysts and membrane design (targets are the increase in the cell current density, cell efficiency, cell operating pressure, rangeability and durability), the balance of plant (the target is increasing the system performances, flexibility and capital cost reduction), the MEA and porous transport layer (focus on increasing the stack unit size, specific cost and electrode area) and the possibility of increasing the operating temperature (target is 80 °C) [32].

1.4.3 Current projects involving PEMEL technology

Global hydrogen demand is rising, and it's expected to significantly increase in the future [25], amounting at around 70 Mtons/y nowadays, mainly for refining, ammonia, methanol and DRI (Direct Reduced Iron) steel production. Although at present only approximately 4% of the hydrogen produced worldwide comes from renewable sources, in the last few years the total amount of new installed electrolyzer capacity has grown considerably, from 1 MW installed in 2010 to the 25.4 MW installed in 2019 [34]. This growth is accompanied by an increase in the size of projects, from a typical size of 0.5 MW in the early 2010s, to sizes up to 6 MW in 2019. As alkaline electrolyzers are the most mature technology, and hence dominate the market, PEM electrolyzers enjoy a faster growth rate, and more and more projects are opting for this technology [27, 28] (Figure 1.6).

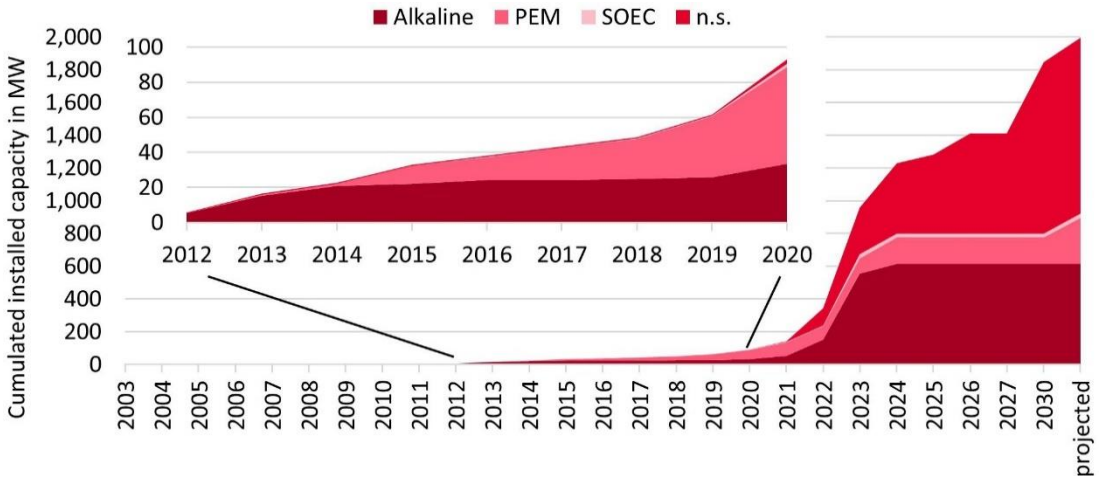

Figure 1.6 - Cumulative installed capacity according to electrolyzer type. n.s., not specified [36]

A brief review of few of the most relevant green hydrogen projects involving proton-exchange membrane electrolyzers realized or planned from 2019 to 2023 is presented below.

H2FUTURE (6 MW, 2019)

In November 2019, the world's largest PEM pilot plant with a capacity of 6 MW, part of the EU-founded H2FUTURE project in partnership with Siemens, started operation at the voestalpine steel manufacturer site in Linz, Austria (Figure 7). The aim of the project is the steel production process decarbonization, by exploiting the 1200 Nm^3/h of green hydrogen produced by 100% renewable sources, but also investigating on the potential of such plants in providing grid services and balancing electricity fluctuations. In order to fully decarbonize the voestalpine plant it would be required 340.000 tons of green hydrogen per year (plus the use of green electricity for those processes not viable using hydrogen as energy carrier), which is more than 400 times the H2FUTURE plant capacity, since about 57 kg of hydrogen are required to produce 1 ton of "green steel", H2FUTURE states [37].

Figure 1.7 – Picture of the H2FUTURE PEM electrolysis system

REFHYNE (10 MW, 2020)

The world's largest PEM electrolyzer in 2020, with a capacity of 10 MW, is built by ITM Power in the context of industrial refinery application for the REFHYNE Project, funded by the European Commission's Fuel Cells and Hydrogen Joint Undertaking (FCH JU). The plant, with a capacity of 1300 tons of hydrogen per year, is operated

by Shell and provides green hydrogen for processing and upgrading products (e.g. desulphurization processes of fossil fuels) at the Shell Rhineland Refinery in Wesseling, Germany. The project aims also in testing and exploring the PEM technology and the application in different sectors, such as heating or transportation [38]. The electrolyzer is operated at a highly responsive mode, providing a balancing service for the refinery's internal electricity grid and selling Primary Control Reserve service to the German Transmission System Operator. The plant started operation in July 2021 and has been designed as the first block of a modular plant, with the option of installing up to 100 MW of electrolyzer capacity [39].

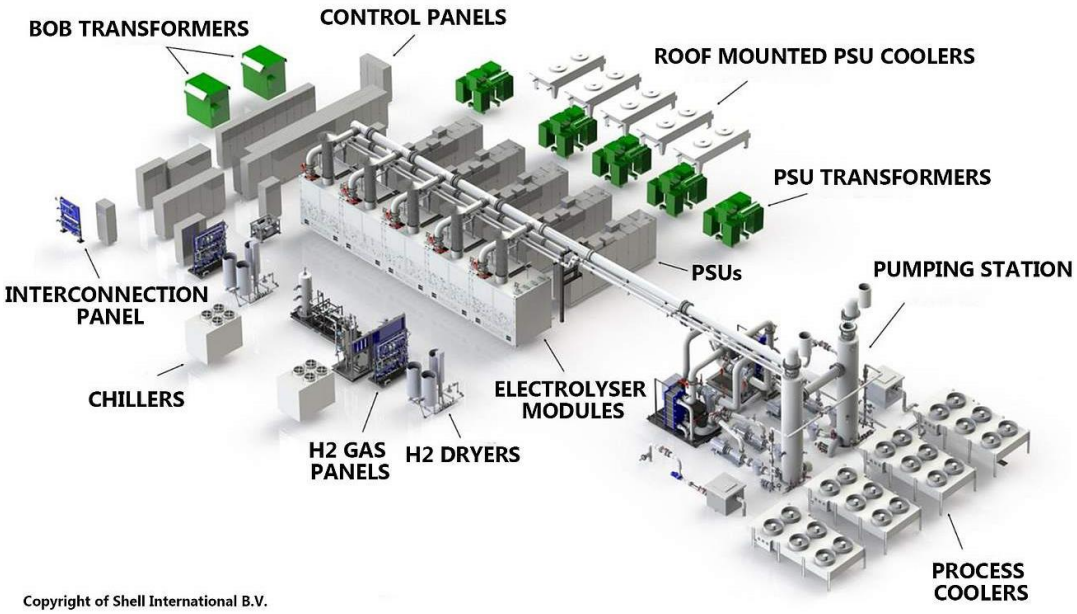

Figure 1.8 - 3D representation of the Refhyne power-to-gas plant

Air Liquide's Bécancour hydrogen production complex (20 MW, 2021)

In January 2021, Air Liquide completed the new largest electrolysis plant based on PEM technology in Bécancour, Québec, in proximity to the main industrial markets in Canada.

The 20 MW PEM electrolyzer is composed by four 5 MW HyLYZER 1000-30 pressurized skids realized by US-based Cummins with Hydrogenics technology, and aims at providing low-carbon hydrogen for industrial use and mobility, increasing by 50% the production capacity of Air Liquide's Bécancour hydrogen production complex. The choice of the site is based both on the proximity to the industrial and hydrogen mobility markets developing in North America and to the abundant renewable power available from the Hydro-Quebec hydroelectric plants. The facility will have an annual hydrogen output of about 3000 tons [40].

Eyre Peninsula Gateway Project (75 MW, 2022)

Among the future projects it's worth citing the Eyre Peninsula Gateway Project, in southern Australia, developed by H2U and supported by the South Australian Government's Renewable Technology Fund.
The project will be built in two stages, the initial demonstration stage will integrate a 75 MW PEM electrolysis plant for ammonia production, with a production capacity of 120 tons/day of green ammonia, and for export of green hydrogen to Japan and other North Asian economies. The second stage of the project plans a further expansion of the electrolysis and ammonia production capacity up to 2400 tons/day of green ammonia, equivalent to 1.5 GW of electrolysis capacity and 200.000 tons of hydrogen per year. The feasibility, site selection and preliminary planning activities of the demonstration phase have already been concluded and the project is now progressing with the front-end engineering and design, awarded by Worley in March 2021. In April 2021, RWE Supply & Trading and H2U announced the signing of a Memorandum of Understanding to develop green hydrogen trading links between Australia and Germany. Planned for completion in late 2022, the cost of the demonstration stage is estimated at 240 million AUD$. South Australia has a competitive advantage for green hydrogen production, with over 51% of renewable electricity generation in 2018 and high quality wind and solar resources [41], allowing a low cost for green hydrogen. The plant will use 100% of renewable energy from wind pharms and solar photovoltaic plants, provide balancing services to the national electricity system and fast frequency response support to the new solar plants in the Peninsula [42].

HyBridge (100 MW, 2023)

HyBridge will be the first large-scale power-to-gas plant in Germany, with an electrolyzer capacity of 100 MW.
Developed by Amprion and Open Grid Europe, it is planned to be located in southern Emsland, where there is an ideal intersection between the electricity grid and the natural gas grid (Figure 1.9). In fact, the project is proposed as part of the solution to the problem of balancing the grid and as a flexible user of the overproduction of renewable electricity that is expected in the upcoming years, planning to inject the hydrogen produced from renewable energy into the natural gas grid.
Different hypothesis are being evaluated, from converting part of the existing gas network for the exclusive transport of pure hydrogen, that can be used by the industries located near the pipeline, to the possibility of building hydrogen storage facilities, in order to temporally decouple the renewable electricity supply from the hydrogen demand, to the building of recharge stations for hydrogen vehicles, to the blending of the natural gas (mixing hydrogen and natural gas in the gas pipeline) with the hydrogen, limiting the share of hydrogen in compliance with the current regulations or even to use the hydrogen to produce synthetic methane by means of the methanation process, using the carbon dioxide captured from exhaust gases of industrial processes and producing green methane that can be easily fed into the existing natural gas transport and storage facilities. Currently the project is in the approval stage and, if the

regulatory authorities will consent the construction, the plant is expected to start operation in 2023 [43].

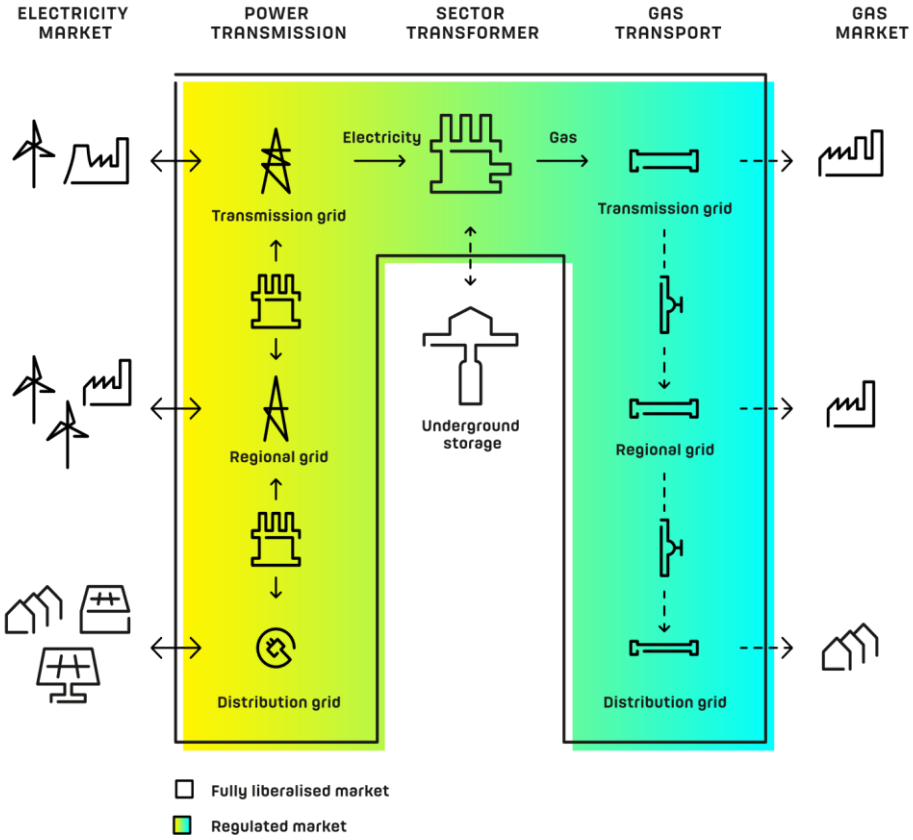

Figure 1.9 – Schematic of the "bridge" concept between electricity grid and gas grid of the Hybridge project in Germany [43]

As it is possible to notice from the previous paragraphs, from the late 2010s PEM technology has gained a huge development. In fact, the maximum size of the new projects is more than doubling every year, leading to an exponential growth of the total installed capacity.

1.5 Thesis outline

In this thesis a dynamic model of a PEM electrolysis system, based on a 60 kW commercial unit and developed in MATLAB Simulink® in a previous work, is analyzed, improved and validated by the use of data available from a previous experimental campaign. Appropriate modifications are made to the model in order to achieve a satisfactory degree of accuracy in predicting the operation of the actual system. The complete description of the system and of its modelling, inclusive of all its auxiliary components and already updated with the modifications here introduced, is presented in chapter 2.

The datasets used for the validation of the model, and the validation process itself are described in chapter 3. The validation includes the electrochemical behavior of the PEM stack (polarization curves), thermal dynamic behavior of the system, pressure dynamics and performances at full and partial load.
After the validation of the Simulink model is completed, in chapter 4 the model is used as tool to investigate different possible strategies to enhance system performances, in particular when operating at partial load, very frequent condition when the system is coupled with renewables.
This thesis, in fact, aims to give its small contribution to the research aimed at improving the efficiency of such systems, one of the three drivers of green-hydrogen production cost reduction [32], as already treated in section 1.4.2, as well as one of the two main paths identified by the scientific community for GHG reduction ([15], Figure 1.1).

2

CHAPTER 2 – MODEL DESCRIPTION

This chapter describes the system model, implemented in MATLAB Simulink, including the stack and all the main BoP components. The objective of this model is the investigation of the dynamic behavior of the complete system, focusing on BoP optimization. Consequent assumptions and simplifications of single component models are presented in the next sections.
The original model described is set up by Eng. Elena Crespi, except when explicitly stated for the parts and components which I added and/or corrected in this thesis work. A synthetic description of the model has been also published in [44]. The description of the parts already existing before my work has the aim of making this work the most complete as possible and to fully comprehend which are the assumptions and considerations within the conclusions of this work live.

2.1 Electrolysis system layout

The electrolysis system, represented in Figure 2.1, is composed, apart from the stack (section 2.2), of a number of BoP components that allow its correct operation and to control the processes involved in the system. A circulation pump (section 2.9) controls the mass flow rate of water, which is a fixed value, entering the stack on the anode side. In order to control the stack temperature, before entering the stack the water is chilled, passing through a heat exchanger (section 2.7). The water exits the stack enriched with oxygen, passes through resin filters which have the function of purifying it from any ions formed in the stack, and enters the oxygen – water phase separator (section 2.3), which collects the water in order to re-send it to the stack, realizing a loop. The pressure control of the oxygen – water separator is ensured by a backpressure valve, regulating the oxygen flow exiting the tank and vented outside the system. The oxygen flow exiting the system is saturated with water vapor, thus, the amount of water inside the oxygen – water separator is controlled by a water refill, implemented by a pump, pumping intermittently deionized water from the deionized water tank (section 2.6), serving as water storage and refilled from the outside.

On the cathode side of the stack, a flow of water–saturated hydrogen gas is generated. This gas enters the hydrogen – water separator (section 2.4) where it encounters a first drying process, by means of heat removal. The level of the liquid water collected on the bottom of the hydrogen – water phase separator is controlled by an intermittent purge of water, which is purified from the dissolved hydrogen and sent back to the deionized water tank. The partly-dried hydrogen reaches out a further drying process in a PSA (Pressure Swing Adsorption) system (section 2.5). The pressure in the PSA system and upstream units is controlled by a backpressure valve.
The electrolysis system is supplied with 3-phase alternated current. Part of this current is sent to the auxiliaries of the system, as pumps (section 2.9) and fans, working with AC current, while the rest is sent to the rectifier, which converts AC current into DC current so as to provide the power to feed the stack.
The electrical power to feed the chiller is supplied separately, from the electrical grid, as this component is external to the electrolysis system.

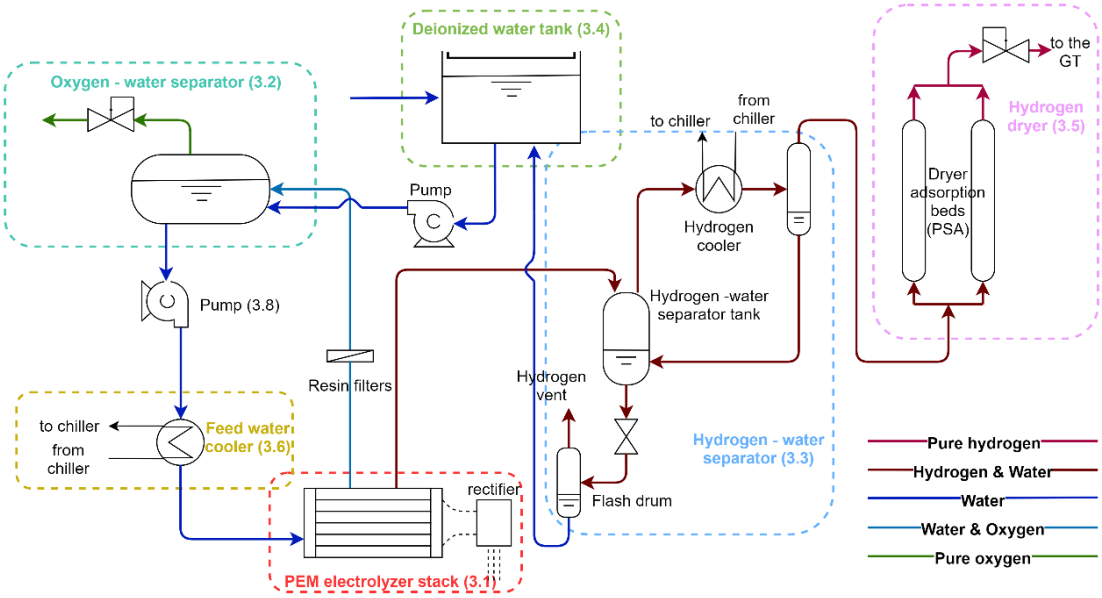

Figure 2.1 - Process flow diagram of the electrolyzer system

2.2 PEM Electrolyzer stack

The electrolyzer stack is composed by a given number of cells, fluid dynamically connected in parallel and electrically connected in series, in order to obtain higher voltages, while keeping the same current:

$$V_{stack} = V_{cell} \cdot N_{cells} \tag{2.1}$$

The model of a single cell is developed following a lumped model approach. The model receives as input feed-in water temperature, composition and mass flow rate, cathode and anode pressure, and the current supplied to the stack.

The following assumptions are made:

- The temperature dynamic of the stack is taken into account by the thermal capacity of the stack, considered as a constant;
- The fluids entering the stack reach immediate thermal equilibrium with it;
- Gas accumulation in cells channels is neglected since the volume of the channels is negligible with respect to the volume of other system components where mass built-up is allocated (i.e. oxygen-water and hydrogen-water separation tanks);
- Pressure drops in the cell's channels are neglected;
- Gas mixtures behave like ideal mixtures of ideal gases.

The model is divided into three subsystems; an electrochemical model, a fluid dynamic model and a thermodynamic model.

2.2.1 Electrochemical model

The electrochemical model computes the cell voltage and power, knowing the current supplied to the stack. Power is computed as:

$$P_{stack} = V_{stack} \cdot I_{stack} = N_{cells} \cdot V_{cell} \cdot I_{stack} \tag{2.2}$$

while cell voltage V_{cell}, the voltage that the electrochemical reaction needs to take place, is computed through semi-empirical current density – voltage polarization curves where the cell voltage is given by the sum of the ideal voltage and overpotentials (losses), i.e. additional voltage required in real conditions:

$$V_{cell}(T_{cell}, p_{cell}, i) = V_{ideal}(T_{cell}, p_{cell}) + \sum \Delta V_{cell}(T_{cell}, p_{cell}, i) \tag{2.3}$$

where i [A/cm^2] is the current density computed as the stack current (I [A]) divided by the cell area (A [cm^2]). The ideal voltage is the minimum cell voltage required for the reaction to take place in ideal conditions, also called 'open circuit voltage', and is computed through Nernst equation:

$$V_{ideal}(T_{cell}, p_{cell}) = \frac{\Delta G_{rev}(T_{cell}, p_{cell})}{n \cdot F} \tag{2.4}$$

where ΔG_{rev} [J/mol] is the variation in the Gibbs free energy, F is the Faraday constant (96485 C/mol), n is the number of electrons involved in the reaction per each H_2 molecule ($n = 2$). The variation in Gibbs free energy is pressure-dependent, thus equation (2.3) is divided in two terms, the first one representing the ideal voltage at reference pressure (p_{ref}) and the second one accounting for the voltage variation with pressure:

$$V_{ideal}(T_{cell}, p_{cell}) = \frac{\Delta G_{rev}(T_{cell}, p_{ref})}{n \cdot F} + \frac{R \cdot T_{cell}}{n \cdot F} \ln\left(\frac{a_{H_2} \cdot a_{O_2}^{0.5}}{a_{H_2O}}\right) \tag{2.5}$$

where a_{H_2}, a_{O_2} and a_{H_2O} are the activities of hydrogen, oxygen and water. The activity of gases is approximated by their partial pressure while water, fed into the cell as liquid, has an activity of 1.
Being the water both at cathode and at anode chambers in liquid phase, the vapor phase is accounted at its saturation pressure [45], hence, oxygen and hydrogen partial pressures are computed as:

$$p_{H_2} = p_{cathode} - p_{sat@T_{stack}} \tag{2.6}$$

$$p_{O_2} = p_{anode} - p_{sat@T_{stack}} \tag{2.7}$$

where $p_{cathode}$ [bar] and p_{anode} [bar] are the cathode and anode pressure respectively and $p_{sat@T_{stack}}$ [bar] is the partial pressure of water in saturation condition at stack temperature, computed by means of the Wagner-Pruss equation [46], valid for temperature values ranging from water triple point (T_{tr} = 273.16 K) to the critical point (T_{cr} = 647.096 K, p_{cr} = 220.64 bar):

$$p_{sat@T}\ [\text{bar}] = p_{cr}[bar] \cdot e^{\frac{b_1 \cdot \theta + b_2 \cdot \theta^{1.5} + b_3 \cdot \theta^3 + b_4 \cdot \theta^{3.5} + b_5 \cdot \theta^4 + b_6 \cdot \theta^{7.5}}{1-\theta}} \tag{2.8}$$

$$\theta = 1 - \frac{T[K]}{T_{cr}[K]} \tag{2.9}$$

where the values of the polynomial Eq. (2.8) for hydrogen are taken from the literature.
Overpotentials account for activation losses, ohmic losses, concentration losses and parasitic losses:

$$\sum \Delta V_{cell}(T_{cell}, p_{cell}, i) = \Delta V_{act} + \Delta V_{ohm} + \Delta V_{conc} + \Delta V_{par} \tag{2.10}$$

The activation overpotential (ΔV_{act}), the additional voltage for the activation of the electrochemical reaction, is represented in detail by the Butler-Volmer equation which applies the activated complex theory to the two half reactions, relating the current density to the activation overpotential at each electrode:

$$i = i_{0,X} \cdot \left(exp\left(\frac{\beta_x \cdot n \cdot F \cdot \Delta V_{act,X}}{R \cdot T_{cell}} \right) - exp\left(\frac{(\beta_x - 1) \cdot n \cdot F \cdot \Delta V_{act,X}}{R \cdot T_{cell}} \right) \right) \tag{2.11}$$

where X is either the cathode or the anode, $i_{0,X}$ [A/cm^2] is the exchange current density of the half-reaction occurring at electrode X, representing the reactivity of the electrode (electrode readiness to proceed with the electrochemical reaction) [7] and β_x is the electrode symmetric factor, representing the fraction of the additional energy going towards reduction, the complementary term $1 - \beta_x$ represents the additional energy going towards oxidation.

From Eq. (2.11), several assumptions can be made in order to express the activation overvoltage as a function of the other variables [6]. In the original model the second term of Eq. (2.11) is assumed negligible and Tafel equation is derived:

$$\Delta V_{act,X} = \frac{R \cdot T}{\alpha_x \cdot n \cdot F} \cdot \ln\left(\frac{i_X}{i_{0,X}}\right) \tag{2.12}$$

where α_x is the charge transfer coefficient, varying between 0 and 1. This equation is anyway valid only assuming sufficiently high activation overvoltage (high current density) [6], leading to high errors on voltage evaluation. Hence, it is substituted by another expression derived from eq. (2.11) assuming symmetry in the processes of the electronic transfer, equally distributed charge (charge transfer coefficient α_x equal to 0.5) [6]:

$$\Delta V_{act,X} = \frac{R \cdot T}{F} \cdot \sinh^{-1}\left(\frac{i_X}{2 \cdot i_{0,X}}\right) \tag{2.13}$$

Finally, the exchange current density dependence on temperature, which is in the original model fixed, is now expressed as [39, 40]:

$$i_{0,X} = i_X^{ref} \cdot exp\left(-\frac{E_{act,X}}{R \cdot T}\right) \tag{2.14}$$

where i_X^{ref} [A/cm^2] is the pre-exponential factor and $E_{act,X}$ [J/mol] is the activation energy for anode and cathode, respectively. Eventually, cathode activation overpotential is neglected because it's much smaller than the one of the anode.
The ohmic overpotential ΔV_{ohm} [V] is determined by electric resistance to the flow of electrons through electrical components (electrodes) and by the resistance of the membrane to the flow of protons. It is modeled through Ohm's law:

$$\Delta V_{ohm} = \left(R_{el,anode} + R_{el,cathode} + R_{mem}\right) \cdot i \cdot A_{cell} \tag{2.15}$$

Where i [A/cm] is the current density, A_{cell} [cm^2] is the cell active area, $R_{el,anode}$ [Ω] and $R_{el,cathode}$ [Ω] are the electrical resistance of anode and cathode:

$$R_{el,X} = \frac{t_{el,X}}{A_{cell}} \rho_{el,X} \tag{2.16}$$

with $t_{el,X}$ [cm] the thickness of either anode or cathode and $\rho_{el,X}$ [$\Omega \cdot cm$] the resistivity of either anode or cathode, while R_{mem} [Ω] is the membrane resistance to the flow of protons:

$$R_{mem} = \frac{t_{mem}}{\sigma_{\mathrm{mem}} \cdot A_{cell}} \tag{2.17}$$

with t_{mem} [cm] the membrane thickness and σ_{mem} [S/cm] the proton conductivity of the membrane, evaluated by means of the Springer model [47], valid for Nafion® 117, accounting for the temperature dependence and the humidification level λ, assumed to be around 22 [48] for fully hydrated membrane (but neglecting the dependence on the proton concentration and the diffusivity coefficient):

$$\sigma_{mem} = (0.005139\,\lambda - 0.00326)\,exp\left(1268\,\left(\frac{1}{303}\cdot\frac{1}{T_{cell}}\right)\right) \tag{2.18}$$

The concentration (or diffusion) overpotential ΔV_{conc} [V], representing mass transfer limitation, is generally referred to all reactants and all products at each electrode but, for PEM electrolyzers, the main resistance to mass transfer is due to the oxygen gas bubbles forming at the anode that could limit the water molecules contact with the anode at very high currents. These losses are hence modelled by defining a limiting current density (i_L assumed to be equal to 6 A/cm^2 as suggested in [49]) and considering only anode side:

$$\Delta V_{conc} = \frac{RT}{\alpha_{anode} nF}\,ln\left(\frac{i_L}{i_L - i}\right) \tag{2.19}$$

Finally, parasitic overpotential (ΔV_{par} [V]) represents losses due to undesired short-circuit current and crossover phenomena in the cell, increasing the electrical consumption due to a reduction in the net hydrogen production. In the present model this loss is not modeled as an overpotential but as a current variation, through the Faradaic efficiency [50], already introduced in section 1.4.1, defined as:

$$\eta_F = \frac{i_{useful}}{i_{cell}} \tag{2.20}$$

Experimental evidences show that Faradaic efficiency is close to 1, and it's assumed to be equal to 0.99, as suggested in [50], in the original model and in the first part of the validation. Anyway, a more precise evaluation of the Faradaic efficiency is introduced at the end of the validation chapter (section 3.4.2) by means of a simplified model accounting for the Faradic efficiency dependence on the current density, since considering a fixed value for this efficiency will be demonstrated to lead to a high deviations on the real behavior at low partial loads (i.e. low current densities).

2.2.2 Fluid dynamic model

The fluid dynamic model solves mass balances, knowing flow rate and composition of the flows entering the stack, in order to determine flow rate and composition of the streams leaving the anode and the cathode. Mass conservation equations are solved for each chemical species *j* (H_2, O_2, H_2O) neglecting gas accumulation in the cell channels

since, as already explained, the volume of the cell channels is negligible with respect to the volumes (tanks and separators) where considerable accumulations occur:

$$\dot{m}_{j,X,out} = \dot{m}_{j,X,in} - \dot{m}_{j,X,cons} + \dot{m}_{j,X,prod} - \dot{m}_{j,X,trans} \tag{2.21}$$

where $\dot{m}_j$ is the mass flow rate [kg/s] of the chemical species *j*, *X* is either the anode or the cathode, *cons* stands for consumed, *prod* stands for produced and *trans* stands for transferred. The only inlet stream is water at the anode (2.22) and the only production terms are hydrogen at the cathode (2.23) and oxygen at the anode (2.24), while water is consumed at the anode:

$$\dot{m}_{H_2,cat,prod} = \frac{i_{usefull}}{2F} \cdot A_{cell} \cdot N_{cells} \cdot MM_{H_2} \tag{2.22}$$

$$\dot{m}_{o_2,an,prod} = \frac{\frac{\dot{m}_{H_2,cat,prod}}{MM_{H_2}}}{2} \cdot MM_{O_2} \tag{2.23}$$

$$\dot{m}_{H_2O,an,cons} = \frac{\dot{m}_{H_2,cat,prod}}{MM_{H_2}} \cdot MM_{H_2O} \tag{2.24}$$

where F = 96485 C/mol is the Faraday constant, $i_{usefull}$ is the useful current density in A/cm^2 , A_{cell} is the active area of one cell in cm^2 and N_{cells} is the total number of cells in the stack.
Water is assumed to be the only transferred substance, whose transport from anode to cathode is the result of three transport mechanisms; the transport of water molecules from anode to cathode by hydrogen ions called electro-osmotic drag, the diffusion driven transport, determined by the difference in water concentration between cathode side and anode side of the membrane, and pressure driven transport, caused by the pressure difference between cathode side and anode side of the membrane:

$$\dot{m}_{H_2O,an,trans} = \dot{m}^{eod}_{H_2O,trans} + \dot{m}^{diff}_{H_2O,trans} + \dot{m}^{\Delta p}_{H_2O,trans} \tag{2.25}$$

$$\dot{m}_{H_2O,cat,trans} = -\dot{m}_{H_2O,an,trans} \tag{2.26}$$

where *eod* stands for electro-osmotic drag, *diff* stands for diffusion and Δp stands for pressure driven.

Electro-osmotic drag is computed as [48], [51]:

$$\dot{m}^{eod}_{H_2O,trans} = \frac{n_d \cdot i_{usefull} \cdot A_{cell} \cdot N_{cells}}{F} \cdot MM_{H_2O} \tag{2.27}$$

where $n_d \left[\frac{mol_{H_2O}}{mol_{H^+}}\right]$ is the electro-osmotic drag coefficient, depending on temperature, current density and pressure [52]:

$$n_d = 0.0029 \cdot \lambda^2 + 0.05 \cdot \lambda - 3.4 \cdot 10^{-19} \tag{2.28}$$

The diffusion driven transport is modelled as [53]:

$$\dot{m}^{diff}_{H_2O,trans} = \frac{A_{cells} \cdot N_{cells} \cdot D_w}{t_{mem}} \left(C^{anode}_{H_2O,mem} - C^{cathode}_{H_2O,mem}\right) \cdot \ MM_{H_2O} \tag{2.29}$$

where D_w is the water diffusion coefficient in the membrane, t_{mem} [cm] the membrane thickness, $C^{anode}_{H_2O,mem}$ and $C^{cathode}_{H_2O,mem}$ the water concentration on the membrane at anode and cathode side respectively computable by means of the Fick's law of diffusion:

$$C^{cathode}_{H_2O,mem} = C^{cathode}_{H_2O,channel} + \frac{t_{anode} \cdot \dot{n}_{H_2O,anode,trans}}{D^{cathode}_{eff} \cdot A_{cell}} \tag{2.30}$$

$$C^{anode}_{H_2O,mem} = C^{anode}_{H_2O,channel} - \frac{t_{anode} \cdot \left(\dot{n}_{H_2O,anode,trans} + \dot{n}_{H_2O,anode,cons}\right)}{D^{anode}_{eff} \cdot A_{cell}} \tag{2.31}$$

where D^{anode}_{eff} and $D^{cathode}_{eff}$ are O_2-H_2O and H_2-H_2O effective binary diffusion coefficients [53], obtained by applying the porosity correction to the binary diffusion coefficient:

$$D^{cathode}_{eff} = D_{H_2-H_2O} \cdot \varepsilon \cdot \left(\frac{\varepsilon - \varepsilon_P}{1 - \varepsilon_P}\right)^{\alpha} \tag{2.32}$$

$$D^{anode}_{eff} = D_{O_2-H_2O} \cdot \varepsilon \cdot \left(\frac{\varepsilon - \varepsilon_P}{1 - \varepsilon_P}\right)^{\alpha} \tag{2.33}$$

where ε is the porosity coefficient (assumed equal to 0.3), ε_P is the percolation threshold (assumed equal to 0.11), α is an empirically determined coefficient, assumed to be 0.785 and $D_{H_2-H_2O}$ and $D_{O_2-H_2O}$ are the binary diffusion coefficients of hydrogen-water mixture and oxygen-water mixture. The binary diffusion coefficient of a mixture of two substances A and B can be computed as:

$$D_{A-B} = \frac{a}{p}\left(\frac{T}{\sqrt{T_{cr,A} \cdot T_{cr,B}}}\right)^{b} \left(p_{cr,A} \cdot p_{cr,B}\right)^{\frac{1}{3}} \left(T_{cr,A} \cdot T_{cr,B}\right)^{\frac{5}{12}} \left(\frac{1}{MM_A} + \frac{1}{MM_B}\right)^{\frac{1}{2}} \tag{2.34}$$

where p [atm] is the pressure, T [K] is the temperature p_{cr} is the critical pressure, T_{cr} is the critical temperature, MM the molecular mass and a and b are non-dimensional coefficients, equal to $3.64 \cdot 10^{-4}$ and 2.334 respectively for water-nonpolar gas pairs.

Finally, pressure driven transport can be calculated as [42, 47]:

$$\dot{m}_{H_2O,trans}^{\Delta p} = \frac{k_{Darcy} \cdot A_{cell} \cdot \rho_{H_2O} \cdot (p_{anode} - p_{cathode})}{t_{mem} \cdot \mu_{H_20}} \tag{2.35}$$

where k_{Darcy} is the membrane permeability to water.

2.2.3 Thermodynamic model

The thermodynamic model subsystem determines the temperature of the stack and of the streams leaving the stack, solving the dynamic global energy balance over the stack:

$$\dot{H}_{in} - \dot{H}_{out} - \dot{Q}_{loss} + P_{stack} = C_{stack} \frac{dT_{stack}}{dt} \tag{2.36}$$

where $\dot{H}_{in}$ and $\dot{H}_{out}$ [kW] are the enthalpy fluxes entering and exiting the stack, computed as:

$$\dot{H}_{in} = \dot{m}_{in} \cdot h_{in} \tag{2.37}$$

$$\dot{H}_{out} = \dot{m}_{out} \cdot h_{out} \tag{2.38}$$

The enthalpy of the inlet and outlet streams, h_{in} and h_{out} [kJ/kg], are computed using NASA polynomials by knowing composition, temperature and pressure of the streams entering and leaving the stack. The streams leaving the stack are assumed to be at thermal equilibrium with it (so, having the same temperature of the stack). P_{stack} [kW] is the electrical power entering the stack, C_{stack} [kJ/K] is the stack overall heat capacity, which depends on the stack geometry and materials and is determined later on in this work by observing experimental data (paragraph 3.2.3 - Stack thermal capacity). Finally, $\dot{Q}_{loss}$ [kW] is the heat exchanged with the external environment, through the stack external walls. In the original model it is assumed to be zero, while now it is modelled as a convection problem:

$$\dot{Q}_{loss} = A \cdot h \cdot \Delta T \tag{2.39}$$

where A [m^2] is the external surface area of the stack exposed to air, ΔT [°C] is the difference between the stack external wall's temperature (assumed to be equal to T_{stack}) and h [W/m^2-K] the convection heat transfer coefficient, determined from the non-dimensional Nusselt number:

$$h = \frac{Nu \cdot k}{L} \tag{2.40}$$

where k [W/m-K] is the air thermal conductivity and L [m] is the characteristic length, depending on the geometry. The thermal conductivity of air is computed as $k = k(T_w)$ by linearly interpolating the value of k at different temperatures T_w [°C] available from literature, where T_w is the so called 'wall temperature', computed as the average

between the temperature of the external wall of the stack and the air temperature (ambient temperature). The non-dimensional Nusselt number Nu is computed by means of semi-empirical correlations for natural convection, depending on the geometry and orientation of the considered surface. Thus, two different Nusselt numbers are computed: one for the upper, horizontal surface and another one for the lateral walls of the stack. Heat losses from the bottom part of the stack, in contact with the skid's floor are neglected.
Nu is computed as function of non-dimensional Rayleigh Ra [-] number. The empirical correlation for the side walls, which are modelled as vertical plates, is [54]:

$$\begin{cases} Nu = 0.59 \cdot Ra^{\frac{1}{4}} & for\ 10^2 \leq Ra \leq 10^9 \\ Nu = 0.1 \cdot Ra^{\frac{1}{3}} & for\ 10^9 < Ra \leq 10^{13} \end{cases} \tag{2.41}$$

while empirical correlation for the upper wall, which is modelled as an horizontal hot surface, is [54]:

$$\begin{cases} Nu = 0.54 \cdot Ra^{\frac{1}{4}} & for\ 10^4 \leq Ra \leq 10^7 \\ Nu = 0.15 \cdot Ra^{\frac{1}{3}} & for\ 10^7 < Ra \leq 10^{11} \end{cases} \tag{2.42}$$

where Ra [-] is the product of the Grashoff Gr [-] and Prandtl Pr [-] non-dimensional numbers, Pr number is also calculated by means of linear interpolations based on T_w and literature data and Gr is computed as [54]:

$$Gr = \frac{g\rho^2\beta\Delta T L^3}{\mu^2} \tag{2.43}$$

where g [m/s^2] is the gravity acceleration (9.81 m/s^2), ρ [kg/m^3] is the air density, β [K^{-1}] is the inverse of T_w [K] expressed in Kelvin degrees, ΔT [°C] is the temperature difference between the external wall and ambient, μ [Ns/m^2] is the dynamic viscosity of air and L [m] is the characteristic length which is the wall height in case of the vertical walls and the surface area divided by its perimeter in the case of the horizontal upper surface. Both density and dynamic viscosity of air are temperature dependent and they are iteratively computed by linearly interpolating the literature data on T_w exactly as for Pr and k.

2.3 Oxygen-water separator

The oxygen-water separator receives the oxygen-enriched stream of water exiting the electrolyzer stack (anode side). Water and oxygen accumulate in the separator and separate via gravimetric separation. Vapor-liquid equilibrium is assumed to be always present in the tank, where vapor phase is assumed to be oxygen saturated with water, while oxygen solubility in water is neglected. The amount of oxygen dissolved in water is computed a posteriori in order to verify the validity of this assumption (see

section 2.4). A gas flow (water-saturated oxygen), driven by a backpressure valve which maintains a pressure of 1.7 bar_g inside the separator tank, is vented outside the system from the top of the separator. The liquid water, taken from the bottom, is sent back to the stack, realizing a recirculation which flow is controlled by a pump (centrifugal recirculation pump). Water is continuously lost because of the water-saturated oxygen venting and due to electrochemical reactions and water transport occurring in the electrolytic cells. Thus, the control system measures the level of liquid in the separator tank and, when the water is below a minimum level, a flow of water, is pumped from the deionized water tank (see section 2.6), through a positive displacement pump (section 2.9) into the oxygen-water separator in order to refill it with fresh water.

The separator model receives temperature, flow rate, composition and pressure of the inlet flows as input. Vapor composition is determined by considering the condition of saturation knowing tank pressure p_{tank} [Pa] and temperature T_{tank} [K]:

$$x_{H_2O,vap} = x_{sat@T_{tank},p_{tank}} \tag{2.44}$$

$$x_{O_2,vap} = 1 - x_{H_2O,vap} \tag{2.45}$$

The model solves dynamic mass balances:

$$\dot{m}_{inAnode} - \dot{m}_{outAnode} + \dot{m}_{refill} - \dot{m}_{vap,out} = \frac{dm_{acc}}{dt} \tag{2.46}$$

where $\dot{m}_{outAnode}$ [kg/s] and $\dot{m}_{inAnode}$ [kg/s] are the mass flow rate of anode feed-in water exiting the separator tank and the mass flow rate of water coming from the anode and entering the separator respectively, $\dot{m}_{refill}$ [kg/s] is the water flow refilling the tank, $\dot{m}_{vap,out}$ [kg/s] is the water-saturated oxygen gas flow exiting the tank and m_{acc} [kg] is the mass accumulated inside the tank. The amount of liquid and of vapor in the tank are computed knowing vapor composition and the volume of the tank occupied by water, assuming a constant density of liquid water of 1000 kg/m^3. The tank volume not occupied by water is filled with the gas, whose pressure is computed by assuming the gas as an ideal gas:

$$p_{tank} = \frac{m_{vap,acc} \cdot R_{gas} \cdot T_{tank}}{MM_{vap} \cdot V_{vap}} \tag{2.47}$$

Temperature is computed from tank enthalpy h_{tank}[kJ/kg] by solving energy balances, assuming a uniform temperature in the tank:

$$(\dot{m} \cdot h)_{inAn} - (\dot{m} \cdot h)_{outAn} + (\dot{m} \cdot h)_{refill} - (\dot{m} \cdot h)_{vap,out} - \dot{Q}_{loss} = \frac{dQ_{acc}}{dt} \tag{2.48}$$

$$\frac{dQ_{acc}}{dt} \approx \frac{d(m_{acc} \cdot h_{tank})}{dt} \tag{2.49}$$

$$h_{tank} = \int \frac{d(h_{tank})}{dt} \tag{2.50}$$

where enthalpy h [kJ/kg] of the inlet and outlet streams, are computed using NASA polynomials by knowing composition, temperature and pressure of the streams entering and leaving the tank. The streams leaving the tank are assumed to be at thermal equilibrium with it. $\dot{Q}_{loss}$ [kW] is the heat exchanged with the external environment, through the stack external walls. In the original model it is assumed to be zero, while now it is modelled as a convection problem:

$$\dot{Q}_{loss} = A \cdot h \cdot \Delta T \tag{2.51}$$

where A [m^2] is the external surface area of the tank exposed to air, ΔT [°C] is the difference between the tank external wall's temperature (assumed in equilibrium with the internal liquid) and the environment, and h [W/m^2-K] the convection heat transfer coefficient, determined from the non-dimensional Nusselt number:

$$h = \frac{Nu \cdot k}{L} \tag{2.52}$$

where k [W/m-K] is the air thermal conductivity and L [m] is the characteristic length, depending on the geometry. The thermal conductivity of air is computed as $k = k(T_w)$ by linearly interpolating the value of k at different temperatures T_w [°C] available from literature, where T_w is the so called 'wall temperature', computed as the average between the temperature of the external wall of the tank (considered at equilibrium with the liquid inside it) and the air temperature (ambient temperature). The non-dimensional Nusselt number Nu is computed by means of semi-empirical correlations for natural convection, depending on the geometry, as function of non-dimensional Rayleigh Ra and Prandtl Pr numbers. The oxygen-water separator is an horizontal cylinder, whose correlation for Nu calculation is [54]:

$$Nu = \left(0.6 + \frac{0.387 Ra^{1/6}}{\left(1 + \left(\frac{0.559}{Pr}\right)^{9/16}\right)^{8/27}} \right)^2 \tag{2.53}$$

where Ra [-] is the product of the Grashoff Gr [-] and Prandtl Pr [-] non-dimensional numbers, Pr number is also calculated by means of linear interpolations based on T_w and literature data and Gr is computed as [54]:

$$Gr = \frac{g \rho^2 \beta \Delta T L^3}{\mu^2} \tag{2.54}$$

where g [m/s^2] is the gravity acceleration (9.81 m/s^2), ρ [kg/m^3] is the air density, β [K^{-1}] is the inverse of T_w [K] expressed in Kelvin degrees, ΔT [°C] is the temperature difference between the external wall and ambient, μ [Ns/m^2] is the dynamic viscosity of air and L [m] is the characteristic length and, given the cylindrical geometry, it's the diameter of the cylinder. Both density and dynamic viscosity of air are temperature dependent and they are iteratively computed by linearly interpolating the literature data on T_w exactly as for Pr and k.

2.4 Hydrogen – water separator and annexed components

The hydrogen – water separator is a pressurized tank where wet hydrogen gas and liquid water accumulate and separate. Similarly to the oxygen-water separator (paragraph 2.3), it is fed by a wet flow exiting the stack (wet hydrogen from the cathode, in this case) where a first separation between hydrogen gas and water takes place. The flow exiting the cathode is assumed to be hydrogen saturated with water at the stack temperature, which composition is computed as for the oxygen – water separator (Eqs. (2.44) and (2.45) where oxygen is replaced with hydrogen), assuming that vapor – liquid equilibrium is always present. Hydrogen solubility in liquid water is instead neglected. Wet hydrogen exits from the upper part of the tank and passes through a heat exchanger which uses the cooling fluid to condensate part of the moisture $\dot{m}_{cond}^{H_2O}$ [kg/s] which, once collected by gravimetric separation into a secondary separator, is delivered back to the hydrogen-water separator, while the partially dried hydrogen is sent to the PSA drying unit (see section 2.5) in order to obtain highly pure hydrogen by further drying.

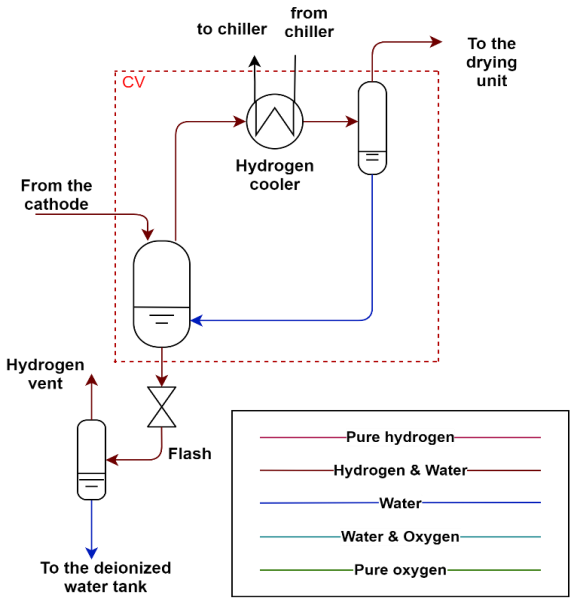

Figure 2.2 - Process flow diagram of the hydrogen - water separator and its annexed components

The Simulink model solves dynamic mass and energy balances (exactly as in the oxygen – water separator, section 2.3) in the control volume (red box in Figure 2.2) containing both the hydrogen – water separator tank and the heat exchanger:

$$\dot{m}^{vap}_{fromCathode} = \dot{m}^{H_2}_{fromCathode} + \dot{m}^{H_2O}_{fromCathode} \tag{2.55}$$

$$\dot{m}^{vap}_{fromCathode} - \dot{m}^{vap}_{out,H_2Chiller} - \dot{m}^{H_2O}_{cond} = \frac{dm^{vap}_{acc,tank}}{dt} \tag{2.56}$$

$$(\dot{m} \cdot y_{H_2O})^{vap}_{fromCath} - (\dot{m} \cdot y_{H_2O})^{vap}_{out,H_2Chiller} - \dot{m}^{H_2O}_{out,tank} = \frac{dm^{H_2O}_{acc,tank}}{dt} \tag{2.57}$$

$$(\dot{m} \cdot y_{H_2})^{vap}_{fromCath} - (\dot{m} \cdot y_{H_2})^{vap}_{out,H_2Chiller} = \frac{dm^{H_2}_{acc,tank}}{dt} \tag{2.58}$$

The level of the water inside the tank is controlled by intermittent purge of liquid water taken from the bottom of the tank with a fixed flow amount $\dot{m}^{H_2O}_{out,tank}$ [kg/s], modelled by a relay in the Simulink model, while the vapor flow rate exiting the hydrogen chiller $\dot{m}^{vap}_{out,H_2Chiller}$ [kg/s] is determined by the backpressure valve downstream of the PSA drying system, which is regulated to maintain the given pressure setpoint of the hydrogen. Thus, the value of the mass flow rate of vapor exiting the hydrogen chiller is computed by the Simulink model block described in section 2.5. The vapor accumulates at the top of the hydrogen – water separator tank and the liquid accumulates on the bottom. The mass accumulation is assumed to be concentrated in the hydrogen – water separator tank, whose volume is assumed to include also the PSA column volume, while mass accumulation in the hydrogen chiller is neglected, due to its lower volume:

$$m^{H_2O}_{acc,tank} = \int \frac{dm^{H_2O}_{acc,tank}}{dt} \tag{2.59}$$

$$m^{H_2}_{acc,tank} = \int \frac{dm^{H_2}_{acc,tank}}{dt} \tag{2.60}$$

$$m^{vap}_{acc,tank} = \frac{m^{H_2}_{acc,tank}}{1 - y_{H_2O,Sat}} \tag{2.61}$$

$$m^{H_2O,liq}_{acc,tank} = m^{H_2O}_{acc,tank} - m^{vap}_{acc,tank} \cdot y_{H_2O,Sat} \tag{2.62}$$

The heat subtracted by the heat exchanger is computed implementing a stationary model of the hydrogen cooler (introduced in this thesis work) which solves energy balances on the heat exchanger, computing the enthalpy of the moisturized hydrogen gas entering and exiting the heat exchanger by means of the NASA polynomials, the

amount of water that condenses, which is computed assuming both the entering and the exiting flows to be saturated with water:

$$\dot{m}_{cond}^{H_2O} = \dot{m}_{in}^{vap} \cdot y_{H_2O,Sat@T_{Tank}} - \dot{m}_{out}^{vap} \cdot y_{H_2O,Sat@T_{Chiller}} \tag{2.63}$$

$$(\dot{m} \cdot h)_{out,chiller}^{liq} = \dot{m}_{cond}^{H_2O} \tag{2.64}$$

$$(\dot{m} \cdot h)_{in,chiller}^{vap} - (\dot{m} \cdot h)_{out,chiller}^{vap} - (\dot{m} \cdot h)_{out,chiller}^{liq} = \dot{Q}_{out,Chiller} \tag{2.65}$$

The coolant fluid is assumed to be the same coolant of the stack feed-in water cooler (see section 2.7) which is cooled in an air cooled chiller, whose consumption $P_{chiller}$[W] is computed considering the heat removed $\dot{Q}$ [W] and assuming a constant COP = 3:

$$P_{chiller} = \frac{\dot{Q}}{COP} \tag{2.66}$$

The liquid water purge taken from the bottom of the tank is sent to a flash drum whose role is to lower the pressure of the water, purifying it from the hydrogen in order to send it back to the deionized water tank. The hydrogen released during this process is lost, therefore, in order to quantify it, the hydrogen dissolved in liquid water is computed a posteriori by means of the Henry's law:

$$\ln\left(\frac{K_H}{p_{H_2Osat,T}}\right) = \frac{A_H}{T_R} + \frac{B_H(1-T_R)^{0.355}}{T_R} + C_H T_R^{-0.41} e^{(1-T_R)} \tag{2.67}$$

where T_R [-] is the water reduced temperature, $K_H$is the Henry's constant, computed as a function of temperature accordingly to [55], [56], $p_{H_2Osat,T}$ [Pa] is the saturation pressure of water at the temperature T and A_H, B_H and C_H are regressed parameters. The impact of the dissolved hydrogen in the hydrogen – water separator tank is assumed negligible and verified *a posteriori*.

2.5 Hydrogen dryer (PSA)

This component is not present in the original model and it's introduced for the first time in the present thesis work. In order to obtain a high purity of the hydrogen produced, the electrolyzer is equipped with a dryer to further remove moisture from hydrogen after the first raw removal carried out in the hydrogen – water separator (section 2.4). The dryer consists in a batch system composed of two pressure swing adsorption (PSA) beds, working alternatively. The separation is based on the

difference in the physical binding force between the different gas molecules and the adsorbent material contained in the adsorption vessels. Highly volatile components with low polarity, such as hydrogen, are practically non-adsorbable if compared to molecules as N_2, CO, CO_2 and water vapor. The PSA process works at constant temperature and uses the effect of alternating pressure (and subsequently partial pressure) to perform adsorption and desorption. Adsorption is carried out at high pressure (~30 bar_g) until the maximum adsorption capacity of the adsorber is reached (equilibrium loading). At this point, the adsorption bed needs to be regenerated by lowering the pressure to slightly above the atmospheric pressure, resulting in a reduction of the equilibrium loading.

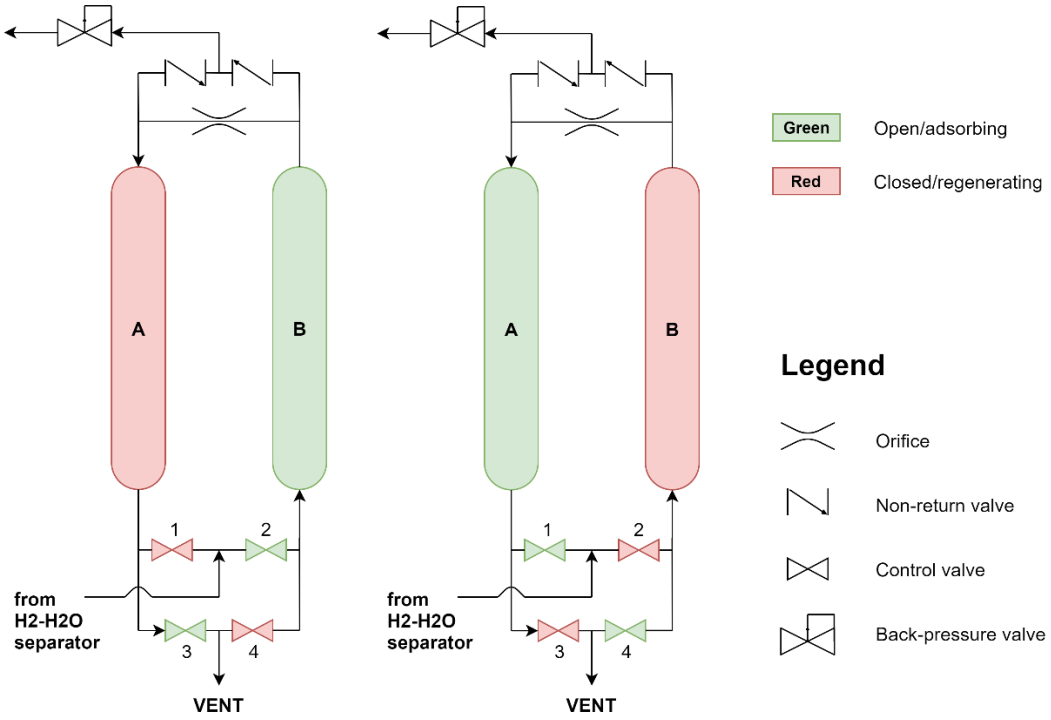

Figure 2.3 - Process flow diagram of the PSA showing the case with A regenerating/B adsorbing (left) and A adsorbing/B regenerating (right)

In particular, the pressure swing adsorption process is composed of four basic process steps:

- Adsorption
- Depressurization
- Regeneration
- Repressurization

In order to provide a continuous supply of purified hydrogen a minimum of 4 adsorption vessels are needed [57], in fact, this number allows to have at least always one bed working in absorption mode. Thus, the purified hydrogen supply presents

certain discontinuities. In Figure 2.3 the system is represented during the adsorption phase of the adsorption vessel "B" and the regeneration of the vessel "A" on the left, and vice versa on the right. As deductible from the figure, during the regeneration phase of the A bed, the valve "2" is open while the valve "4" is closed, forcing the hydrogen coming from the hydrogen – water separator to flow through the adsorbing bed "B". The purified hydrogen, which reaches a purity level of 99.9998%, exits from the top of the vessel and passes through the back-pressure valve. The back-pressure valve allows to control the pressure upstream of itself, down to the stack cathode, automatically regulating the hydrogen flow rate in order to keep the pressure upstream at 30 bar_g. The contemporaneous regeneration phase taking place for the "A" vessel is carried out by means of a purging process, consisting in the final removal of impurities at low pressure thanks to a stream of purified hydrogen coming from the adsorbing bed (this allows to obtain a very low partial pressure of impurities and a resulting low equilibrium loading). The pure hydrogen stream comes from the top of the adsorbing bed and it is orifice-driven. The pure hydrogen, passing through the regenerating vessel captures the impurities still contained in it, and thus needs to be vented out of the system by keeping valve "1" closed and valve "3" open. As adsorption and regeneration phases happen contemporaneously for the two beds, also the remaining two phases, depressurization and repressurization do so. In fact, after a certain amount of time (~18 minutes in our case) the active (adsorbing) bed reaches the maximum load and needs to be regenerated while the regenerating bed is completely regenerated, so they need to be "switched". This phase is very short in time (less than one minute) and mainly consists in opening valves "1" and "4" and closing valves "2" and "3", allowing the bed "A" to re-pressurize and the bed "B" to depressurize. A cycle is complete, and a new cycle can start with the bed "A" being the active one this time, while the bed "B" is set in regeneration mode. Knowing how the PSA works is important in particular to quantify the hydrogen losses occurring in it, losses which, as it will be lately explained in this work (section 3.4.2) heavily impact the performances of the electrolyzer.

Thus, a simplified stationary model of the PSA drying system, original of this thesis work, is implemented and used to simulate the hydrogen drying process and quantify its losses. The PSA is modelled as an isothermal system at the temperature of the moisturized hydrogen exiting the heat exchanger (i.e. entering the PSA) annexed to the hydrogen – water separator. This assumption is justified by the fact that, at the operating temperature of the PSA (20 – 30 °C), the saturation pressure of water is three orders of magnitude lower than the total pressure at which the PSA works, and so the molar fraction of the water in the gas flow entering the PSA is in the order of magnitude of 10^{-3}. Therefore, the latent heat of evaporation released by the water, condensing because of its adsorption by the PSA, is not capable of appreciably influence the temperature of the system, considered the mass flow rates and the thermal inertia of the system.

Mass balances are solved in order to compute the mass flow rate of the pure hydrogen exiting the heat exchanger and the mass flow rate of water entrained by the active

adsorption bed $\dot{m}_{adsorbed,PSA}^{H_2O}$ [kg/s] (assumed equal to the entire amount of water exiting the hydrogen cooler $\dot{m}_{out,H_2Cooler}^{H_2O}$ [kg/s]):

$$\dot{m}_{out,H_2Cooler}^{H_2} = \dot{m}_{out,orifice}^{H_2} - \dot{m}_{out,ELsystem}^{H_2} \tag{2.68}$$

$$\dot{m}_{out,H_2Cooler}^{vap} = \frac{\dot{m}_{out,H_2Cooler}^{H_2}}{y_{vap}^{H_2}} \tag{2.69}$$

$$\dot{m}_{adsorbed,PSA}^{H_2O} = \dot{m}_{out,H_2Cooler}^{H_2O} = \dot{m}_{out,H_2Cooler}^{vap} \cdot y_{vap}^{H_2O} \tag{2.70}$$

where $y_{vap}^{H_2}$ [-] and $y_{vap}^{H_2O}$ [-] are the mass fraction of hydrogen and the mass fraction of water in the vapor exiting the hydrogen cooler $\dot{m}_{out,H_2Cooler}^{vap}$ [kg/s], $\dot{m}_{out,H_2Cooler}^{H_2}$ [kg/s] is the mass flow rate of hydrogen exiting the hydrogen – water separator, $\dot{m}_{out,ELsystem}^{H_2}$[kg/s] is the mass flow rate of hydrogen exiting the electrolyzer (which boundary is assumed to be the backpressure valve) and $\dot{m}_{out,orifice}^{H_2}$ [kg/s] is the mass flow rate of hydrogen lost through the orifice.

The backpressure valve is modelled through its PID controller which directly regulates the pure hydrogen flow exiting the system $\dot{m}_{out,ELsystem}^{H_2}$ [kg/s] (i.e. neglecting the characteristic curve of the valve and its dynamics) in order to maintain the active adsorption bed pressure at the given setpoint (30 bar_g), while the hydrogen slipstream used for the regeneration of the regenerating bed is determined implementing a simplified model of an orifice, which computes the mass flow rate of the gas as:

$$\dot{m} = (KY)A_0\sqrt{2g\rho_1\Delta p} \tag{2.71}$$

referred to as "ASME" equation [10] where KY [$m^{1/2}/s$] is the discharge coefficient (computed as the product of the orifice discharge coefficient for incompressible flow K and the expansion factor Y, accounting for compressibility of the gas), A_0 [m] is the orifice area, g [m/s^2] is the gravity acceleration, ρ_1 [kg/m^3] is the density of hydrogen upstream the valve and Δp [Pa] is the pressure difference across the valve (the pressure downstream the orifice is assumed to be equal to the atmospheric one). The orifice is calibrated by assuming the terms $(KY) \cdot A_0 = c$ to be constant in the operating range of interest and determining it knowing the mass flow rate passing through the orifice at nominal conditions (Δp = 30 bar).

The dynamic of the PSA system, related to the gas accumulation in the active adsorption bed, is modelled by including in the hydrogen – water separator model the volume of the PSA bed itself. In other words, the hydrogen – water separator and the PSA are assumed to be a single volume in which the hydrogen – water vapor

accumulates, (section 2.4), the pressure of the total mass of vapor from the stack to the backpressure valve is computed as:

$$p = \frac{m_{vap} \cdot T_{vap}}{MM_{vap} \cdot V_{vap,H_2tank+PSA}} \tag{2.72}$$

where p_{vap}[Pa] is the pressure of the vapor in the hydrogen – water separator tank, assumed to be equal to the pressure inside the dryer bed and at the backpressure valve inlet (pressure losses are neglected, considering the low velocities), m_{vap} [kg] is the total mass of gas accumulated in the hydrogen – water separator and in the adsorption bed which molar mass MM_{vap}[g/mol] is computed as a weighted average of the molar mass of hydrogen and water, T_{vap} [K] is the temperature of the vapor inside the hydrogen – water separator and $V_{vap,H_2tank+PSA}$ [m^3] is the total volume occupied by the vapor estimated as:

$$V_{vap,H_2tank+PSA} = \left(V_{H_2tank} + V_{PSA}\right) \cdot 1.1 - V_{H_2tank}^{liq} \tag{2.73}$$

where V_{H_2tank} [m^3] is the total volume of the hydrogen – water separator tank, $V_{H_2tank}^{liq}$ [m^3] is the volume of liquid water contained in it, computed dynamically in the model block described in section 2.4 and V_{PSA} [m^3] is the net volume of one adsorption bed of the PSA. The presence of the 1.1 term has the purpose to take into account the volume of pipes and of the hydrogen chiller that otherwise would be neglected, estimated to account for a 10% of the sum of the volume of the PSA and of the hydrogen tank.

2.6 Deionized water tank

The deionized water tank collects the water to refill the oxygen – water separator, which must be demineralized water (conductivity below 1 $\mu S/cm$) with high purity. It receives the water from the hydrogen – water separator after the hydrogen removal in the flash drum (see section 2.4) and a water refill $\dot{m}_{refill}$ [kg/s] flow used to control the water level in the tank which is modelled by a relay. The water exiting the tank $\dot{m}_{toO_2Sep}$ [kg/s] is used to refill the oxygen – water separator, which then provides the feed in water for the stack (see section 2.3). The tank is modeled by solving dynamic mass and energy balances assuming a uniform temperature in the tank:

$$\dot{m}_{refill} + \dot{m}_{fromH_2Sep} - \dot{m}_{toO_2Sep} = \frac{dm_{tank}}{dt} \tag{2.74}$$

$$(\dot{m} \cdot h)_{refill} + (\dot{m} \cdot h)_{fromH_2Sep} - (\dot{m} \cdot h)_{fromO_2Sep} - \dot{Q}_{loss} = \frac{dQ_{tank}}{dt} \tag{2.75}$$

where $\dot{Q}_{loss}$ $[kW]$ are the convective heat losses to the environment, modeled as for the stack (see section 2.2), where Eqs. from (2.39) to (2.43) are used.

2.7 Feed water cooler

The feed water cooler has the purpose to achieve temperature control over the stack, by subtracting heat from the stack feed-in water and thus avoiding its overheating above the temperature setpoint. The cooler is modelled as a counter-current plate-type heat exchanger working with liquid streams on both sides. In particular, it works with water on the hot side and coolant fluid on the cold side. The heat exchanger is composed of parallel plates forming a modular structure and the fluids are assumed to be equally distributed among the channels between the plates. Therefore, it is modelled as a sequence of identical sub-units, including a single plate and half of the adjacent hot and cold channels. The heat transferred, the temperature of the plate and of the outlet streams are computed, discretizing the unit along the direction of the channels (1D-model). For each control volume, mass and energy balances are solved assuming a uniform temperature for the plate, neglecting heat transfer by conduction along the flow direction, fluid mass accumulation in the channels and heat losses to the environment. Temperature dynamic is related to the thermal capacity of the heat exchanger materials (C_{plate} $\left[\frac{kJ}{kg}\right]$):

$$\dot{Q}_{hot} - \dot{Q}_{cold} = \dot{m}_{plate} \cdot C_{plate} \cdot \frac{dT_{plate}}{dt} \tag{2.76}$$

The thermal capacity and the heat transfer coefficients are assumed to be constant, while the thermal resistance of the plate is neglected. Pressure is assumed to vary linearly with the mass flow rates (given the assumptions of laminar flow and incompressible fluids):

$$\Delta p = \Delta p_{nom} \frac{\dot{m}}{\dot{m}_{nom}} \tag{2.77}$$

where Δp_{nom} [Pa] and $\dot{m}_{nom}$ [kg/s] are known from the heat exchanger datasheet.

2.8 Pipes

The Simulink model computes the distributed pressure drops in the pipes connecting the process units as function of the volumetric flow rate:

$$\Delta p_{distributed} = \lambda \rho \frac{L}{D} \frac{v^2}{2} = \lambda \rho \frac{8\,L}{\pi^2 D^5} \dot{V}^2 \tag{2.78}$$

where the Darcy friction factor λ is assumed to be constant, while concentrated pressure drops (e.g. in pipes elbow joints) are taken into account by means of a corrective coefficient K_{conc} [-]:

$$\Delta p_{tot} = \Delta p_{distributed} * K_{conc} \tag{2.79}$$

Transport delay is also modelled, the time needed by the fluid to pass through a tube, in the assumption of incompressible fluid, is computed as:

$$t_{delay} = L\frac{\pi D^2}{4}\cdot\frac{1}{\dot{V}} \tag{2.80}$$

Accumulation phenomena are neglected in pipes, given the small volume contained in the pipes with respect to other process units.

2.9 Pumps

In the plant, two pumps are present. The first one is the stack feed-in water pump, or circulation pump, which is a centrifugal pump, while the second one is the pump used to refill the oxygen – water separator (section 2.3) with fresh water coming from the deionized water tank (section 2.6), which is a positive displacement pump. The circulation pump is always active during the electrolyzer operation and works at constant rotational speed while the second pump can be 'on' or 'off' depending whether the refill is active or not. The pumps are modelled by means of a stationary model, since the pump dynamics are assumed to be negligible as a first approximation. The model computes the electric consumption of the pump P_{el} [W], the pressure p_{out} [Pa] and the temperature T_{out} [K] of the outlet fluid as:

$$P_{el} = \frac{\frac{\dot{m}}{\rho_{fluid}}\Delta p}{\eta_{is}\cdot\eta_{mech}\cdot\eta_{el}} \tag{2.81}$$

$$p_{out} = p_{in} + \Delta p \tag{2.82}$$

$$T_{out} = T_{in} + \frac{P_{el}\cdot\eta_{mech}\cdot\eta_{el}}{c_{p,fluid}\cdot m_{fluid}} \tag{2.83}$$

where $\dot{m}$ [kg/s] is the fluid flow rate, Δp [Pa] is the pressure gain the pump has to provide, ρ_{fluid} [kg/m^3] is the density of the fluid, assumed to be constant as well as the isentropic η_{is} [-], mechanical η_{mech} [-] and electrical η_{el} [-] efficiencies.
The pump located in the coolant fluid circuit of the heat exchangers is considered to be outside of the system boundaries as the analysis that will be carried out in the next chapters has the purpose of optimizing the electrolyzer and its BoP components and there is no interest in optimizing the cooling system.

2.10 Rectifier

In order to feed the stack with DC current, the AC current supplied to the system must be rectified. This process leads to electrical losses, quantified by the rectifier efficiency $\eta_{rectifier}$ [-]. Before being rectified, a portion of the net electrical power supplied to the electrolyzer system P_{net} [kW] is consumed by auxiliaries P_{aux} [kW], i.e. the two pumps, a fun and other small electrical components in the system. The last two are modelled as a constant power consumption, while the pumps consumption is computed as already exposed in section 2.9. The model solves dynamically the electrical power balance of the stack in order to determine the value of the electrical current supplied to the stack:

$$I = \frac{V_{stack}}{(P_{net} - P_{aux}) \cdot \eta_{rectifier}} \tag{2.84}$$

As already shown in section 2.2, the stack model block receives in input the current and gives as output the voltage V_{stack} [V], which is looped back in the rectifier block, guaranteeing the continuous power balance of the stack.

3

CHAPTER 3 – MODEL VALIDATION

This chapter deals with the validation of the system model described in the previous chapter. In detail, in section 3.1 the experimental campaign and the data collected in it are described and briefly commented. The validation process takes place in sections 3.2.1 (statically) and 3.2.2 (dynamically) for polarization curves, in sections 3.2.3 and 3.2.4 for thermal behavior and in section 3.3 for pressure dynamics. Finally, in section 3.4 the performances resulting from the simulation of the complete system model, including BoP components, are compared with full load and part-load experimental performances.

3.1 Experimental Campaign

For model validation, datasets from the running of the electrolyzer system during the University of California Irvine (UCI) power-to-gas demonstration project, involving its integration with the UCI Central plant (Figure 3.1), [5] are used,.

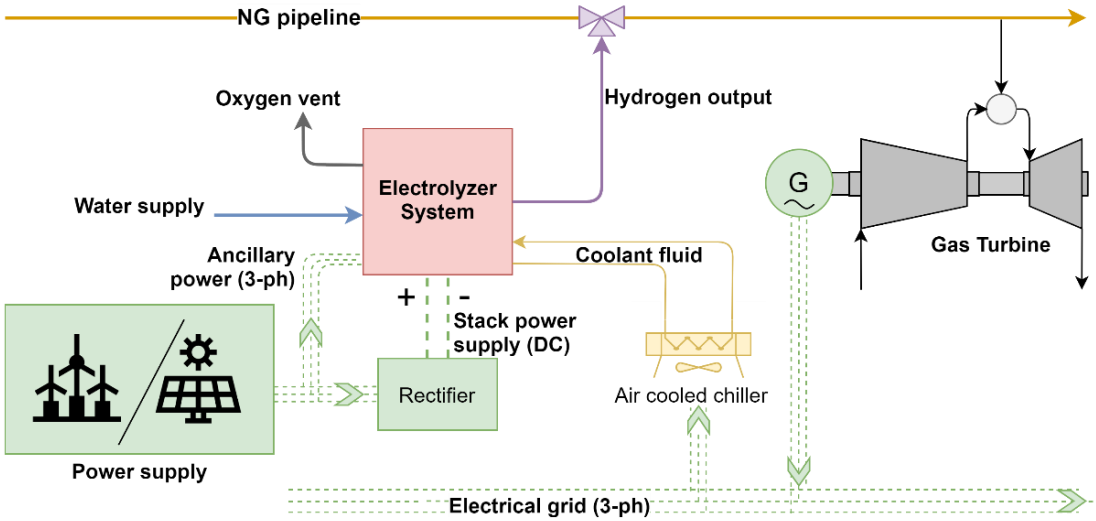

Figure 3.1 - Simplified scheme of the UCI power-to-gas demonstration plant

The electrolyzer deployed is a Proton Onsite Model C10 (whose datasheet is reported in Table 3.1), a differential pressure PEM electrolyzer, with a 65 cells and a 214 cm^2 active area stack, 62 kW of nominal power and 410 A of stack nominal current.

Table 3.1 - Operating parameters for the Model C10 electrolyzer system [5]

Hydrogen	
Net production rate [Nm^3/h @ 0°C, 1 bar]	10 Nm^3/h
Net production rate [kg/24 h]	21.6 kg/24 h
Delivery pressure – Nominal	30 bar_g
Power consumption per volume of gas produced	6.2 kWh/Nm^3_{H2}
Power consumption per mass of gas produced	68.9 kWh/kg_{H2}
Water	
DI water requirement	9 l/h
Circulation rate (at anode)	37.9 l/min
Temperature	5 °C to 40 °C
Input water quality (conductivity)	>1 MΩ ·cm
Electrical specifications	
Breaker rating	480 VAC 3-phase, 100 kVA
System power (kW AC)	60
Electrolysis stack (Volts/Amps DC)	140/410
Cooling	
Chiller system	Accuchiller air-cooled chiller
Chiller capacity (kW_{th})	55.7
Max heat refrigeration (kW_{th})	33.4

During the experimental campaign, the hydrogen is produced by the electrolyzer system at 30 bar_g and then mixed into the high pressure natural gas pipeline upstream of a gas turbine in order to be combusted into the gas turbine, thus constituting a complete P2G2P system. The power supplied to the system is partly used as ancillary power to feed the BoP components, such as pumps and fans (working with AC current), and partly sent to the rectifier in order to supply the electrolyzer stack with DC current. The air-cooled chiller is external to the electrolysis system as it is electrically fed by the electrical grid and its consumption is not measured during experiments. Hence, the validation process will involve the electrolyzer system with all its BoP components, with the exception of the air cooled chiller.

The main research objectives of the experimental campaign included evaluating the dynamic dispatch capabilities of a commercial PEM electrolyzer system in load following both solar PV (section 3.1.2) and wind farm aggregated power (section 3.1.3), and characterizing the PEM electrolyzer performance. Furthermore, cold startups have been performed at different loads, controlling the electrolyzer hydrogen output through the installation of an external mass flow controller (section 3.1.1).
Measures of interest include the hydrogen pressure at the outlet of the hydrogen electrode, oxygen pressure at the oxygen – water phase separator, stack current, stack voltage, water temperature at the anode outlet, which are collected at 1 s intervals and

averaged down to 15 seconds intervals. As shown in Figure 3.2 cathode side pressure (hydrogen pressure) is measured in the hydrogen tank, anode side pressure in the oxygen tank, while stack temperature is the temperature measurement taken in the recirculating water exiting the anode.

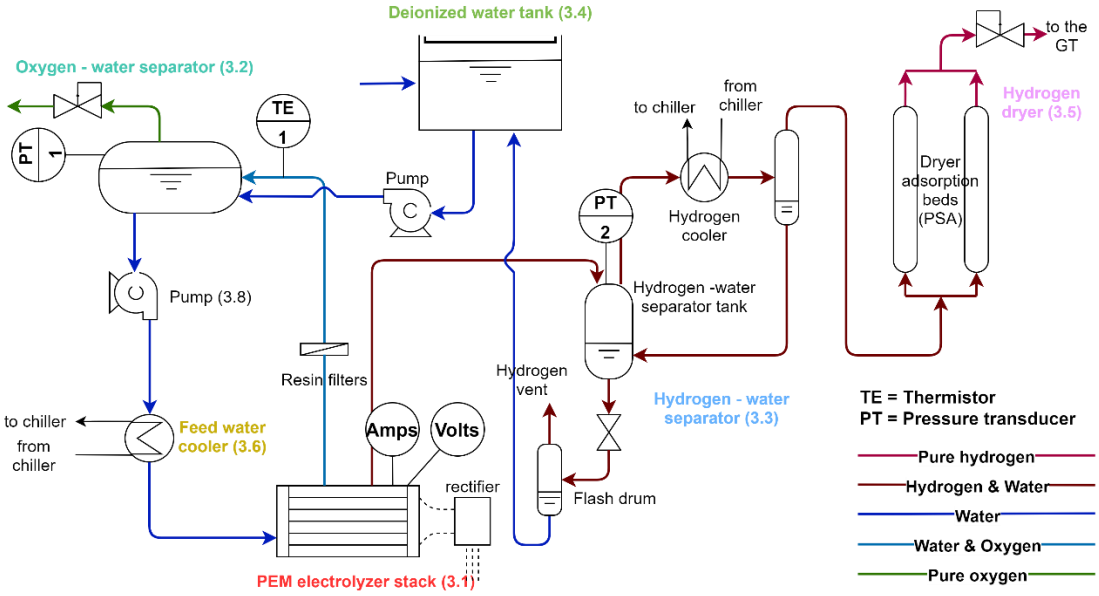

Figure 3.2 – Basic PFD of the complete electrolyzer system with the representation of the sensors used during the experimental campaign

3.1.1 System start-up

The system has been run for a total of 37 hours, during which it has been switched off until cooling and switched on again for 6 times. In each of the warm-up transient the temperature ramps up to the nominal value set by the user while the system is controlled in hydrogen production, which is set to different values during operation. The flow rate of water fed to the stack is constant during system operation and equal to 37.85 l/minute. The data of current, voltage, stack temperature, anode side and cathode side pressures have been collected at 1 s intervals and averaged down to 15 s intervals. The current density is computed by knowing the cell area, which is reported to be 213.68 cm^2 ($i\ [\frac{A}{cm^2}] = \frac{I\ [A]}{A_{cell}[cm^2]}$), while the cell voltage is computed by knowing the number of cells which compose the stack, reported to be equal to 65 ($V_{cell} = \frac{V_{stack}}{N_{cells}}$, as electrical connections are in series in the stack).

The temperature and current density values over time are shown in Figure 3.3, where the data are represented in a centered moving mean on 3’ 45” intervals, for reasons of clarity in reading the graph. From Figure 3.3 it is possible to notice that the system is able to keep the stack temperature almost constant after warm-up despite the continuous variations in the current due to the hydrogen production-based control of

the system. It is also possible to make an assumption on the ambient temperature during experiments, which must be below 25 °C, which is the minimum temperature that the stack reaches, and is assumed to be equal to 22 °C.

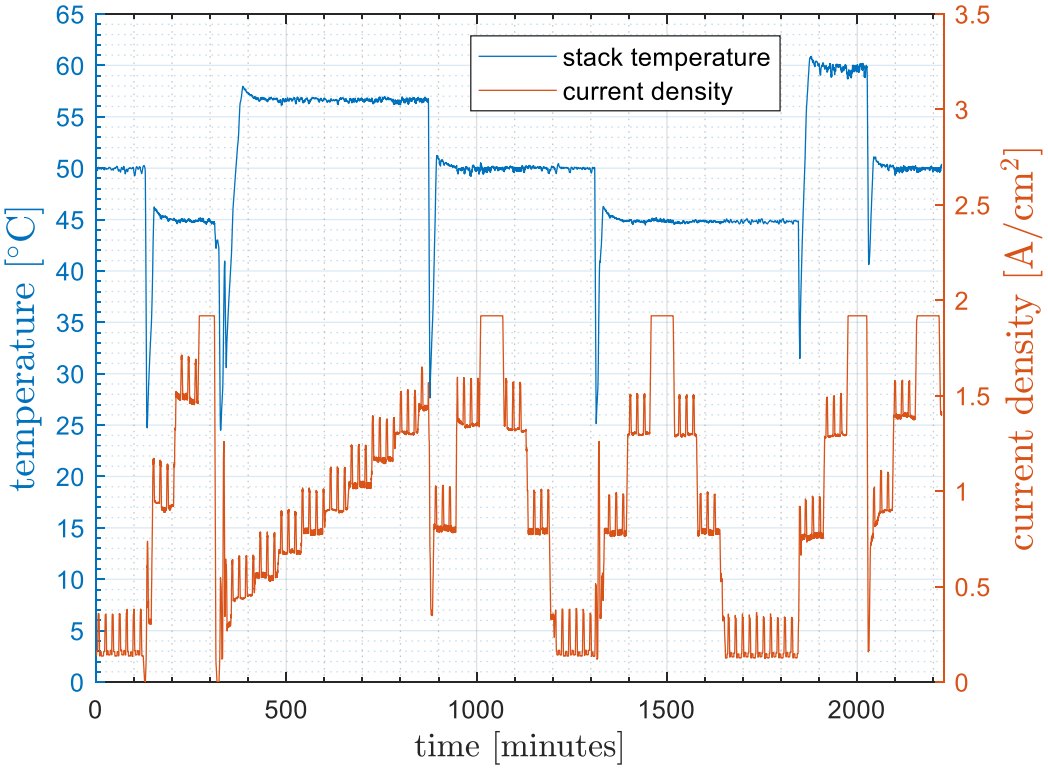

Figure 3.3 – Stack temperature and current density during warm-up experiments (averaged data with moving mean)

During experiments it was not possible to control the anode side pressure and the range for the cathode side pressure was very limited (mainly 28 – 32 barg). As it is possible to see in Figure 3.4, showing cathode pressure, anode pressure and current density during warm-up experiments, anode side pressure is almost constant and ranges between 1.01 bar_g and 2.72 bar_g and increases slightly for higher currents, due to the higher oxygen production, while maximum cathode pressure decreases with higher currents due to system pressure controls interacting with the injection to gas turbine process. The maximum cathode pressure reaches 33.24 bar_g. It is also possible to notice some pressure dips on the cathode side after system shut down during the restart, indicating that in that moment the hydrogen flow is deviated to the vent (atmospheric pressure is, in fact, reached in the hydrogen tank). For example, in the 4th start-up of the dataset, shown in Figure 3.5, between minute 1320 and minute 1321, the control system, that immediately after the venting of hydrogen measures a zero-output for the hydrogen flow rate, tries to increase the hydrogen output by increasing the current. After the venting ends, the pressure, which is regulated by a backpressure valve increases up to the nominal value, when the hydrogen delivery to the gas turbine starts (from minute 1322).

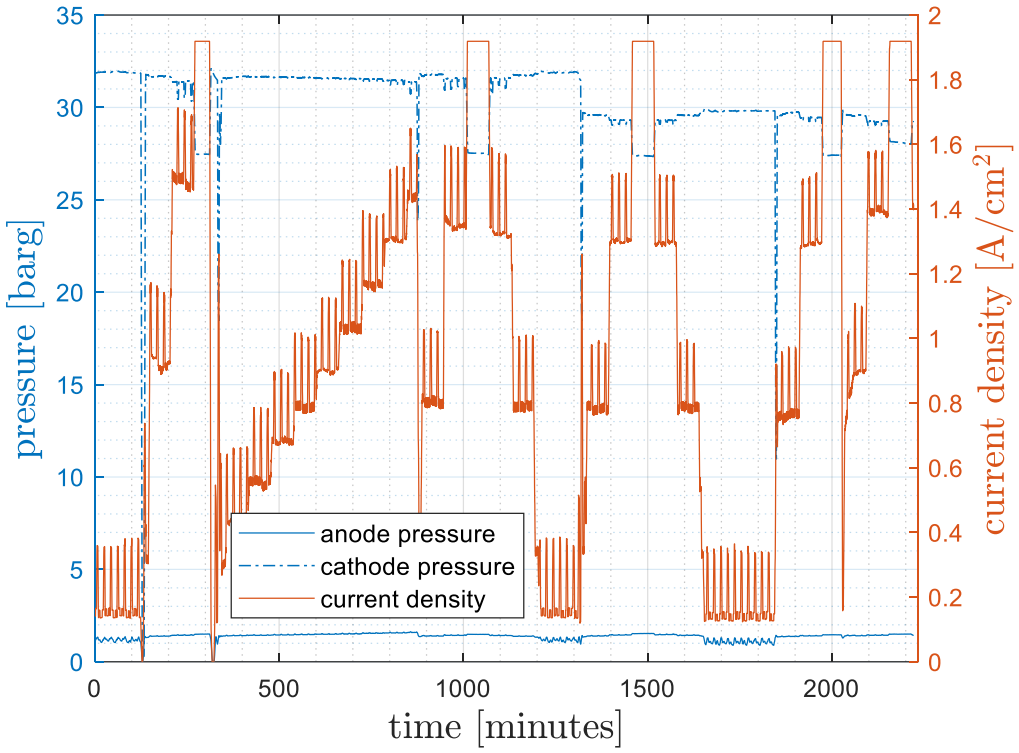

Figure 3.4 – Cathode pressure, anode pressure and current density during warm-up experiments (averaged values with moving mean)

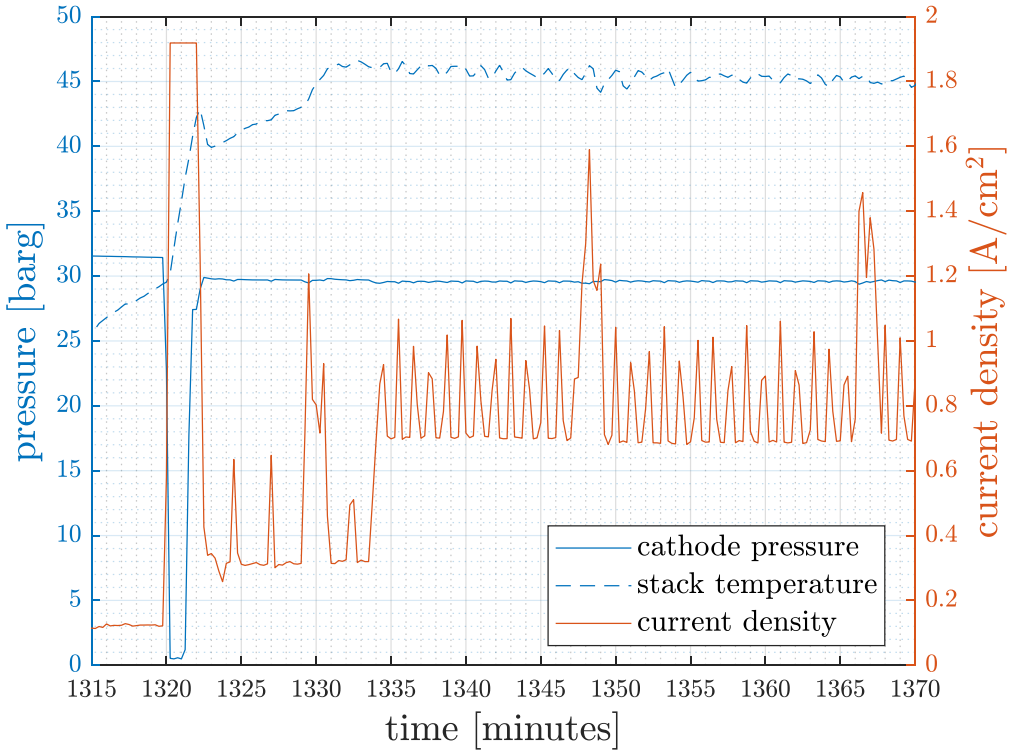

Figure 3.5 - Hydrogen pressure, stack current density and temperature around the 4th start-up

It is also possible to notice smaller and higher peaks of the current. The small peaks are due to the control system, and are closer for higher currents, while the high peaks, occurring every 18 minutes, are due to the switching of the operating PSA bed, in order to regenerate the other bed. When this operation occurs, the hydrogen delivery stops for few seconds, so current is increased by the control system, trying to keep the hydrogen output to the set one. Eventually, it is worth noting how the temperature increase rate (the derivative of the temperature over time) is proportional to the value of the current density, determining a faster warm-up when current is higher.
A zoom on each of the 6 (all available) temperature transient identified is shown in Figure 3.6, where current density and temperature evolution over time are shown, deliberately eliminating from the time window the first phases when the temperature acts in irregular ways, probably due to not known phenomena influencing the energy balances (see around minute 1322 in Figure 3.5, probably when the temperature increase is very fast the chiller starts to extract heat from the stack feed-in-water even though the temperature setpoint is not reached yet).

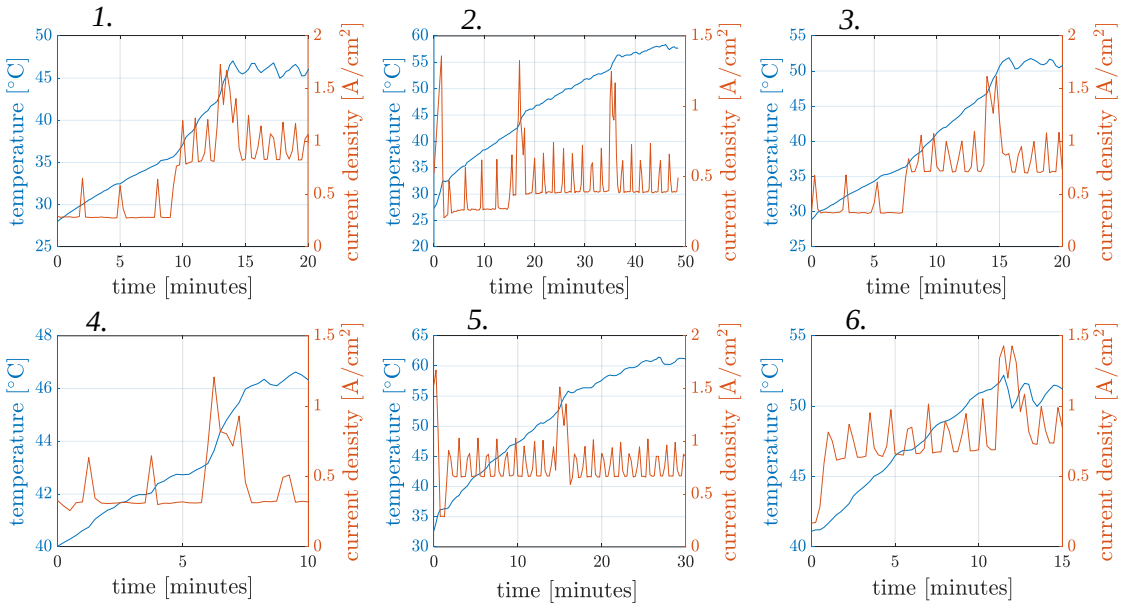

Figure 3.6 - stack current density and temperature evolution for each of the 6 warm-ups identified in the dataset

Despite the intervals are selected in order to avoid too irregular traits, there are, however, some irregularities in temperature trends, like a sudden decrease in the temperature curve slope after the 5th minute in the transient *4.* and the decrease in the temperature slope in transients *2.* and *5.* despite the constant current. These phenomena are probably due to some events that influence energy balances (like a premature start of feed-in water cooling) or high heat losses to the environment. The main characteristics of each temperature transient are shown in Table 3.2, where it is possible to notice how generally (transients from *1.* to *4.*) to a higher mean current density corresponds a higher mean slope of the temperature over time ($(dT/dt)_m$), but

in transients *5.* and *6.* where, despite a high mean current density, temperature increase rate relatively low.

Table 3.2 – Duration, temperature range, mean temperature increase over time and mean current density for each temperature transient identified in the dataset

	Duration	**Temperature**			**Current**
# transient	[min:sec]	Initial [°C]	Final (setpoint) [°C]	$(dT/dt)_m$ [°C/s]	Mean current [A/cm^2]
1	13:30	32	45	0.0160	0.557
2	44:15	27	58	0.0117	0.448
3	15:00	29	50	0.0233	0.649
4	08:15	40	46	0.0121	0.449
5	26:30	34	61	0.0170	0.799
6	10:45	41	51	0.0155	0.787

3.1.2 Coupling with solar photovoltaic

The electrolyzer system has been operated as coupled to a solar photovoltaic generation profile with a peak power ratio of 1:1. The system is operated with a stack temperature constant and equal to 55 °C, a cathode pressure of 30 bar_g and an anode pressure of 1.7 bar_g for approximately 90 hours. Also in this case, the dataset provided is composed of data recorded with a 1 second intervals and averaged down to 15 seconds intervals. The measured values of stack current, stack voltage, stack temperature, cathode pressure and anode pressure are provided. As it's possible to notice from Figure 3.7, where the stack temperature and stack power deriving from the coupling with the photovoltaic plant during autumn is represented, the stack power never gets any lower than 3 kW of power. In fact, the system hasn't actually been coupled to a solar photovoltaic panel, but a solar photovoltaic generation profile was replicated using electrical power from the grid. Thus, in order to reduce the observation time, the night time hasn't been reproduced. It is possible to notice that the electrolyzer is able to keep the temperature around the rated value of 55 °C quite well (maximum error ± 2 °C) despite the quick changes in the load. Similar results from experiments reproducing the solar PV-electrolyzer coupling during winter are also provided. In Figure 3.8 stack current and the pressures at cathode and anode are illustrated.

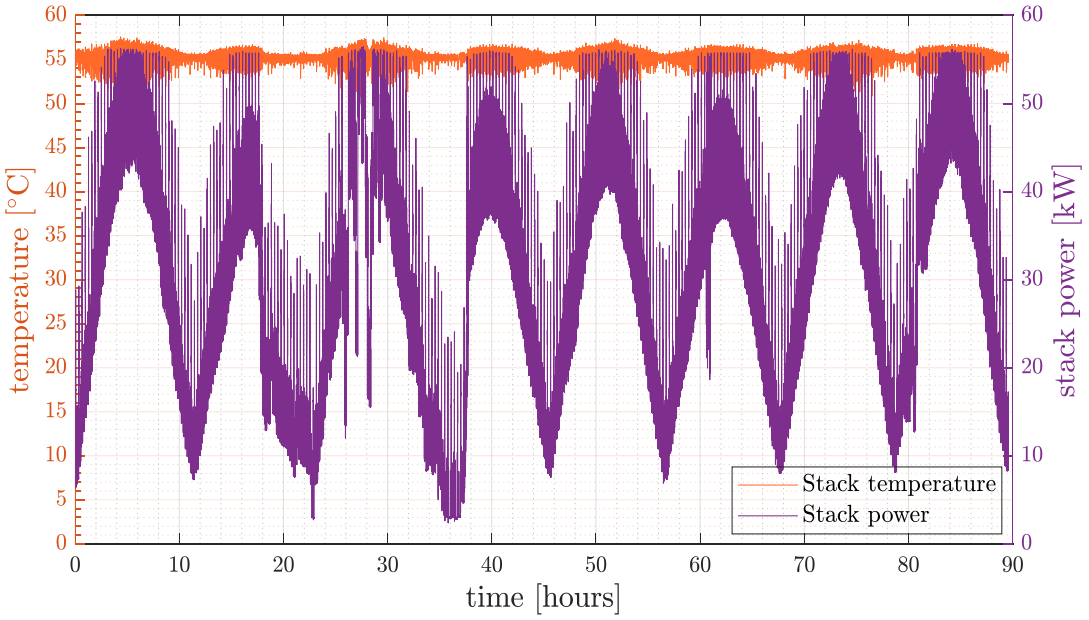

Figure 3.7 - Stack power and temperature of the electrolyzer over time measured during the experimental campaign coupling the system with solar photovoltaic

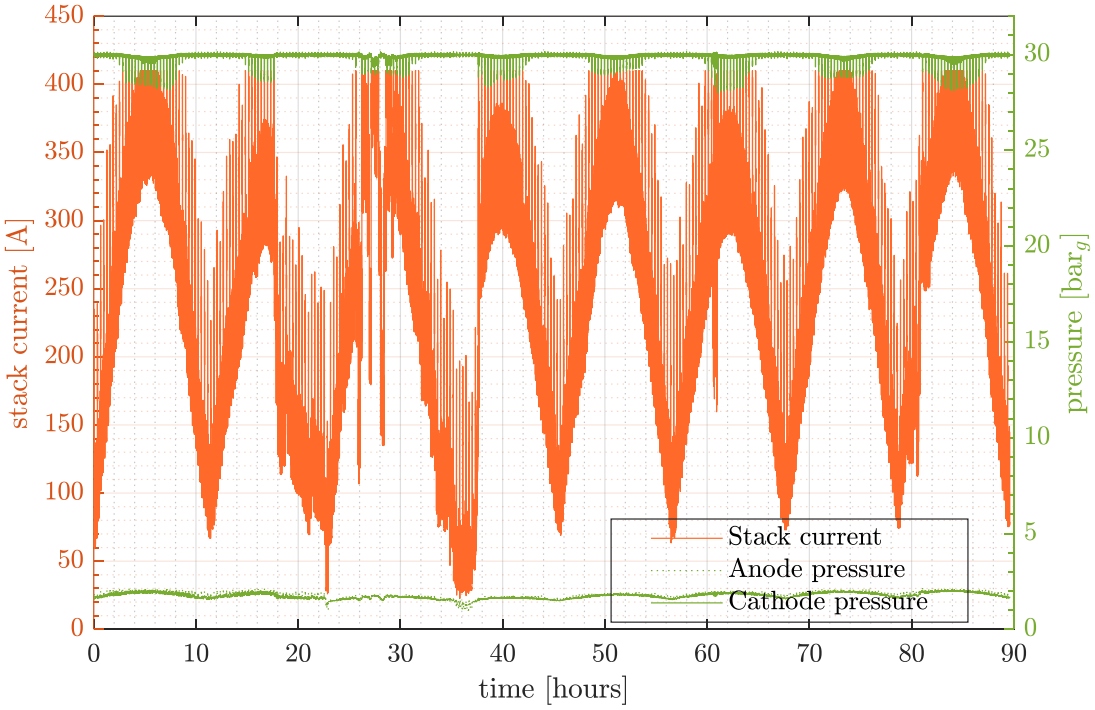

Figure 3.8 - Stack current, anode and cathode pressures over time from coupling to solar photovoltaic (autumn)

3.1.3 Coupling with wind turbine

The electrolyzer has also been operated as coupled to a wind turbine-type load profile. Also in this case the coupling has been only simulated, thus the periods during which the power from the wind turbine is zero, or not sufficient to run the whole electrolyzer, haven't been reproduced during experiments. Hence, the system is run continuously for 330 hours. As in previous cases, the stack temperature, voltage and current, and cathode and anode pressures are measured at 1 second intervals and provided as 15 seconds averages. As before, the system is able to keep the stack temperature around 55 °C as shown in Figure 3.9, representing the stack power and temperature over time.

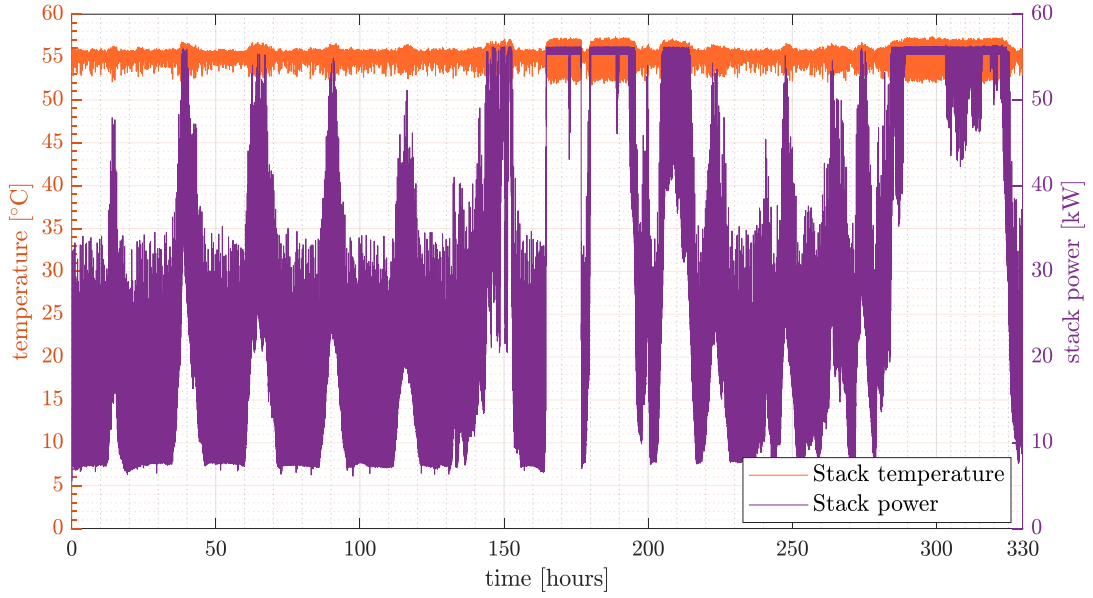

Figure 3.9 - Stack temperature and power over time from the coupling with the wind turbine

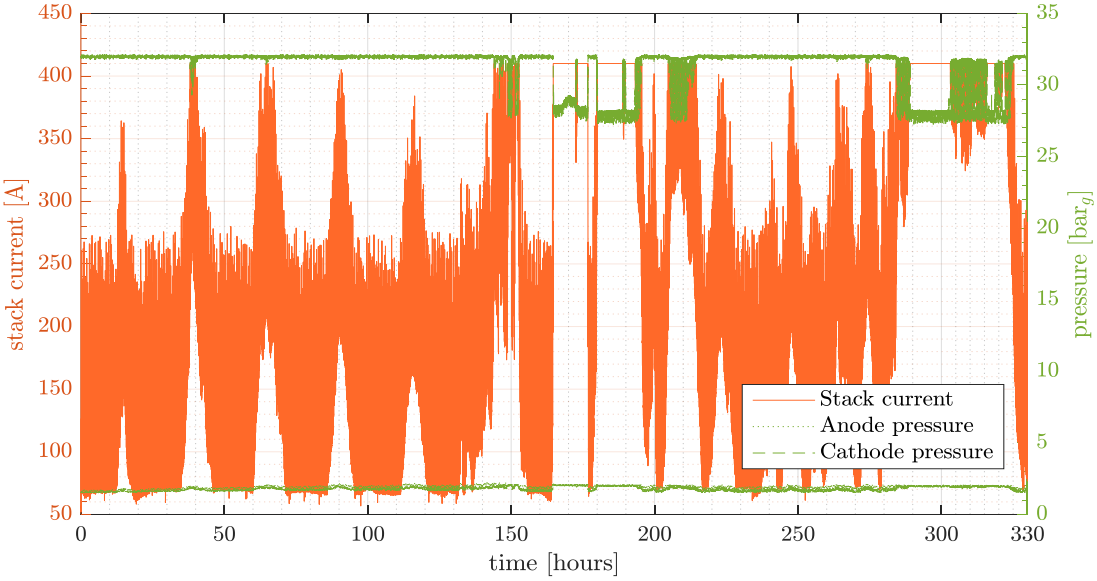

Figure 3.10 – Stack current and cathode and anode pressures over time deriving from the coupling with the wind turbine

The anode pressure is quite constant all over the operation time at 1.7 bar_g, while the cathode pressure is kept at 32 bar_g, with some drops at very high power, due to the interaction with the gas turbine downstream (Figure 3.10).

3.2 Stack model validation

The first part of the stack model validation involves the electrochemical behavior, i.e. the polarization curves. The second part regards the thermal transients of the stack. For the electrochemical behavior validation only the stack block of the Simulink model is considered, while for the thermal behavior of the stack it is required the simulation of the whole system, since all the system components influence the mass and thermal transfers of the stack. After the validation of the stack polarization curves, for which the first dataset in section 3.1.1 (Figure 3.3) is used, the stack operation is simulated imposing to the stack the PV current profile in order to verify that the electrochemical response of the stack is well simulated also in dynamic and realistic conditions.

3.2.1 Polarization curves

For polarization curves validation the dataset containing the different transients (section 3.1.1, Figure 3.3) are clustered in 7 different temperature ranges in order to compare the model polarization curves at different temperatures and verify that it correctly derives voltage from current at any temperature of interest.

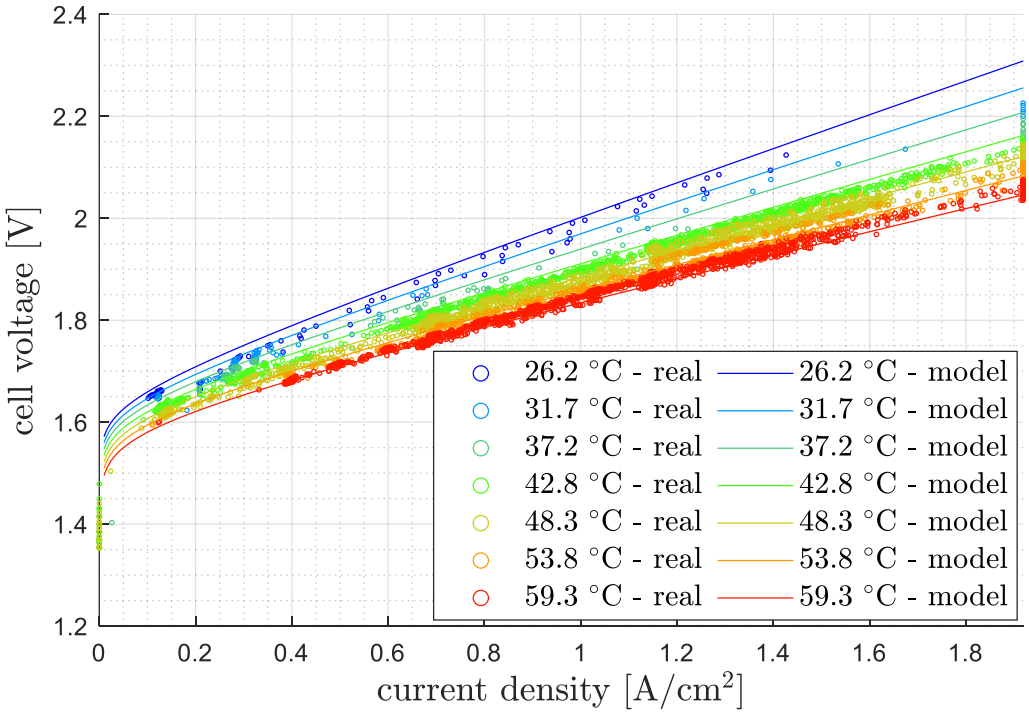

Figure 3.11 - Model polarization curves and experimental i-V couples at different temperatures

The value of the temperature ranges from 23.5 °C to 62 °C so the data are gathered in different clusters, corresponding to 5.5 °C wide temperature ranges centered on a certain value, depending on the stack temperature during the measure. For each of the 7 clusters, the mean cathode pressure and anode pressure of the experimental data are determined and imposed in input to the model in order to reduce the error due to the dependence of the voltage on the pressures. The model polarization curves are drawn by varying the current density from 0 A/cm^2 to 2 A/cm^2 and imposing the mean temperature and pressures of each cluster as a constant value (see Figure 3.11).
It is possible to notice the presence of a positive error (over-estimation of the voltage) at low temperature gradually decreasing up to negative values with the increase in temperature (Table 3.3).

Table 3.3 - Mean and maximum error on the voltage in the polarization curves for different temperatures

	Temperature dependence			
	Error analysis			
Temperature range [°C]	**Mean error [V]**	**Max error [V]**	**Mean error [%]**	**Max error [%]**
26.2 ± 2.7	0.0212	0.0486	1.20 %	2.92 %
31.7 ± 2.7	0.0192	0.0628	1.07 %	3.87 %
37.2 ± 2.7	0.0181	0.0741	1.03 %	3.90 %
42.8 ± 2.7	0.0116	0.0361	0.61 %	1.83 %
48.3 ± 2.7	0.0071	0.0442	0.40 %	2.94 %
53.8 ± 2.7	0.0033	0.0256	0.20 %	1.37 %
59.3 ± 2.7	-0.0079	-0.0300	-0.42 %	-1.45 %

This errors never exceed 3.9%, if we exclude a single outlier (12.44%, 0.175 V) in the third temperature range, and have an average on the whole current density range of 1.2% in the worst case. Taking into account that the temperature at which the model computes the voltage is not the same at which the real voltage is measured, the error inherent the measuring instruments, the influence of pressures (not taken into account in this analysis) and in general the quality of the data provided (15 seconds averages), these errors are considered completely acceptable.
In order to obtain these results, the original polarization curve model presented in section 2.2 is improved by introducing the dependence of the exchange current density on the temperature (Eq. (2.1)).

Indeed, if the activation overpotential (ΔV_{act}) is computed considering a constant exchange current density, as initially assumed, the voltage dependence on the temperature results to be strongly affected, as shown in *Figure 3.12*.

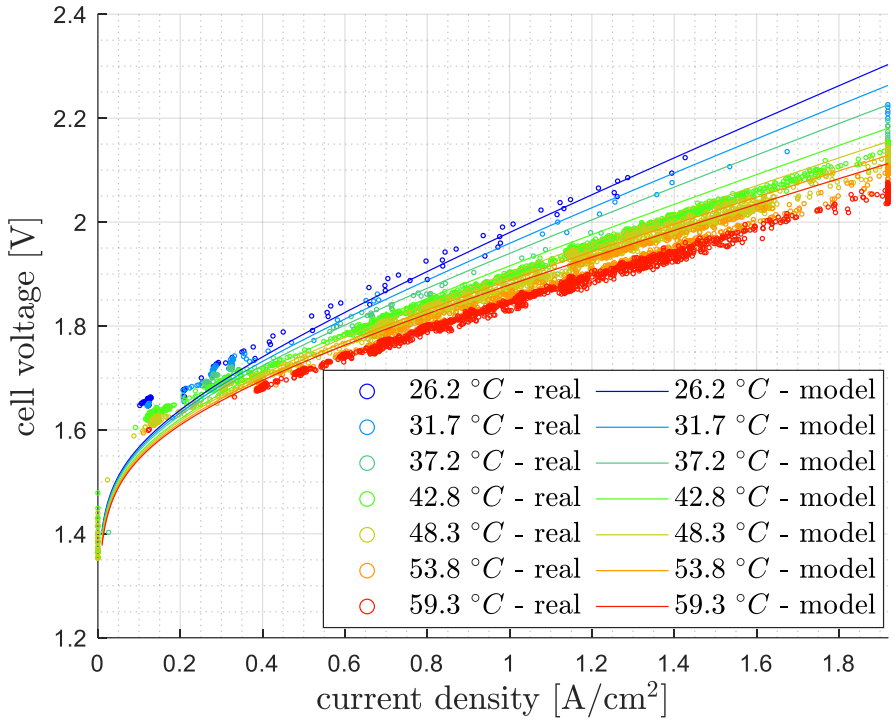

Figure 3.12 - Polarization curves and experimental i-V couples at different temperatures in the preliminary model before introducing exchange current density's dependence on temperature.

As expected, for any current value the voltage variation with the temperature is smaller than it should. In fact, exchange current density represents the electrode's readiness to proceed with the electrochemical reaction, it is thus an important parameter for evaluating the activation overpotential [7]. Exchange current density can be expressed as [8]:

$$i_{0X} = i_{Xref} \cdot exp\left(-\frac{Vact,X}{R \cdot T}\right) \tag{3.1}$$

where i_{Xref} is the pre-exponential factor and $V_{act,X}$ is the activation energy for anode and cathode. Neglecting the influence of the temperature and assuming a constant exchange current density determines an error in the voltage dependence on the temperature. From Figure 3.11 it is possible to notice how the introduction of the exchange current density's dependence on the temperature influences the polarization curves when varying the temperature, with respect to the case in Figure 3.12, where it is fixed.

The analysis of the polarization curves at different pressures requires the i-V couples taken into account to be measured at similar temperatures. In fact, the voltage variation generated by the temperature range in object (23.5 °C – 62 °C) are significantly wider than the one generated by the pressure range of the available data (28.5 bar – 33.5 bar). By considering only the data available in a narrow temperature range of 50 ± 1 °C and clustering them in two pressure ranges of 29.56 ± 1.22 bar_g and 32.00 ± 1.22 bar_g it is not possible to appreciate a sensible change in the voltage, where both the experimental data and the model curves appear almost superposed (Figure 3.13). It is therfore not possible, with the available dataset, to validate the voltage variation with pressure of the model. Thus, the model can't be considered predictive on the operation at different pressures. The validation of the model with regard to the behaviour of the electrolysis system at different pressures is a topic on which the future research works and experimental campaigns following this work should focus.

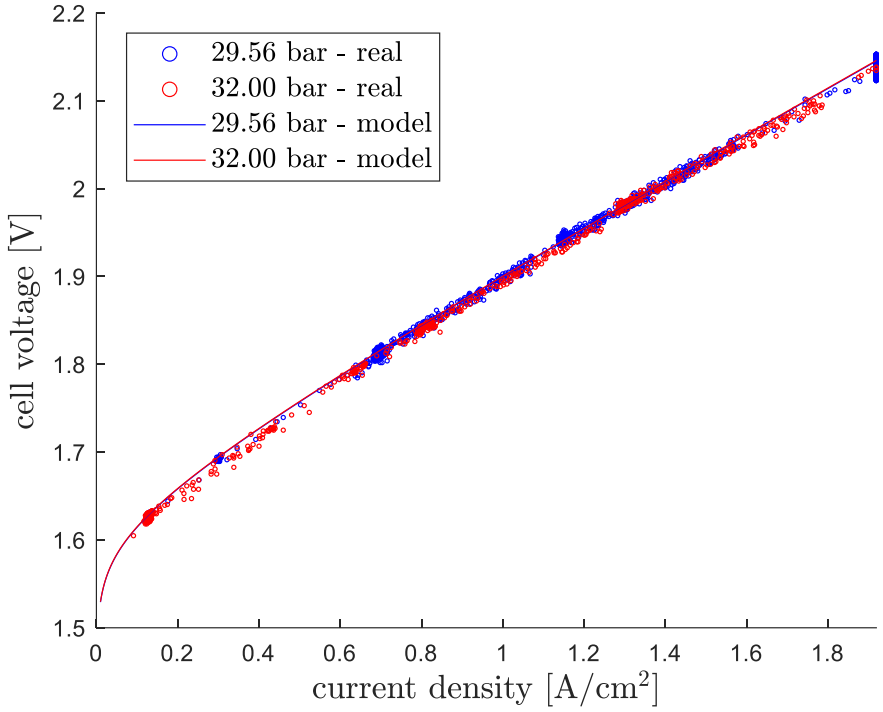

Figure 3.13 – Experimental and model i-V couples at different pressures and fixed temperature (50 ± 1 °C)

It is however possible to compare the polarization curves obtained from the model working at different pressures with results taken from the literature, in order to verify that the model has a realistic behavior. By simulating the stack operation at 7 bar and 70 bar on the cathode side (at 58 °C and 42 °C) it is possible to compare the polarization curves experimentally obtained from another PEM electrolysis system [12] operating in the same conditions (Figure 3.14). Anode pressure is kept close to atmospheric pressure in both cases.

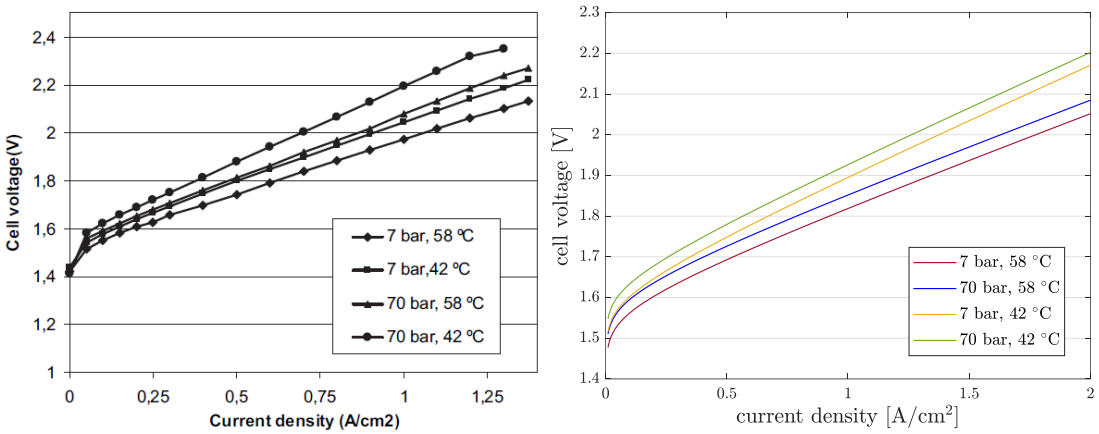

Figure 3.14 - Electrolyzer polarization curves in different operating conditions experimentally obtained from a different PEM electrolyzer ([12], left plot) and obtained from the model (right plot)

As the system with which the comparison is made is a different PEM electrolyzer, the quantitative results are different and cannot be validated. Anyway, it is possible to make some observation and to notice that qualitatively the model has a realistic behavior. In particular, voltage results to be higher when the stack operates at higher pressure of hydrogen, keeping the temperature constant. The main reason for these results is that a higher operating pressure directly leads to an increase in the open circuit voltage (Eq. (2.5)), shifting the curve upwards. This shift leads to two couples of parallel curves (one for each temperature) in the model results, which seem to well approximate the experimental behavior. However, in the model ohmic overvoltage is not affected by the pressure and the voltage increase is the same at any current density, while in the experimental results the voltage increase at higher pressure seems slightly higher at higher current density. Additionally, the pressure influence on the voltage seems to be lower at higher temperature in the experimental results, while according to Eq. (2.5) the pressure influence results to be slightly higher at higher temperature in the model. This observation points out that open circuit voltage is not the only parameter influenced by the operating pressure.
In fact, other secondary phenomena influence the polarization curves in a PEM electrolyzer. Increasing the cathode pressure leads at increasing the species partial pressure, preventing water diffusion inside the electrode and membrane Eq. (2.34), which consequently increases diffusion loss [58]. This loss is not considered in the model, but it also does not seem to significantly affect the voltage in the experimental case, due to the maximum current density being well below the limiting current density. In any case, a more detailed model for the computation of the concentration losses, taking into account the concentration of the chemical species at anode and cathode, as the one used in [45], could be considered for future analysis, with a view on the increase in the maximum current density forecasted for PEM electrolyzers. Such model uses the Nernst potential and computes the voltage loss due to concentration difference of charge-carriers between the electrolyte and the electrode surface from a reference concentration:

$$V_{conc} = \frac{RT}{4F} \ln \frac{C_{an,mem,o_2}}{C_{an/mem,o_2,0}} + \frac{RT}{2F} \ln \frac{C_{cat,mem,H_2}}{C_{cat/mem,H_2,0}} \quad (3.2)$$

Moreover, increasing the hydrogen pressure leads to hydrogen crossover across the membrane, reducing the Faradaic efficiency. This loss is not modelled as a voltage increase in the present model, but as a current reduction, and Faradaic efficiency dependence on the pressure is not considered.
Marangio et al. [53] also reported that increasing the operating pressure could lead to a voltage increase since it might reduce the movement of hydrogen ions across the membrane and make the reaction more difficult.
It is interesting to observe that, as the vertical shift of the polarization curve is a good approximation of the voltage variation with the pressure, an almost constant voltage drop is present along all the polarization curve (i.e. at any current density). This means that the cell efficiency drop when increasing the operating pressure of the electrolyzer is lower the higher is the operating current density.

3.2.2 Stack dynamic operation

In order to verify the accuracy of the electrochemical model in dynamic conditions (continuous and quick variations of current, pressure and stack temperature) the stack operation is simulated by the sole use of the stack Simulink model block imposing the real stack current, pressures and temperature profiles over time measured during the coupling with the solar photovoltaic (section 3.1.2, Figure 3.8).

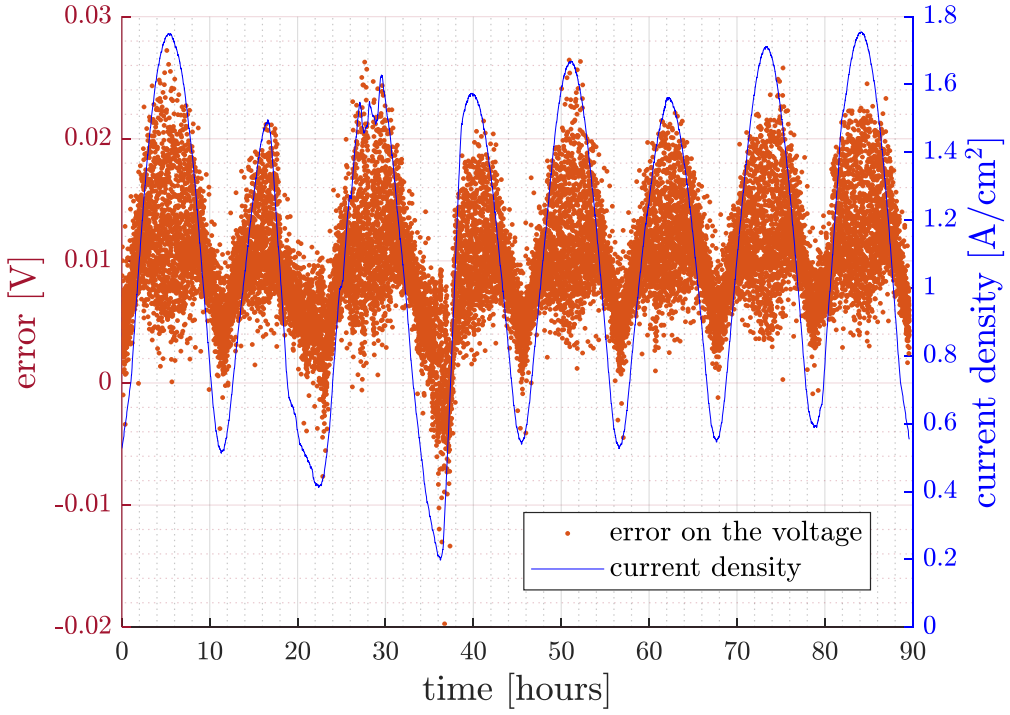

Figure 3.15 - Absolute error on the voltage and moving mean of the current density over time during simulation of coupling with solar PV

The results on the simulation show an error below 0.03 V (Figure 3.15) during all the 90 hours simulated, and a maximum relative error of 1.3%, results which are perfectly in line with the static ones (section 3.2.1, Table 3.3) in the range of temperature of 53.8 ± 2.7 °C. From Figure 3.15, where the moving mean of the current is plotted together with the error on the voltage, it is also possible to observe that the error on the voltage is not casual, but it is the higher the higher is the current density, and that the minimum error on the voltage is obtained at a current density between 0.6 and 0.8 A/cm^2.
It is however possible to state that the electrochemical model is able to reproduce the electrochemical behavior of the stack promptly and with a sufficient level of accuracy.

3.2.3 Stack thermal capacity

As already introduced in section 1.4.1, stack temperature tends to increase due to the irreversibility that occur within the electrochemical cells. In order to avoid the temperature to exceed a certain limit value (typically set around 60 – 70 °C for PEM electrolyzers) the control system is able to regulate the stack feed-in water temperature by means of a heat exchanger.
The analysis of the stack temperature transients during warm-ups allows to determine the heat capacity of the stack, since when the temperature setpoint is not reached, the heat exchanger heat duty is equal to 0.
The thermal capacity is the tendency of a material to change its internal energy and change its temperature when it is heated or cooled [59]. It is defined by:

$$C = \frac{Q}{(T_2 - T_1)} \tag{3.3}$$

Where C is the thermal capacity [J/K], Q [J] is the heat absorbed or released by the material, $T_2 - T_1$ [K] is the temperature difference before and after heating or cooling (i.e. absorbing or rejecting Q). In the case of the stack, the only unknown parameter in the energy balances is the stack thermal capacity (see section 2.2), so imposing to the stack model the experimental current density profile over time (correctly setting cathode and anode pressures) it is possible to compare the temperature evolution predicted by the model with the real one for different values of the stack thermal capacity. Since, as already said, the model of the entire system is used for the simulations, the assumptions in Table 3.4 are used to simulate the behavior of the other system components.
Results are shown in Figure 3.16, referring to the first temperature transient shown in Figure 3.6, from 28°C to 46°C, with a current setpoint equal to 0.24 A/cm^2 for the first 9 minutes, to 0.8 A/cm^2 from minute 9 to 12 and higher than 1.2 A/cm^2 from minute 12 to 14.
An increase in the stack thermal capacity of 40 kJ/K generates a delay of about 1 minute in the range of interest (this value is anyway dependent on the specific current profile). It is possible to notice in Figure 3.16 that the slope of the temperature profile over time ($\partial T/\partial t$) increases as the current density increases, due to the higher heat generated by irreversibilities (Q_{irr}) for higher current densities. The slope is also function of the thermal capacity, since increasing the thermal capacity and keeping the

same current (thus, same Q_{irr}) the temperature increase becomes slower (i.e. lower slope).

Table 3.4 – Setting of the main parameters that influence the thermal behavior of the system

Parameter	**Nominal value**
Initial stack temperature	Initial temperature in the experimental dataset
Feed water pump – water flowrate	37.8 l/min
O_2 separator – initial water content	8.35 l (capacity 16.7 l)
O_2 separator – refill water flowrate (if on)	1.8 l/min
O_2 separator – initial water temperature	Initial stack temperature
O_2 separator – purged water flowrate	0.06 l/min
H_2 separator – initial water content	0.5 l (capacity 1 l)
H_2 separator – initial water temperature	Initial stack temperature
H_2 separator – purged water flowrate (if on)	0.9 l/min
Deionized water tank – initial water content	50 l (capacity 100 l)
Deionized water tank – initial water temperature	Initial stack temperature
Deionized water tank – refill water flowrate (if on)	1.8 l/min
Feedwater cooler – heat duty	0 kW
Ambient temperature	22 °C

Furthermore, by finding the value of the stack thermal capacity that minimizes the error on the slope for each of the warm-ups (that is eventually the value of the thermal capacity that minimizes the error on the transient duration) it is possible to determine a value for the thermal capacity (fitting thermal capacity).

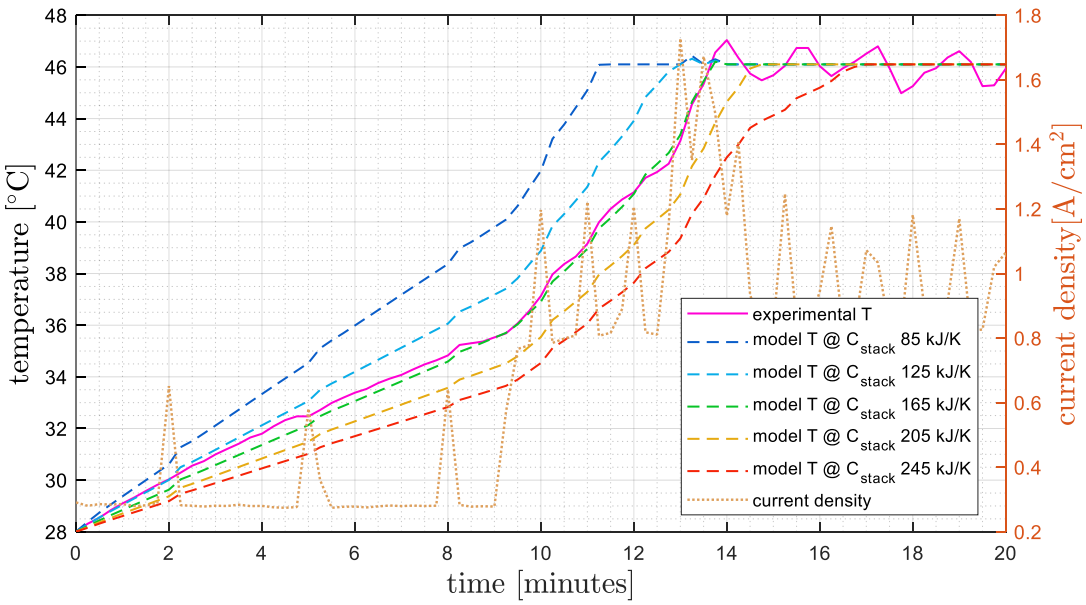

Figure 3.16 – Current density and temperature over time for different values of stack thermal capacity

The eventual presence of a water refill of the O_2-H_2O separator tank from the deionized water tank, which could be at lower temperature, would influence the energy balances of the stack (see paragraph 2.3). In fact, the stack feed water comes from the O_2-H_2O separator, whose temperature is influenced by the refills as well as the oxygen rich flux of water coming from the stack. In the first transient (Figure 3.16) a refill of the oxygen-water separator was present in the simulation before the temperature reached the nominal value, for the duration of about 2 minutes. It is instead unknown when the refill is present in the experimental dataset. A more detailed discussion of this aspect will be carried out later in this paragraph.

Table 3.5 - Fitting stack thermal capacity, maximum error on the temperature at best thermal capacity

# transient	Fitting stack thermal capacity [kJ/K]	Maximum error on the temperature at fitting C_{stack}	
		Absolute [°C]	Relative [%]
#1	*165*	-1.12[1]	-2.48 %
#2	*180*	-1.45	3.66 %
#3	*165*	1.01	2.74 %
#4	*210*	-0.82	-1.90 %
#5	*215*	-1.40	-2.49 %
#6	*220*	-1.33	-2.66 %

As can be seen from Table 3.5, the values of the thermal capacity of the stack that allow to better approximate its thermal behavior varies between 165 kJ/K and 220 kJ/K, and in all cases the error on the temperature along the transient does not exceed 1.45 °C. The reason for such a deviation of 55 kJ/K is identified in the presence of phenomena that influence the thermal balances of the system and whose occurrence and scale cannot be accurately determined by the model. In fact, as illustrated in sections 2.3 and 2.6, the level of water in both the water tank and the oxygen-water separator are controlled by intermittent refills and purge flows, which timing depends on the level of the liquid at the beginning of the operation, and on the setting of the relay (on-off controller). In addition, the initial temperature in these tanks is not known. As it is not possible to match the liquid levels in the model with the actual levels at the beginning of the observations, which are not known, these levels are set

[1] A negative error on temperature means that the model overestimates the temperature, while a negative error on the time means that the model underestimates the time (the model reaches the setpoint faster).

to half the volume of the tank at the beginning of each simulation. The temperature of water in these tanks at the beginning of the simulation is set instead equal to the stack initial temperature. It is however inevitable that the water temperature is different from the initial stack temperature, or that in the model a refill takes place at a time when it is not happening in reality, or vice versa, influencing the evolution of the temperature, and so the apparent thermal capacity.
In fact, analyzing the experimental dataset, it is possible to notice that in all the transients in which the stack thermal capacity that better approximates the thermal behavior results higher (i.e. slow growth in the temperature), there is the presence of some irregularities. An example is shown in Figure 3.17 for transient number 5, where the temperature increase slows down suddenly after minute 12 despite the current density being equal to the one in the first trait from minute 0 to minute 10. This can be representative, for example, of the start of a cold water refill at minute 12.

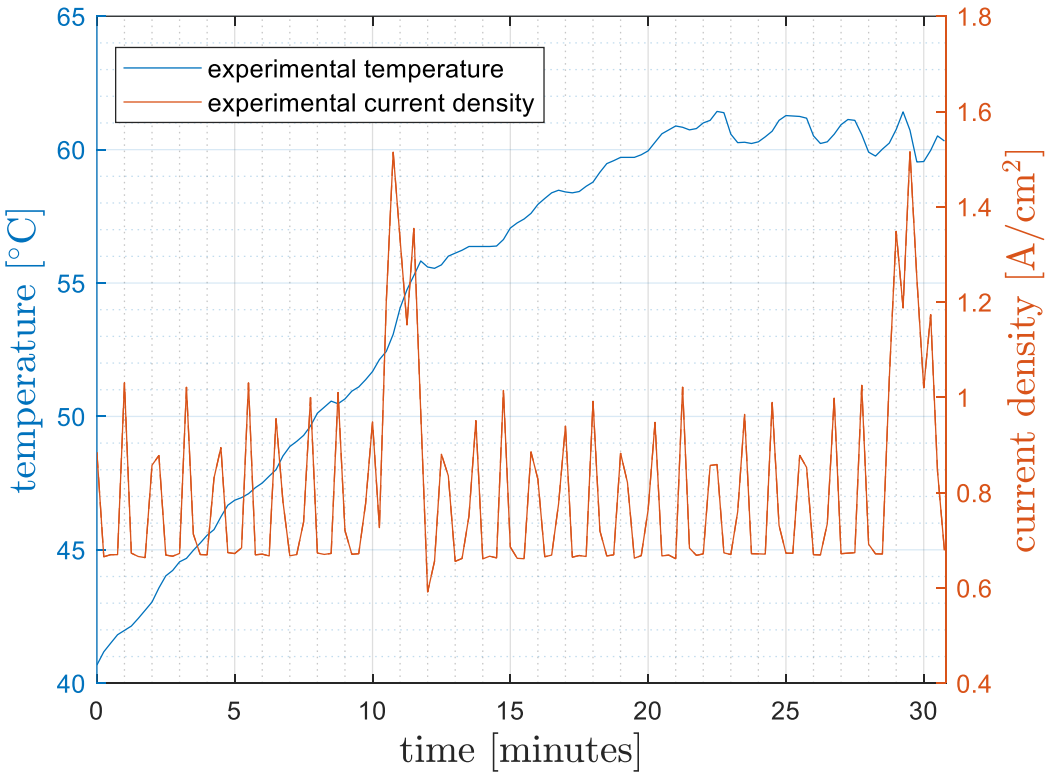

Figure 3.17 - real temperature and current evolution in time of 5th transient

The effect on the simulation results of starting the refill of the oxygen-water tank at different time is investigated, considering transient number 1. With the basic assumption of refilling the tank when it is 25% full, the refill starts after 11 minutes and the optimal thermal capacity results to be 165 kJ/K. Instead, imposing the refill of the oxygen tank to start when the oxygen tank is 10% full (instead of 25%), the stack thermal capacity that better approximates the thermal behavior appears to be 175 kJ/K, in fact in this last case no refill occurs during the thermal transient (the refill starts after the end of the transient). By imposing the refill to start when the tank is 40% full the

apparent thermal capacity decreases to 145 kJ/K, and the refill starts after 5 minutes, for the duration of 5 minutes. As shown in Figure 3.18 the two temperature profiles are identical up to the 5th minute, when the refill of the oxygen tank starts and temperature increase slows down. This means that the presence of a complete refill (last case), or the complete absence of it (second case) can potentially generate a deviation in the thermal behavior and consequently in the evaluation of the stack thermal capacity of 30 kJ/K at minimum, considering that the refills are set at minimum possible flow rates (that is the minimum flow rate allowing to avoid tanks emptying when the system is operated at maximum current for extended periods of time).

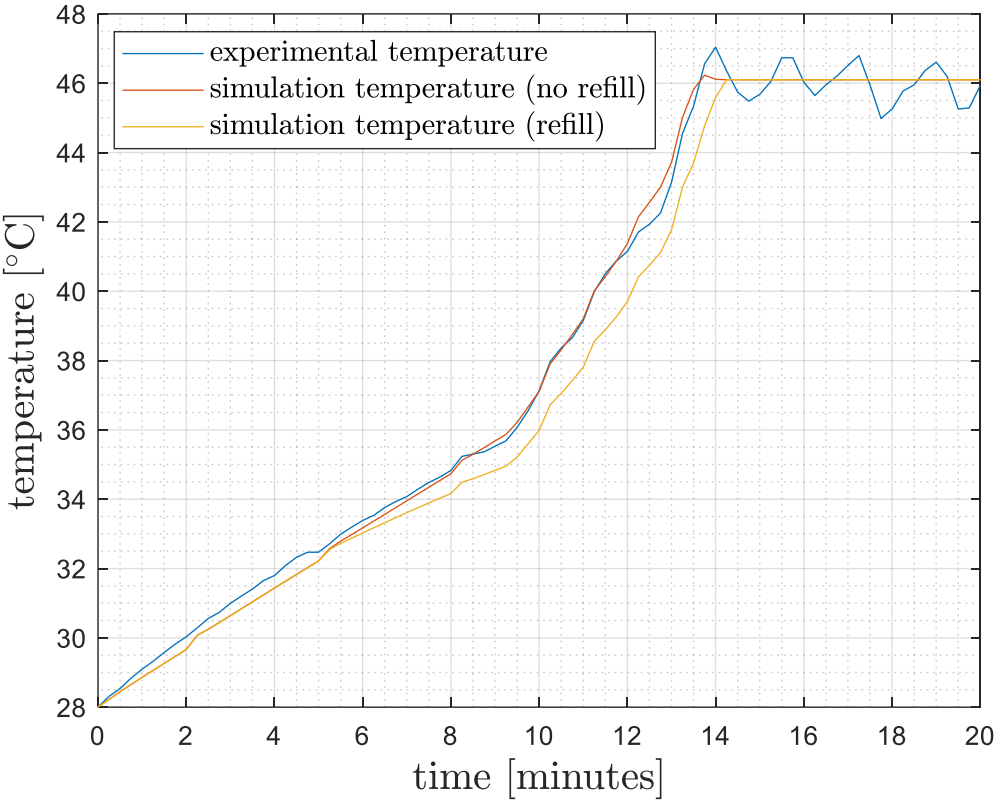

Figure 3.18 - Temperature profile in the 1st transient evaluated experimentally and simulating the system with and without oxygen separator refill, with C_{stack} = 165 kJ/K.

This evidence can partly justify the apparent deviation in the fitting C_{stack} of the different transients, and given that transient *1.* and *3.* are the only ones without irregularities in the temperature trend, 165 kJ/K is assumed as the best value of the C_{stack}, taking also into account that this value generates, for all the 6 cases, an error on the temperature below 3 °C or 7 % and on the transient duration below 5 minutes, or 31% as illustrated in Table 3.6.

Table 3.6 – Maximum error on the temperature and error on the warm-up duration with a stack thermal capacity of 165 kJ/K

	Maximum error on temperature		**Error on duration**	
# transient	**Absolute [°C]**	**Relative [%]**	**Absolute [s]**	**Relative [%]**
#1	-1.12	-2.48 %	4.8	0.58 %
#2	-2.85	-5.34 %	-105	-4.79 %
#3	1.01	2.74 %	15	1.64 %
#4	- 1.60	- 3.78 %	-45	-3.33 %
#5	- 3.09	- 6.37 %	- 285	- 19.19 %
#6	- 2.81	- 5.92 %	- 195	- 30.95 %

Transient *5*. presents a low error up to the 5th minute, where the temperature slope of the experimental data starts deviating from the one resulting from simulation, and the simulated temperature reaches the setpoint before the experimental temperature (4'45" in advance), a water refill of the oxygen water separator is present from minute 11' to 17' in the simulation [Figure 3.19, on the left]. Transient *6.* presents, instead, a different behavior for all the duration of the warm-up [Figure 3.19, on the right].

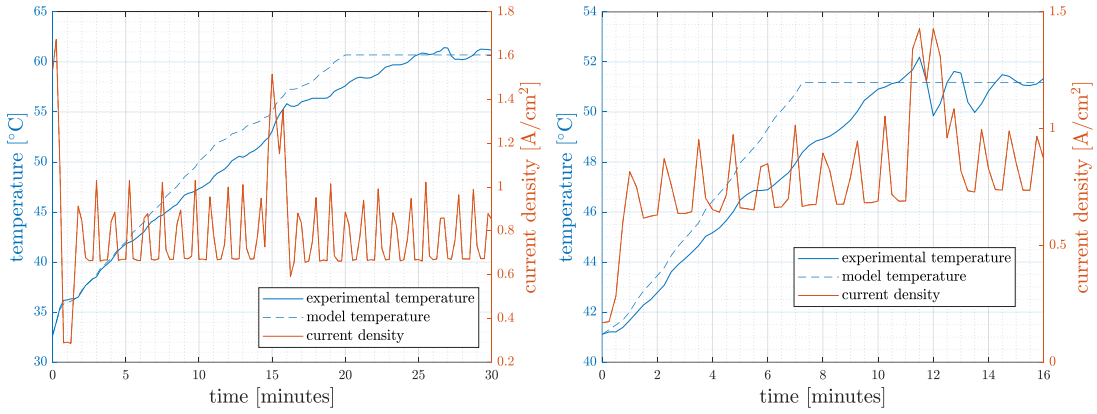

Figure 3.19 - experimental and simulation results on temperature for 5th (left) and 6th (right) transient

A possible explanation of the deviation in transient 6. is that the simulations are operated initializing the temperature in the oxygen and water tanks to the initial stack temperature, but this value can be different. Thus, the initial temperature in the tanks is decreased (Table 3.7, values based on other transients) in order to investigate how simulation results change. This assumption should, in fact, lead to an error that is

bigger the higher the initial temperature of the simulation, since the water temperature in the tanks grows with a delay with respect to the stack temperature, while it is equal to the stack temperature as the system is switched on). It is anyway possible to see, how illustrated in Figure 3.20, that the deviation in the behavior is almost negligible, in case no refill is done, while imposing an anticipated refill of the O_2 separator tank the deviation between the model and experimental results is more significantly reduced, but still high.

Table 3.7 - Temperature initialization of the 3 main tanks of the electrolyzer system

Tank	**Initial temperature**
O_2 separator	Stack temperature – 1 °C
Deionized water	Stack temperature – 10 °C
H_2 separator	Stack temperature – 2 °C

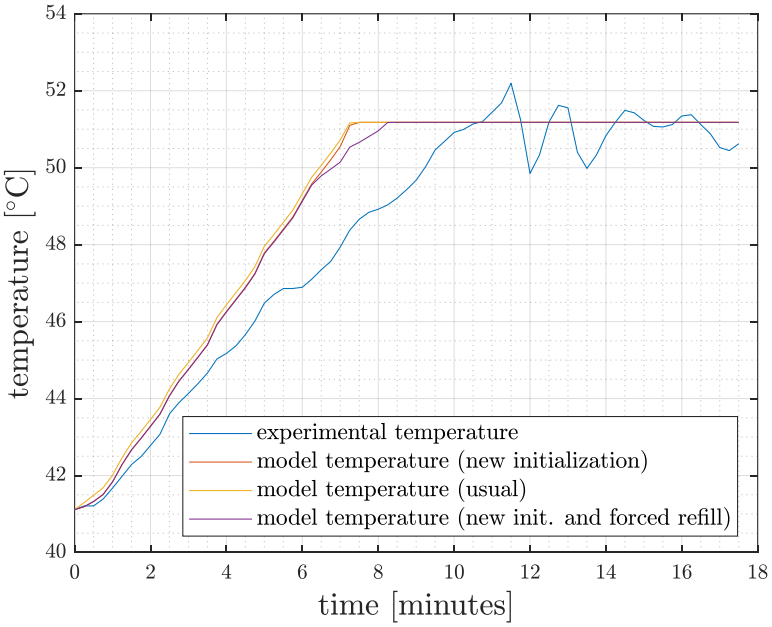

Figure 3.20 - Experimental temperature and model temperature for the two initialization approaches (with and without refill)

Since the deviation must therefore be due to other unknown phenomena, it is considered more reliable to choose to give greater importance to those transients that do not have irregular behavior for the validation of the thermal capacity of the stack.

3.2.4 Thermal behavior validation under dynamic conditions

Once the thermal behavior of the model during warm-up is validated it is necessary to validate the thermal behavior in dynamic conditions, namely when the stack current undergoes strong fluctuations in the case of coupling with a renewable power source. In order to verify that the model maintains a temperature value of the stack sufficiently similar to the experimental one also in dynamic conditions, the value of the current of

the stack measured during the coupling with the wind-like power is given in input to the complete model. The current profile given in input is the one measured between hour 140 to 160 during experiments, where both ascending and descending stack power ramps are present (Figure 3.21), while the pressure setpoints for the anode and the cathode are set equal to the average ones measured during experiments in the time window considered, corresponding to 2.8 bar_a and 32.8 bar_a respectively.

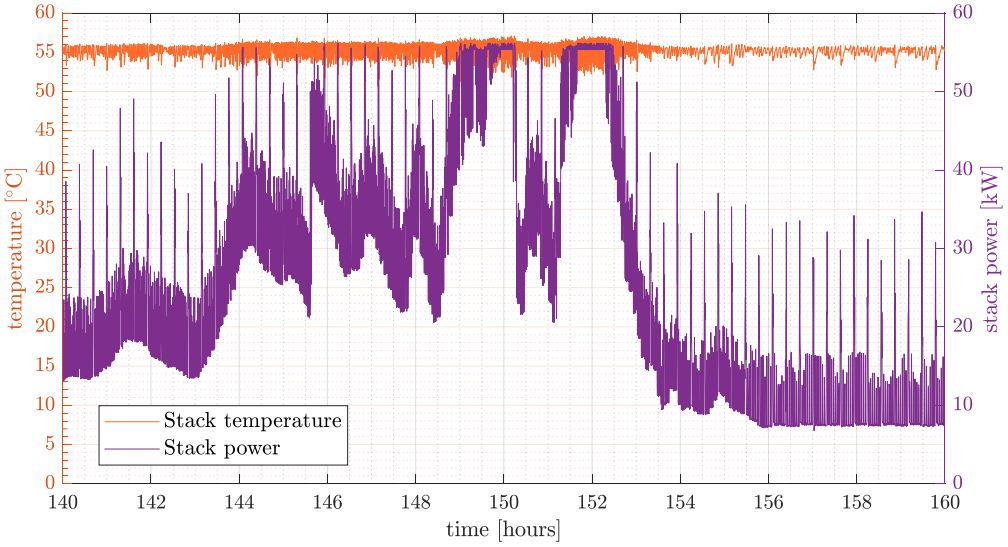

Figure 3.21 – Stack power and temperature over time measured during the coupling of the electrolyzer with the wind power source during the time window considered for the validation of dynamic thermal behavior

The simulation results show that the system is capable of keeping the stack temperature around the setpoint value of 55 °C (Figure 3.22) as the real system is, even during fast and sudden fluctuations of the power as the ones used for the simulation.

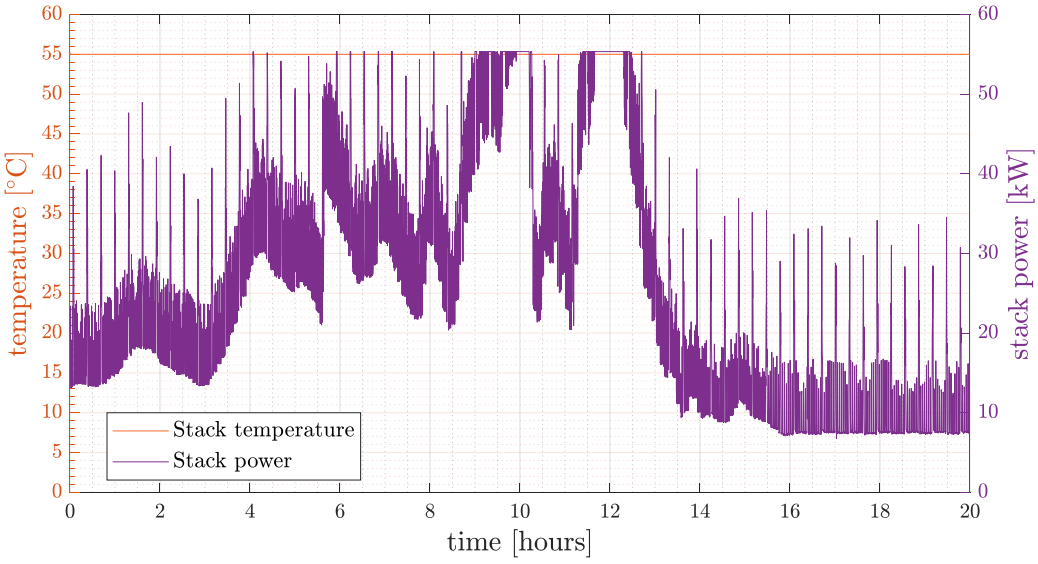

Figure 3.22 - Stack power and temperature over time from simulation of the coupling of the electrolyzer with the wind power source

In fact, the stack feed-in water heat exchanger's PID continuously regulates the refrigerant flow rate in order to keep the temperature at the setpoint value (see section 2.7 for a more detailed explanation). As illustrated in Figure 3.23, for higher currents the coolant mass flow rate increases, since higher amount of heat must be removed from the stack in order to maintain the temperature setpoint, on the other hand, when the current density is low the coolant flow drops close to zero since the amount of heat to be removed is lower.

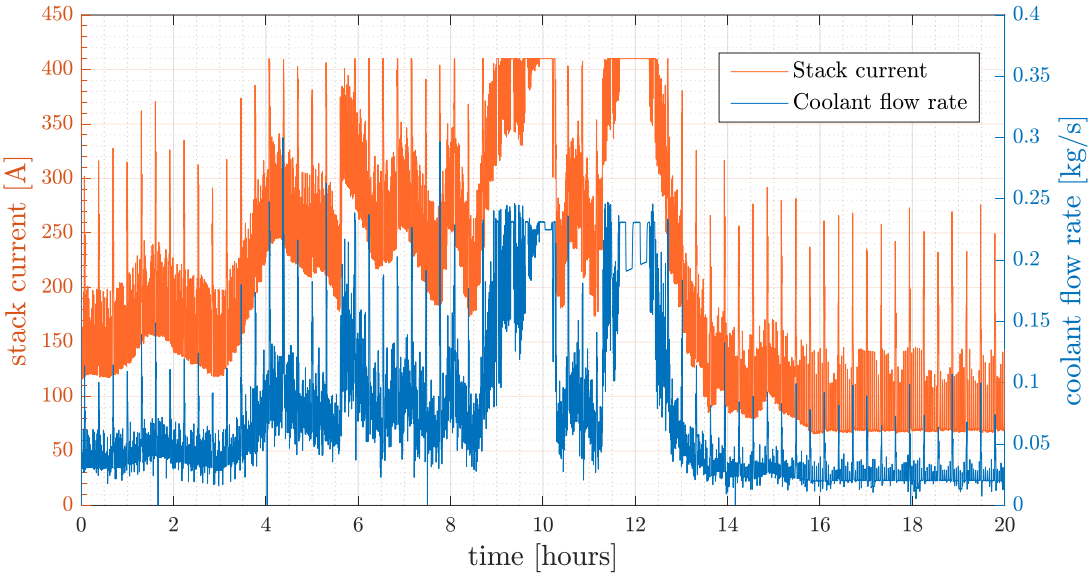

Figure 3.23 - Stack current and feed-in water cooler refrigerant fluid mass flow rate over time from simulation of the coupling of the electrolyzer with the wind power source

3.3 Hydrogen pressure in the system

Hydrogen pressure evolution is an important parameter for evaluating the readiness of the system in delivering hydrogen when switched on. In fact, hydrogen pressure is controlled by a backpressure valve, so the delivery starts only when the pressure of hydrogen downstream of the drying process reaches the pressure setpoint of 30 bar_g. By knowing the hydrogen production and loss for the PSA regeneration (which is reported to account for the 90% of hydrogen losses at nominal conditions), and the volume upstream the backpressure valve, it is possible to model the hydrogen pressure dynamics (section 2.5). The volume upstream the valve is mainly composed by the hydrogen separator volume and the PSA volume (pipeline's volume is neglected), which are known and equal respectively to 1 l and 1.6 l. The total volume available for the gas is anyway different from 2.6 l, since the volume occupied by liquid water in the hydrogen separator tank must not be considered. This volume is assumed to be half of the hydrogen tank at the beginning of the simulations, and then may vary during operation as already described in section 2.4.

The hydrogen losses for PSA regeneration are due to a dried hydrogen purge downstream of the actively adsorbing PSA bed, passing through an orifice, and sent to the saturated bed to purge it of the entrained moisture before the bed switches back, as explained in detail in section 2.5. The mass flow rate of the hydrogen loss is therefore orifice driven, and as such it's a function of the hydrogen pressure [5]. A simplified model for the orifice is implemented, and it's description is present in section 2.5.
As treated in that section, the outgoing mass flow rate is calculated through a revised form of the "ASME" equation [10]:

$$\dot{m} = c \cdot \sqrt{2 g \rho_1 \Delta p} \tag{3.4}$$

where A_0 [m] is the orifice area, g [m/s^2] is the gravity acceleration, ρ_1 [kg/m^3] is the density of hydrogen upstream the valve, Δp [Pa] is the pressure difference across the valve (atmospheric pressure is considered downstream the orifice) and c is a coefficient enclosing the expression $(KY) \cdot A_0$, assumed to be constant in the operating range of interest. Thus, the orifice is calibrated by determining the constant c as the mass flow passing through the orifice at nominal conditions (Δp = 30 bar) is known to be equal to $0.0744 \ \frac{kg}{h}$ [5].

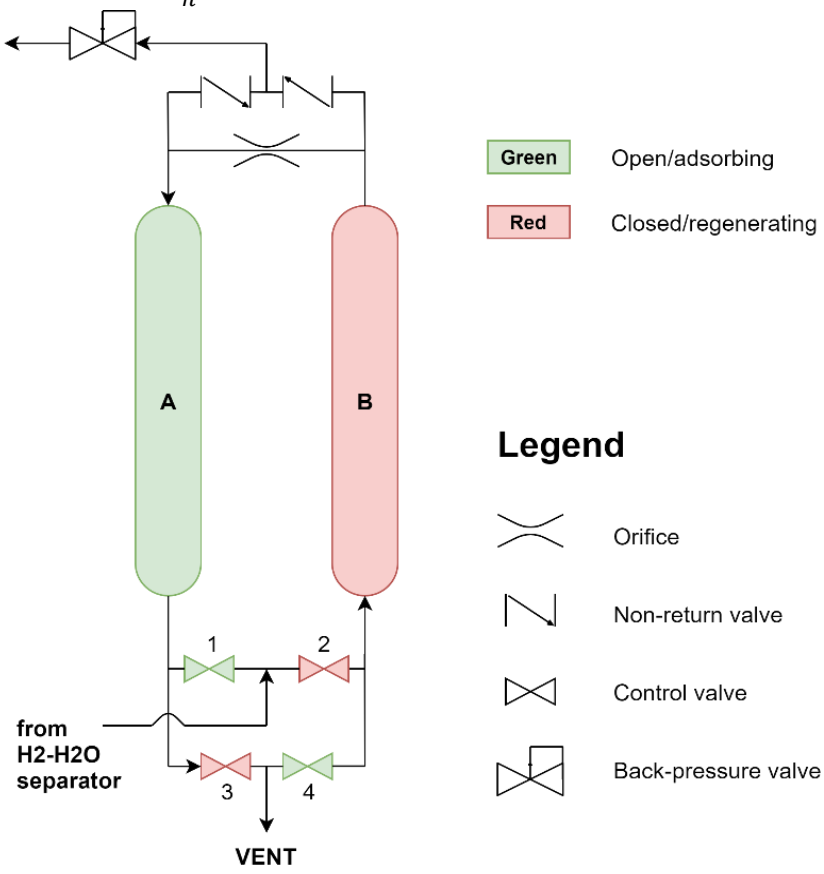

Figure 3.24 - Simplified diagram of the PSA hydrogen drier, showing in green the bed in operation and in red the bed in regeneration mode.

Hydrogen pressure is computed as $p = \frac{R^* \cdot T}{v}$ by following the equation of state of ideal gases, while v [m^3/kg] is computed as the PSA and hydrogen separator volume (0.0026 m^3) minus the volume of liquid contained in the hydrogen – water separator tank, initialized at half of its capacity at the beginning of each simulation, divided by the total mass of gas (hydrogen saturated with vapor) accumulated in the hydrogen tank and PSA.

As the system is switched on, a first phase during which all the hydrogen generated is vented is present. This phase has the purpose of expelling any impurities (oxygen and nitrogen) that may have entered when the system was shut down due to the pressure decrease before it gets pressurized and operative. After this phase ends, and hydrogen ceases to be purged, the hydrogen separator tank, PSA and all the other hydrogen-side components get pressurized. Each of the six start-up transients already introduced in section 3.1.1 (Figure 3.6) is then simulated (identifying the phase where the pressure starts increasing) with the entire Simulink model starting from the same pressure of the experimental data and imposing the same current profile over time. The 3rd and the 6th transients don't present a pressure transient, probably due to some cutting of the data, so they are not simulated.

Current density and anode pressure experimental profiles over time are imposed to the model, which simulates the operation starting from the same cathode pressure of the experimental data, imposing a pressure setpoint equal to the maximum pressure measured in the experimental campaign (the pressure range is so the same in the simulation and experimental data). For all the other assumptions and initializations, refer to Table 3.4.

In Table 3.8 results from experiments and simulations are shown. Please note that being the available experimental data averaged on 15 seconds intervals, an error of 15 seconds is related with the discretization step.

Table 3.8 – Experimental and model results for the hydrogen pressure transients

	Experimental data		**Simulation results**	
# transient	**Duration [s]**	**Pressure range [bar_g]**	**Duration [s]**	**Error on duration [s]**
#1	45	0.29 – 32.17	45	0
#2	30	27.43 – 31.82	15*	-15
#3	-	-	-	-
#4	45	1.20 – 27.41	45	0
#5	45	2.46 – 29.75	30	- 15
#6	-	-	-	-

*Data step is 15'

Pressure losses in the pipes downstream the hydrogen separator tank and in the PSA bed are neglected in the simulation (it is assumed that the pressure in the hydrogen separator tank is equal to the pressure downstream the adsorption beds). Pressure losses are also the reason why the final pressure of each transient generally differs from 30 bar_g in experimental data, and it is slightly higher: in fact, the cathode-side pressure is experimentally measured in the hydrogen tank, thus neither taking into account for pressure losses downstream of it, nor the interaction with the gas turbine. Results are illustrated in Figure 3.25.

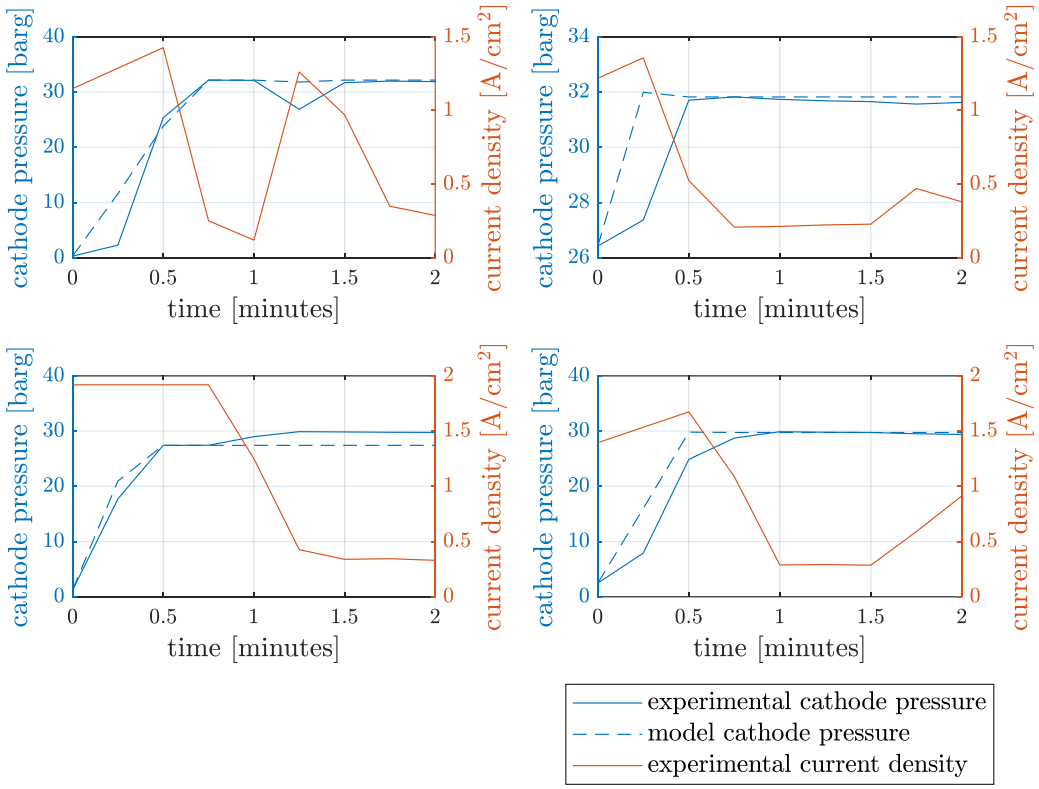

Figure 3.25 - Hydrogen pressure transients and corresponding current density over time

3.4 System BoP

For a final validation of the Simulink model, the balance of plant components are included in order to compare the results of system efficiency, system consumption and hydrogen production with data previously collected on the electrolyzer under analysis and published in “Experimental dynamic dispatch of a 60 kW proton exchange membrane electrolyzer in power-to-gas application” [5]. All the ancillary power systems are included, except for the air-cooled chiller which has the task to cool down the refrigerant sent to the feed-in water cooler and drying system, and the hydrogen compressor, which are considered outside the system boundaries. Thus, the included

auxiliaries comprise the inverter, the feed-in water pump, circulation pump, oxygen-water separator pump and a fan. In Table 3.9 the values of the main parameters of the simulation are shown.

Table 3.9 – Main operating parameters for nominal, steady state operation

Parameter	**Nominal value**
Operating temperature	55 °C
Ambient temperature	22 °C
AC/DC converter efficiency	93%
Anode pressure [bar_g]	1.5 bar_g
Cathode pressure [bar_g]	30 bar_g
Gross power [kW]	62 kW
Fan consumption [kW]	0.5 kW (constant)
Pumps isentropic efficiency	80%
Pumps mechanical efficiency	97%
Pumps electrical efficiency	98%

Pumps consumption is computed from the pressure drop inside the pipes:

$$P_{el,Pump} = \dot{m} \cdot \frac{\Delta p}{\rho} \cdot \frac{1}{\eta_{is,Pump} \cdot \eta_{mech} \cdot \eta_{el}} \tag{3.5}$$

3.4.1 Full load operation

The system at full load operation and steady state is simulated with the entire model and the performances measured from the model compared with the benchmarking and experimental results at full throughput. Performances are evaluated through stack gross efficiency:

$$\eta_{gross,HHV} = \frac{\dot{m}_{H_2,OutStack} \cdot HHV_{H_2}}{P_{gross}} \tag{3.6}$$

and the system net efficiency:

$$\eta_{net,HHV} = \frac{\dot{m}_{H_2,OutSystem} \cdot HHV_{H_2}}{\frac{P_{gross}}{\eta_{inverter}} + P_{auxiliries}} \tag{3.7}$$

While gross efficiency refers to the stack only, the net efficiency takes into account both hydrogen losses in the purification unit and the auxiliaries power consumptions (excluding the chiller and the hydrogen compressor). Efficiencies are computed on HHV basis, for reasons of comparison with the experimental results in [5].

At full load producer specifications claim a net efficiency of 57.24% (gross efficiency not specified), experimental results revealed a system net efficiency of 57.47% and a stack gross efficiency of 72.03% after 100 h of operation [5], while simulation results show a system net efficiency of 58.78% and a stack gross efficiency of 71.17%.

3.4.2 Part load operation

For part load operation, it is possible to compare the system net energy consumption (kWh_{el}/kg of hydrogen delivered) computed from the model to a plot of the experimental results available in [5].

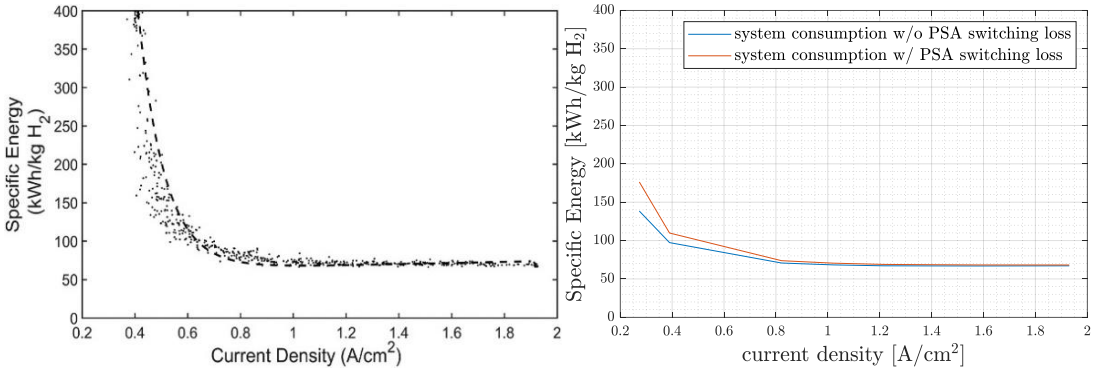

Figure 3.26 - Specific energy consumption vs. current density (experimental results on the left, simulation results on the right) [2]

Coherently with the assumption of constant auxiliary consumption and hydrogen loss, which only depends on cathode pressure (see section 3.3), the specific energy consumption for unit mass of hydrogen produced remains almost flat as current density is reduced down to 0.8 A/cm^2 (corresponding to nearly 40% of the load), then increasing exponentially for lower loads. Nevertheless, when considering only the hydrogen loss deriving from adsorption beds regeneration by means of the hydrogen flux passing through the orifice, the experimental specific consumption increases more quickly than the simulated ones when going below 30% of the load, reaching highest deviation at 0.4 A/cm^2 (100 kWh/kg vs. 400 kWh/kg, blue line in Figure 3.26).

The deviation decreases if the hydrogen loss due to the switching of the active PSA bed is included in the model (orange line in Figure 3.26). In fact, as can be inferred from the experimental data, the active adsorption bed is switched every 18 minutes (section 3.3). This operation, which is carried out by closing the saturated bed's valve and opening the regenerated one's (Figure 3.24), causes the loss of the hydrogen contained in the saturated bed, which is vented for depressurization. For sake of

[2] Experimental results below 0.4 A/cm^2 are not present because it was not possible to make the system work at lower current density. Therefore, the simulations' results below 0.4 A/cm^2 are of poor interest and ignored for the validation purposes

simplicity, instead of simulating the hydrogen loss every 18 minutes, an average of the hydrogen loss over time is computed and implemented in the model:

$$\dot{m}_{H_2,loss} = \frac{V_{PSA} \cdot \Delta\rho_{H_2,regeneration}}{t} \tag{3.8}$$

where V_{PSA} is the PSA net volume (1.6 l), t is the time between two regenerations (18'), $\Delta\rho_{H_2,regeneration}$ is the density difference before and after regeneration namely the difference between the density of hydrogen at 30 bar and 1 bar, computed by the use of the ideal gas equation of state corrected with the compressibility factor *Z*, taking into account the non-ideal behavior. All calculations are made assuming a temperature of hydrogen of 25 °C. The result is a hydrogen loss equivalent to a continuous flux of $4.0 \cdot 10^{-6}$ kg/s (including a 10% increase for hydrogen contained in the pipes). Numerical results are shown in
Table 3.10.

Table 3.10 – System efficiency at full net load (experimental and simulation results) and system efficiency and consumption at part load (simulation results)

	Experimental		**Simulation**			
Net load	Net efficiency	Gross efficiency	Net efficiency	Gross efficiency	System consumption [kWh/kg]	System consumption w/ switching loss [kWh/kg]
100%	57.47%	72.03%	58.78%	71.17%	67.105	68.169
80%	-	-	58.96%	73.47%	66.900	68.232
70%	-	-	58.87%	74.90%	66.997	68.524
60%	-	-	58,77%	76.85%	67.117	68.917
50%	-	-	57.75%	78.64%	68.298	70.542
40%	-	-	55.75%	80.85%	70.747	73.786
20%	-	-	40.52%	86.46%	97.346	109.842
15%	-	-	28.50%	88.34%	138.458	176.365

The system net efficiency at full load computed by the model, considering the hydrogen loss due to the depressurization of the saturated bed reaches 57.86%, a value closer to the experimental efficiency at full load (57.47%) with respect to the net efficiency computed without this hydrogen loss (58.78%).
Nevertheless, as it's possible to notice in Figure 3.26 (orange line), the system net consumption at part load reported by the model differs the more the load is reduced from the experimental net consumption. Thus, a simplified model for computation of the Faradaic efficiency, which is assumed constant and equal to 99% up to now (section 2.2.1), is implemented.

Faradaic efficiency is defined as:

$$\eta_F = \frac{\dot{m}_{H_2}^{C,out}}{\frac{I}{2F}} \tag{3.9}$$

where $\dot{m}_{H_2}^{C,out}$ [kg/s] is the mass flow rate of hydrogen coming out of the cathode, I is the stack current [A] and F is the Faraday constant (96485.33 C/mol). As seen in section 2.2 the Faradaic efficiency is smaller than one because of gas crossover across the membrane:

$$\eta_F = 1 - \frac{\dot{m}_{H_2}^{back}}{\frac{I}{2F}} \tag{3.10}$$

where $\dot{m}_{H_2}^{back}$ is the hydrogen flow diffusing back from cathode to anode (crossover flux). A simplified definition of the crossover flux is here reported [60]:

$$\dot{m}_{H_2}^{back} = \frac{1}{2K_{H_2}}\left(\frac{\nu p_{H_2}^{C}}{2} + \frac{D_{H_2}}{\delta_m} p_{H_2}^{C}\right) \tag{3.11}$$

where K_{H_2} is the Henry constant of hydrogen, D_{H_2} is the dissolved hydrogen diffusivity, $p_{H_2}^{C}$ is the partial pressure of hydrogen at the cathode, δ_m is the membrane thickness and ν is the superficial velocity of liquid water related to the total pressure gradient and dependent on the pore-water viscosity μ and hydraulic permeability k_p [60]:

$$\nu = \frac{k_p}{\mu}\frac{p^c - p^a}{\delta_m} \tag{3.12}$$

The Faradaic efficiency thus increases with the membrane thickness, but the increase in the membrane thickness increases ohmic losses [61] and even though technological progresses allowed to obtain very high Faradaic efficiencies with respect to the past [9], this efficiency remains a critical issue when designing electrolyzers. Furthermore, Faradaic efficiency decreases with the increase in hydrogen pressure and anode-cathode pressure difference. By looking at eq. (3.10) and assuming $\dot{m}_{H_2}^{back}$ to be only dependent on pressure and temperature which are fixed for all current densities once steady state is reached it is possible to develop a simple relation which links Faradaic efficiency with current density in the form:

$$\eta_F = 1 - \left(\frac{a}{i}\right) \tag{3.13}$$

Such kind of relations has already been demonstrated to be able to provide an estimate of the Faradaic efficiency at different currents with a very low error for PEM electrolyzers [9]. The parameter a [A/cm^2] incorporates all the characteristics of the electrolyzer in the term $\frac{\dot{m}_{H_2}^{back}}{2F}$ at a given temperature and cathode pressure (55 °C and 31 bar$_a$ in our case), and can be reverse-engineered by knowing the system efficiency at full load. In fact, imposing a Faradaic efficiency such that the model and the experimental data provide the same net efficiency at nominal load (57.47%), the parameter a turns out to be equal to 0.03113 and the Faradaic efficiency can be estimated for each current density (3.13), as shown in Figure 3.27:

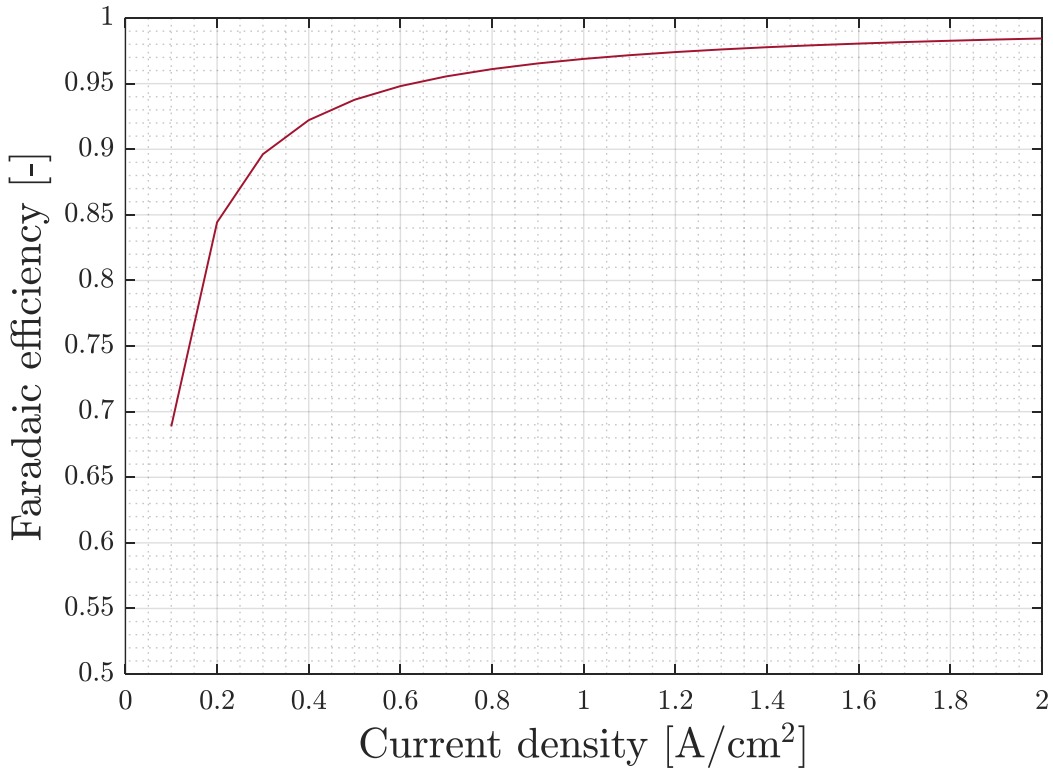

Figure 3.27 - Faradaic efficiency computed by means of the simplified correlation

The new Faradaic efficiency is then included in the model and results on the system consumption are illustrated in Figure 3.28. Please note that, being no experimental data present for current densities below 0.4 A/cm^2 (real system doesn't work below that value), also the values of the Faradaic efficiency found below 0.4 A/cm^2 are not considered and a minimum Faradaic efficiency equal to 92%, found at minimum load, is considered acceptable for such technology.
The PSA switching loss is also included (right plot in Figure 3.28), considering one switching every 18' (best case, blue line) and the worst case scenario where two switching of the PSA active bed are present in 18' of data recording (red line).

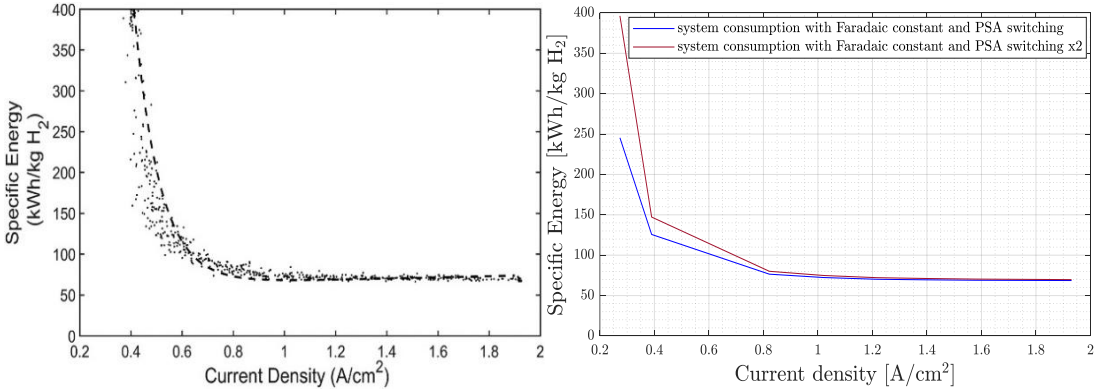

Figure 3.28 – Specific net energy consumption of the system evaluated experimentally (left) and by means of the model including the variable Faradaic efficiency model and the PSA switching loss (right)

The numerical results are reported in Table 3.11.

Table 3.11 – New system net efficiency and consumption with the new Faradaic efficiency computation method for the two cases of PSA switching loss

		Simulation results			
		PSA switch loss (normal)		PSA switch loss (high)	
Net load	***Current density [A/cm^2]***	**System net efficiency**	**System consumption [kWh/kg]**	**System net efficiency**	**System consumption [kWh/kg]**
100%	*1.9305*	57.47%	68.635	56.55%	69.750
80%	*1.5774*	57.17%	68.993	56.02%	70.407
70%	*1.3965*	56.75%	69.508	55.44%	71.153
60%	*1.2155*	56.18%	70.206	54.65%	72.173
50%	*1.0215*	54.53%	72.341	52.69%	74.863
40%	*0.8217*	51.55%	76.511	49.26%	80.077
20%	*0.3899*	31.39%	125.678	26.79%	147.220
15%	*0.2735*	16.07%	245.389	9.95%	396.380

The model results are still slightly underestimated below 0.6 A/cm^2 but within the range of experimental data, thus acceptable.
Specific energy consumption of the system can be broken down into 4 main sources; the stack energy consumption, energy losses due to the AC/DC conversion, the auxiliaries balance of plant consumption and the energy loss associated to the physical hydrogen loss. While stack consumption is dominant for net loads higher than approximately the 40%, for lower net loads the physical hydrogen loss becomes the main consumption share of the system, de facto making it economically inconvenient

to run the system. In Figure 3.29 the share of the 4 contributions on the global energy consumption at different loads from the in simulations is illustrated and compared to experimental results. Physical hydrogen losses include the PSA regeneration and switching losses, the hydrogen vented from the flash downstream of the hydrogen – water separator and the hydrogen loss due to the Faradaic efficiency reduction.

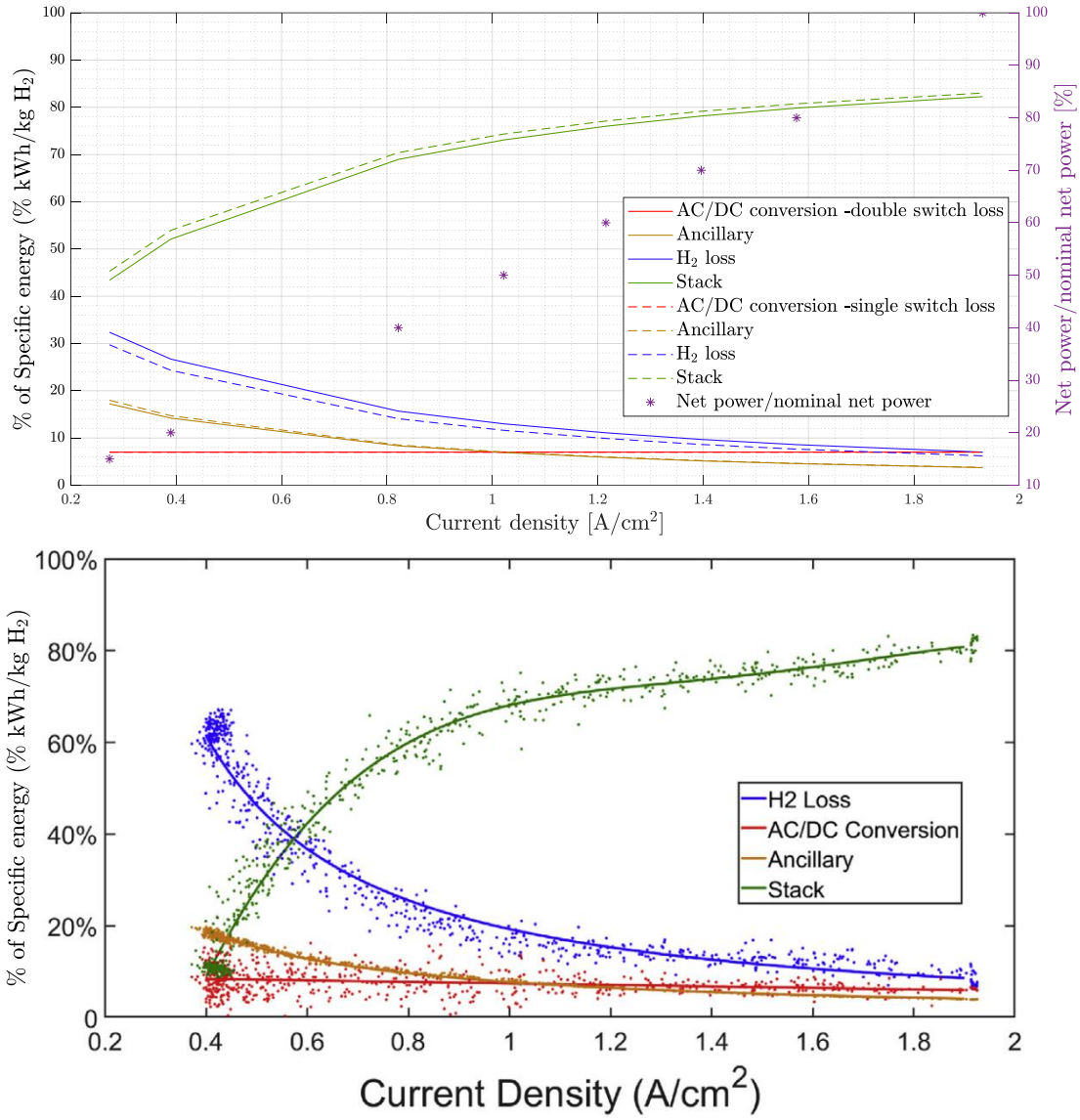

Figure 3.29 - Sources of energy consumption in electrolyzer system per unit kg H_2 produced from simulations (top figure) and experimental (figure below)

It is possible to notice that hydrogen losses are slightly underestimated in the simulations with respect to the experimental results. This last analysis should be taken as a qualitative comparison showing that relatively small hydrogen losses have an exponentially higher weight on efficiency at low load, while their influence can be considered negligible at high loads. It is therefore of primary importance, when considering experiments, to know their timespan and the frequency of periodic events

such as the switching of the active adsorption bed, considered as the main cause of the higher dispersion of experimental results at low loads in Figure 3.26.

4

CHAPTER 4 – SYSTEM OPTIMIZATION

This chapter has the purpose to determine which are the best measures to be taken in order to optimize the operation of the electrolyzer system in a context of non-dispatchable power sources, due to coupling with renewable power sources or provision of grid balancing services. Firstly, in section 4.1 the system warm-up is considered, showing the actual performances and analyzing different scenarios that could lead to a better and more performing operation of the system during start-up. Then, different ways to increase partial load performances are identified, starting from the reduction of the hydrogen losses (sections 4.2.1 and 4.2.2), which have been demonstrated to be the main cause of performance decline at partial load (section 3.4.2, Figure 3.29) and then going to analyze the performance improvement deriving from optimizing the use of auxiliaries at partial load (section 4.2.3). Finally, the operation with high cathodic pressures is analyzed and compared with the classic use of a compressor (section 4.3).

4.1 System start-up optimization

System start-up is of primary importance in a context of intermittent power sources since it determines after how much time the system starts producing hydrogen and the efficiency with which it does, before reaching nominal conditions.
A sensitivity analysis on different net power loads is performed in paragraph 4.1.1 in order to show the transient duration and performances during warm-up for different loads in the base case (actual system). Then, modifications to the system components and system operation are proposed in order to increase the system readiness in producing hydrogen with a high efficiency since the first minutes of operation, as changing the oxygen-water separator refill settings (paragraph 4.1.2) and by performing a preheating of the water accumulated in the oxygen-tank (hot stand-by), in paragraph 4.1.3. The entire analysis of start-up optimization considers timespans of maximum 1 hour from the beginning of operation, since after 1 hour of operation this kind of system can be already considered to be operating at nominal and steady state conditions at any load.

4.1.1 Base case analysis

System start-ups are simulated, imposing different loads in input to the model, constant over time for one hour, and the conditions and setpoints in Table 4.1, starting from 20% to full load (100%). Adsorber's switching losses and Faradaic efficiency dependence on current are included in the model (section 3.4.2). At the beginning of the simulations, all the tanks and separators are considered in thermodynamic equilibrium with the external environment (same temperature) and half full.

Table 4.1 – Main operating conditions and setpoints of the simulations

Variable	Initial value	Final value
Ambient temperature	15 °C	15 °C
Stack temperature	Ambient temperature	55 °C
Anode pressure	1.01 bar_a	2.50 bar_a
Cathode pressure	1.01 bar_a	31.00 bar_a

Five simulations are run imposing a constant net electrical power entering the system equal to 20%, 40%, 60%, 80% and 100% of the nominal power (62 kW). Each simulation is characterized by a different time to reach nominal, steady state condition, given that the temperature increase is proportional to the current (i.e. the power), as illustrated in Figure 4.1.

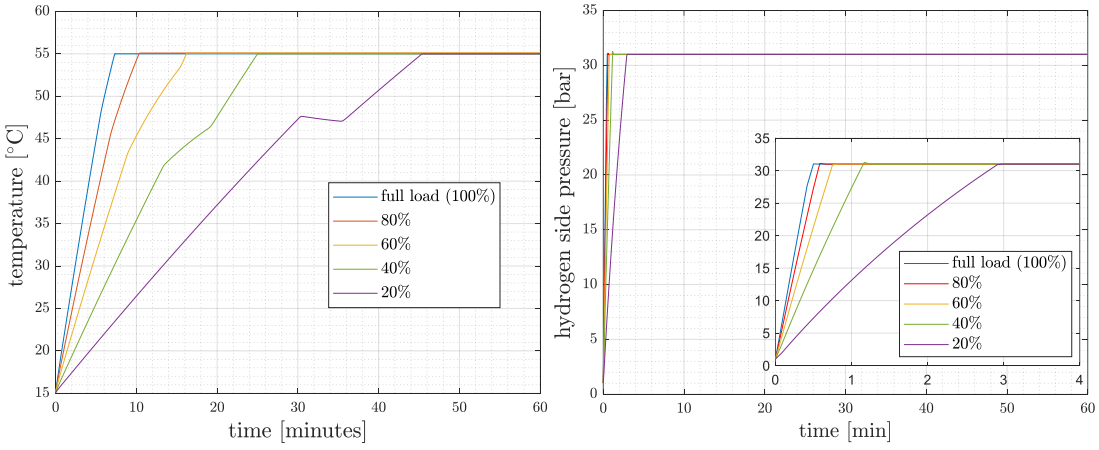

Figure 4.1 – Temperature (left graph) and pressure (right graph) profiles over time from the 5 simulations at different loads

It is possible to notice discontinuities in the temperature profiles, the more accentuated the lower the power at which the system is operated, due to the refill of the oxygen-water separator with a flux coming from the deionized water tank, which has a lower temperature with respect to the oxygen – water separator.

According to polarization curves theory (sections 1.4.1 and 2.2.1), cell voltage decreases with the temperature increase, thus each start-up is characterized by a first phase in which stack voltage decreases and current increases due to the power-based control of the system (Figure 4.2).

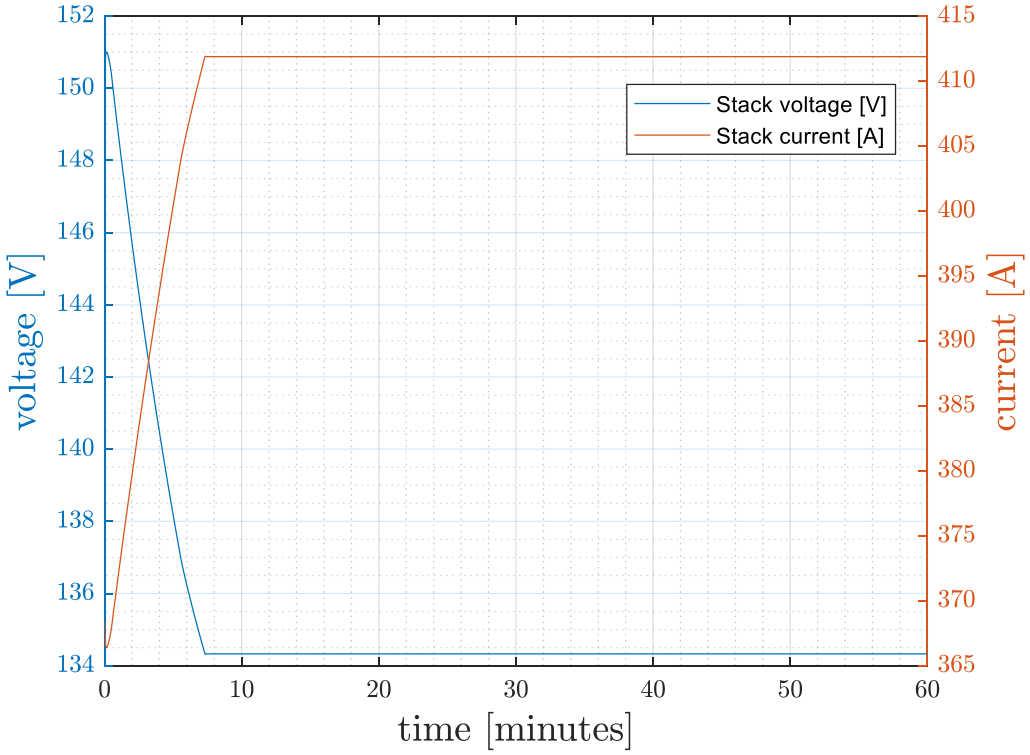

Figure 4.2 – Stack current and voltage profiles over time from the simulation at full power

Being the current proportional to the hydrogen produced, according to Faraday's Law (sections 1.4.1 and 2.2.1), and the power constant, the maximum efficiency of the electrolyzer is reached after this first transient phase. It is important to take into account the global efficiency of the system from the beginning of operation up to a certain time *t*, thus, an average net efficiency, based on the cumulated hydrogen production, is defined as:

$$\bar{\eta}_{net,HHV}(t) = \frac{\int_0^t \dot{m}_{H_2,OutSystem,t} \cdot HHV_{H_2} \cdot dt}{\int_0^t P_{net} \cdot dt} \tag{4.1}$$

The value of the average net efficiency over time for every transient is shown in Figure 4.3. It can be observed a first phase in which no hydrogen exits the system, being all the hydrogen exiting the stack used to pressurize the hydrogen tank and the adsorption bed. After this first phase the system starts producing, efficiency rises quickly and then

stabilizes, tending asymptotically to the maximum value achievable at the corresponding load.

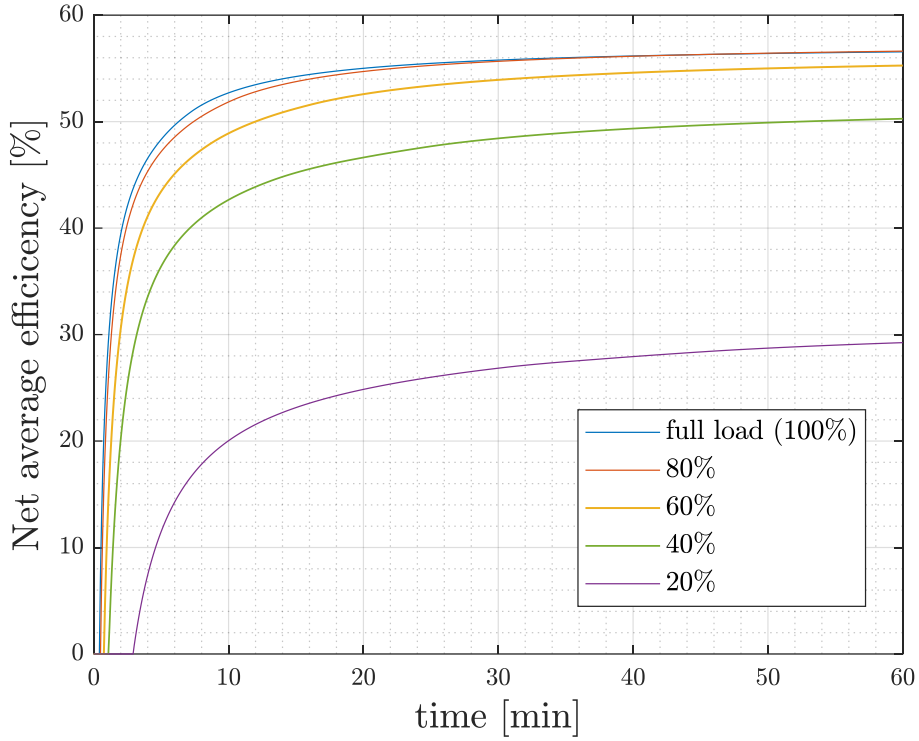

Figure 4.3 – Net average efficiency of the system for each of the 5 simulations over time

The time the system needs to reach the asymptote is determined as the time needed by the system to reach an average efficiency equal to 95% of the maximum efficiency reachable in those conditions. This value is reported together with the time needed by the electrolyzer to start delivering hydrogen (pressurization time), the transient duration (time to reach nominal temperature and thus, maximum net efficiency), the maximum net efficiency and the average net efficiency after one hour in Table 4.2.

Table 4.2 – Time needed by the system to deliver hydrogen and to reach nominal temperature, maximum efficiency time to reach asymptotic cumulative efficiency (95% of max efficiency) and cumulative efficiency after one hour for the 5 loads considered

Net load	**Time to deliver hydrogen**	**Warm-up duration**	**Max net efficiency**	**Time to reach asymptotic av. efficiency**	**Average efficiency after one hour**
100%	25 s	07’ 20”	57.33%	16’ 15”	56.55%
80%	30 s	10’ 20”	57.58%	20’ 00”	56.62%
60%	45 s	16’ 15”	56.62%	28’ 40”	55.27%
40%	65 s	25’ 00”	52.12%	42’ 35”	50.27%
20%	175 s	45’ 45”	31.82%	> 60’	29.24%

By drawing an horizontal line intercepting the curves in Figure 4.3 corresponding to the minimum efficiency that makes it convenient to run the electrolyzer it is possible,

knowing the power that will be fed into the system, to determine the minimum time during which this power should be fed. Considering the case in Figure 4.4, where the minimum acceptable net efficiency is set to 50%, it is possible to understand that, given a constant power profile over time fed into the electrolyzer, it is never convenient to switch on the system if this power is the 20% of the maximum power of the electrolyzer, while for a power corresponding to the 40% of the maximum load it is convenient only if the system is kept operating for at least 52 minutes, 12 minutes for the 60% load and only 7 minutes and 30 seconds and 6 minutes and 20 seconds for 80% and 100% load, respectively. From this example, it is possible to notice how the average net efficiency of the system changes quickly in the first minutes of operation, so that it is essential to predict this efficiency and to know how long the system will have to be switched on in case of a request for intermittent operation (e.g. grid balancing services).

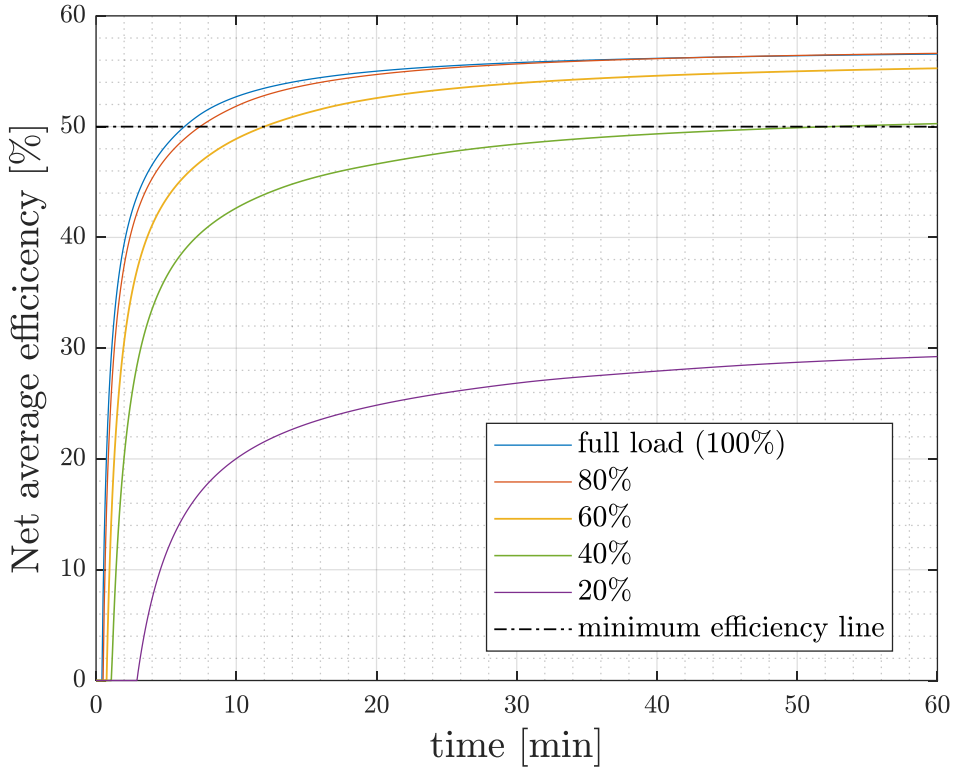

Figure 4.4 – Net average efficiency with example of minimum efficiency line

4.1.2 Smart refill management

It is clear from the previous paragraph (Figure 4.4), that the electrical power entering the electrolyzer system strongly influences both its efficiency once steady state is reached and the time needed to reach steady state. So, for low loads, the system not only has lower maximum efficiency, but also requires a longer time to reach the maximum efficiency, causing a further penalization of the operation at partial load.

The purpose of this paragraph is thus to identify ways to reduce start-up time (time to reach steady state conditions and in particular nominal temperature) and improve the efficiency in the very first minutes after the system is switched on, and measure the gain deriving from such measures.
A way to reduce start-up duration and so to improve the net average efficiency during the first minutes of operation can be to avoid the refill of the oxygen-water separator tank during the warm-up which, as shown in Figure 4.1 in section 4.1.1, considerably slows down the achievement of the rated temperature and the warm-up duration. This can be achieved by setting the refill to start when the oxygen-water separator is emptier than 25% (setting used up to now). Refill can be delayed also by completely refilling the tank before the start-up (up to now it is 50% full at beginning of operation), but this strategy is excluded a priori, because this would lead to a slower warm-up (more water needs to be heated up).

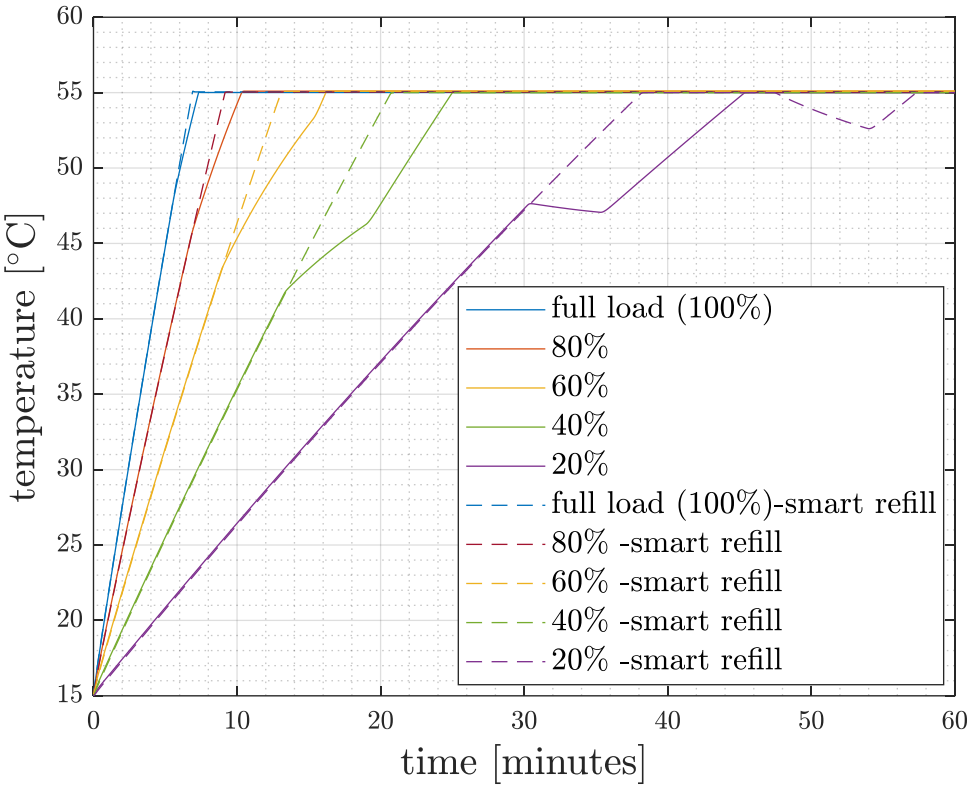

Figure 4.5 – Temperature evolution over time with smart refill (discontinuous line) or without (continuous line)

By setting a minimum water content of the 10% for the oxygen-water separator the refill of the oxygen-water separator starts after the temperature setpoint is reached for every load. This influences the warm-up time, especially at low loads, as it's possible to observe in Figure 4.5. Anyway, for very low loads (20%), the effect of the fresh water refill of the oxygen separator (minute 48') cannot be compensated by the heat generated by irreversibility, due to the too low current electrical power even if the coolant flow in the feed-in water heat exchanger is completely interrupted, and nominal temperature (55 °C) cannot be maintained until the refill starts, causing a

performance decrease after the warm-up is ended up. Such phenomenon is frequently observed in experiments and could be a first indicator of the inconvenience in starting the system at very low loads. In Table 4.3 it is possible to visualize the most significant parameters deriving from this simulation, time to start delivering hydrogen is not represented because it doesn't change with respect to previous case (Table 4.2).

Table 4.3 - Difference in time needed by the system to reach maximum efficiency, warm-up duration, maximum efficiency, maximum time to reach asymptotic cumulative efficiency and cumulative efficiency after one hour for the 5 loads considered and smart refills

Net load	**Reduction of warm-up duration**	**Warm-up duration**	**Max net efficiency**	**Time to reach asymptotic av. efficiency**	**Average efficiency after 1 hour**
100%	0' 25" (5.7%)	06' 55"	57.33%	16' 05"	56.56%
80%	1' 05" (10.5%)	09' 15"	57.58%	19' 45"	56.62%
60%	3' 10" (19.5%)	13' 05"	56.62%	27' 45"	55.31%
40%	4' 15" (17.0%)	20' 45"	52.12%	40' 10"	50.38%
20%	7' 25" (16.2%)	38' 20"	31.82%	> 60'	29.30%

Even though the warm-up time results to be sensibly reduced, especially at low loads, the benefits in terms of efficiency (thus, hydrogen produced) are quite low, with an increase in net average efficiency after one hour below 0.11% at any load. The cumulative efficiency plot is not reported as it is not possible to visibly appreciate a change from the previous case. This result is due to the fact that only the last minutes of the warm up are operated at higher temperature (i.e. higher efficiency), while during the most of the transient time the two cases present the same stack temperature (see Figure 4.5).

4.1.3 Hot stand-by

A more efficient way to reduce warm-up time and increase overall efficiency could be to keep the water in the oxygen-water separator tank, which is the tank that directly feeds the stack with water, at a certain temperature until the system is powered (hot stand-by).

Simulations are performed for all loads, simulating an initial water temperature in the oxygen-water separator equal to 30 °C and equal to 50 °C. Also these simulations are performed assuming the volume of water inside the tank at the beginning of the

simulation to be equal to half of the separator's volume. As it is possible to see in

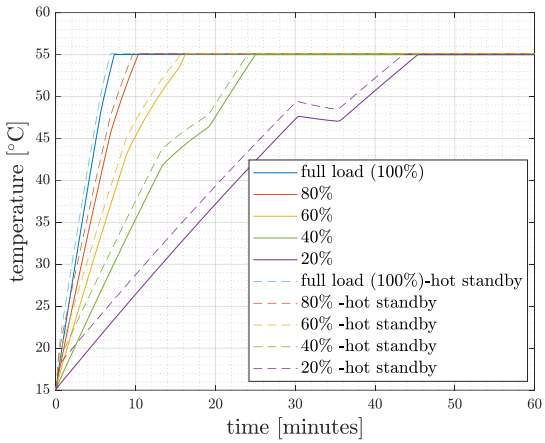

Figure 4.6 – Temperature evolution over time in base case and when adopting a hot standby at 50 °C (left graph) and 30 °C (right graph)

the temperature of the stack rapidly increases at the beginning of the warm-up until equilibrium between the oxygen separator and other components of the system is re-established, and it starts to evolve in parallel to the base case.

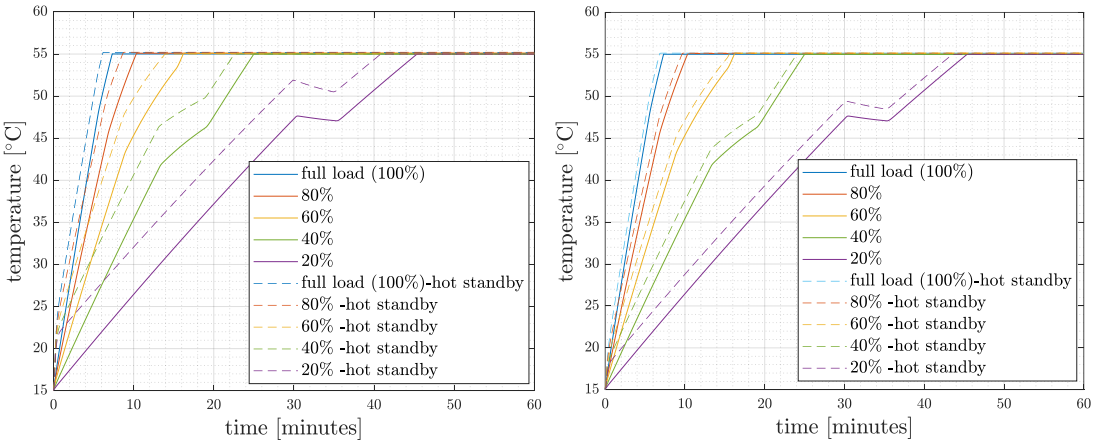

Figure 4.6 – Temperature evolution over time in base case and when adopting a hot standby at 50 °C (left graph) and 30 °C (right graph)

All the warm-ups result to be faster and the stack temperature (Table 4.4Table 4.5) is higher with respect to the base case for all the warm-up duration. Hence, the net average efficiency increases (approximately 1%$_{pt.}$ increase at the end of the warm-up for the 50 °C hot stan-by and approximately 0.5%$_{pt.}$ increase at the end of the warm-up for the 30 °C hot stan-by), as shown in Figure 4.7.

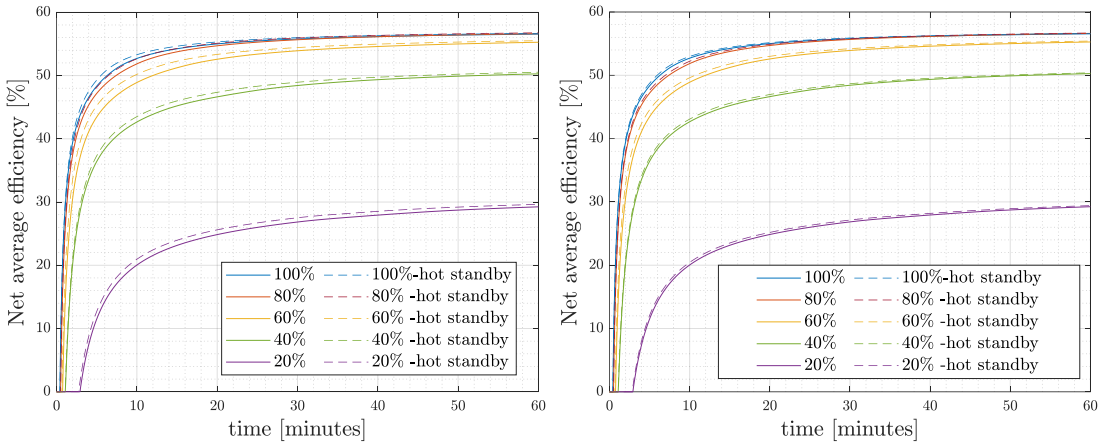

Figure 4.7 – Net average efficiency of the system over time without and with adoption of hot standby (30 °C right, 50 °C left)

However, the efficiency increase is still small with respect to what it could be achievable with a higher temperature increase with respect to the base case during the warm-up. In fact, the hot stand-by at 30 °C allows to reach only 3 °C of temperature increase in the first minutes of the warm-up with respect to the base case and the one at 50 °C only of 6 °C, while the maximum theoretical temperature increase is more or less of 30 °C (almost immediate achievement of the nominal temperature).

Table 4.4 – Difference in time needed by the system to reach maximum efficiency, warm-up duration, maximum efficiency, maximum time to reach asymptotic cumulative efficiency and cumulative efficiency after one hour for the 5 loads with 50 °C hot standby

Net load	Reduction in warmup duration	Warm-up duration	Max net efficiency	Time to reach asymptotic total efficiency	Total efficiency after 1 hour
100%	1’ 10” (15.2%)	06’ 10”	57.33%	14’ 05”	56.68 %
80%	1’ 35” (15.3%)	08’ 45”	57.58%	17’ 15”	56.76 %
60%	2’ 20” (16.8%)	13’ 55”	56.62%	23’ 10”	55.51 %
40%	2’ 25” (10.7%)	22’ 35”	52.12%	36’ 35”	50.53 %
20%	4’ 50” (11.8%)	40’ 55”	31.82%	> 60”	29.64 %

Table 4.5 – Difference in time needed by the system to reach maximum efficiency, warm-up duration, maximum efficiency, maximum time to reach asymptotic cumulative efficiency and cumulative efficiency after one hour for the 5 loads with 30 °C hot standby

Net load	Reduction in warm-up duration	Warm-up duration	Max net efficiency	Time to reach asymptotic total efficiency	Total efficiency after one hour
100%	0’ 25” (5.7%)	06’ 55”	57.33%	15’ 15”	56.62 %
80%	0’ 35” (5.6%)	09’ 45”	57.58%	18’ 45”	56.68 %
60%	0’ 35” (3.6%)	15’ 40”	56.62%	25’ 40”	55.41 %
40%	0’ 55” (3.7%)	24’ 05”	52.12%	39’ 50”	50.39 %
20%	2’ 10” (4.7%)	43’ 35”	31.82%	> 60”	29.41 %

Such a low impact of the oxygen tank heating up is due to the fact that the oxygen-water separator has a low thermal capacity due to the small amount of water that it contains (half of its volume in this case, namely around 8 l), amounting to around 33.5 kJ/kg that is about 5 times lower than stack thermal capacity (165 kJ/K). In fact, when stack and oxygen separator are reaching thermal equilibrium, due to the continuous recirculation of water, oxygen tank temperature decreases about 5 times more than the stack temperature increases, as Figure 4.8 shows.

Therefore, it is possible to increase the amount of heat released by the oxygen separator to the stack at system start-up by increasing the amount of water in the oxygen-water separator tank. In particular, by filling it completely and heating up the water when system is shut down, both the hot stand-by and a form of smart refill management are implemented. In fact, by filling completely the oxygen separator tank with water the tank cannot be emptied to 25% even at maximum power (i.e. maximum water consumption), during the warm-up, and no refill starts.

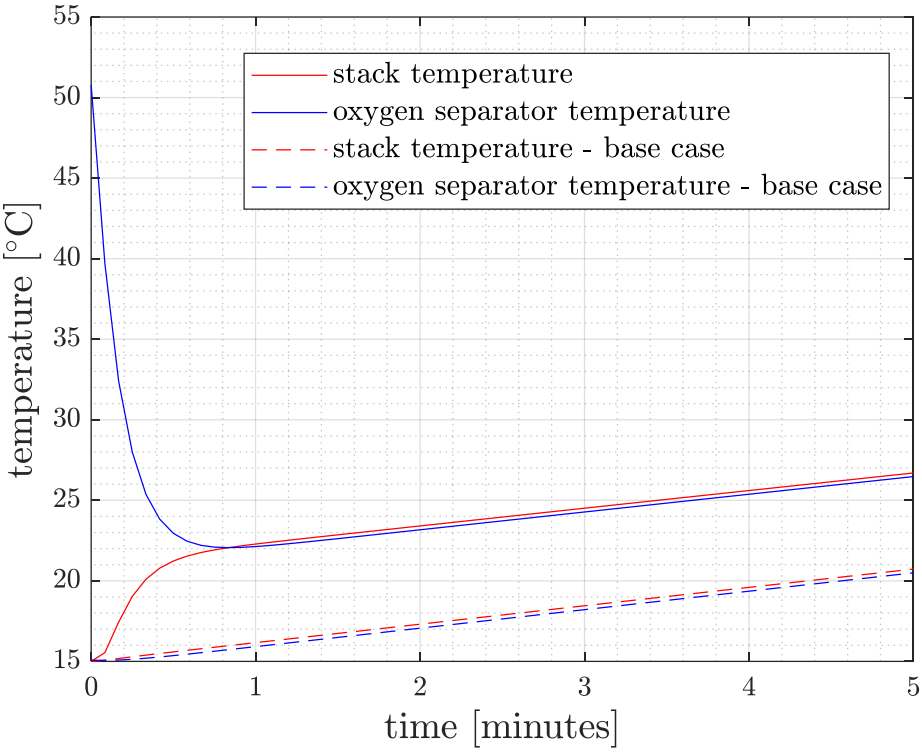

Figure 4.8 - Oxygen-water separator and stack temperatures over time in case of 50 °C hot stand-by and 20% load and base case

The hot stand-by is performed at 50 °C as the efficiency increase at 30 °C is considered to be too low (0.5 $\%_{pt.}$). The temperature increase of the stack while reaching thermal equilibrium with the oxygen-water separator at 20% of the load is represented in Figure 4.9, while in Table 4.6 the main numerical results of the 5 simulations at the 5 different loads are reported.

Table 4.6 – Main simulation results for the 5 loads with 50 °C hot standby and full of water oxygen separator

Net load	**Reduction in warm-up duration**	**Warm-up duration**	**Max net efficiency**	**Time to reach asymptotic av. efficiency**	**Total efficiency after 1 hour**
100%	1’10”(15.9%)	06’ 10”	57.33%	13’ 40”	56.69%
80%	2’05” (20.2%)	08’ 15”	57.58%	16’ 15”	56.90%
60%	4’20” (26.7%)	11’ 55”	56.62%	22’ 00”	55.58%
40%	7’00” (28.0%)	19’ 00”	52.12%	34’ 05”	50.65%
20%	10’55” (24%)	34’ 50”	31.82%	>60’	29.72%

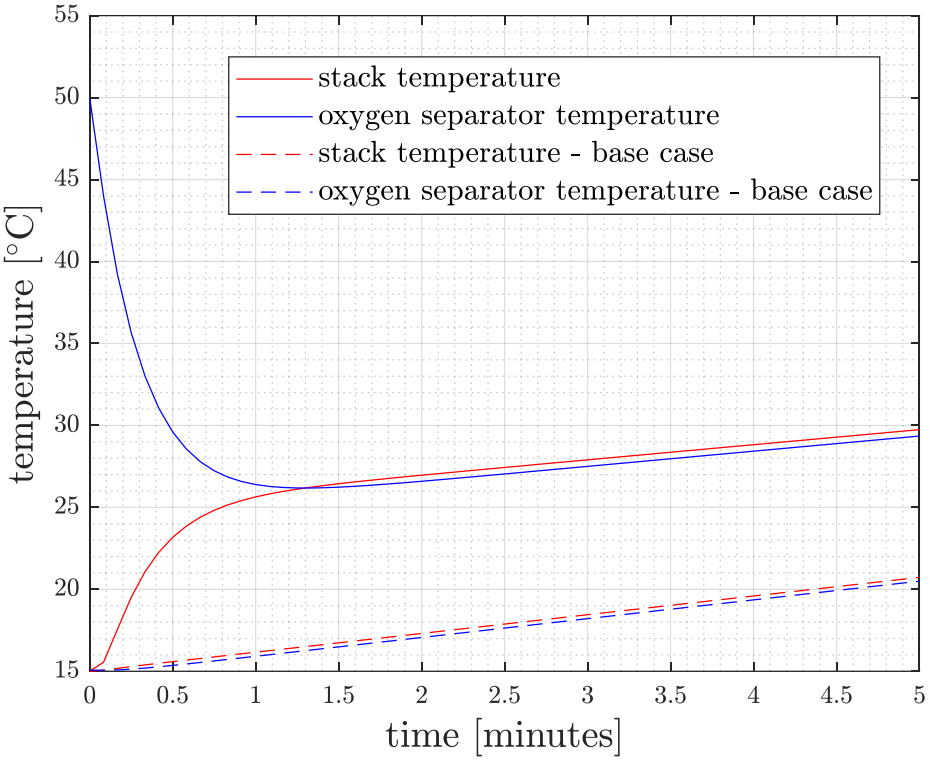

Figure 4.9 - Oxygen-water separator and stack temperatures over time in case of 50 °C hot stand-by and 20% load

The temperature profiles over time show the absence of refill during stack warm-up but, as in previous case, the 20% load temperature profile evidences, at the last minutes of simulation, problems in keeping the temperature to the rated one (55°C), as shown in Figure 4.10. In general, temperature increase is higher with respect to a hot standby with half-full of water oxygen tank.

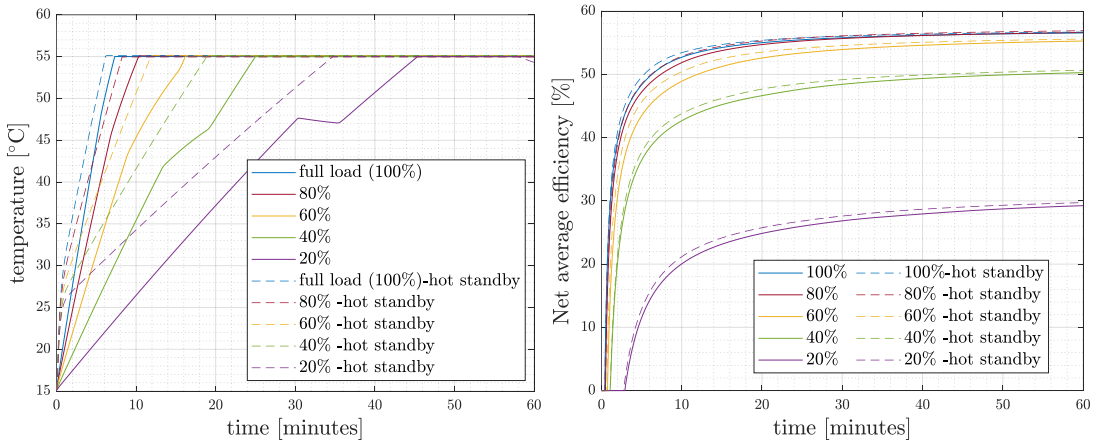

Figure 4.10 – Left chart: Stack temperature over time with hot standby at 50°C and full oxygen separator (dashed line) compared to base case (continuous). Right chart: Net average efficiency over time without and with the adoption of hot standby (50 °C and full oxygen separator)

The temperature increase during warm-up is automatically translated into an efficiency increase. The average efficiency increase at the end of each warm-up is around 2 $\%_{pt.}$ (Figure 4.10).
In order to evaluate when hot standby is convenient and weather not the increase in hydrogen produced with respect to the base case is computed. In fact, in order to reach/keep the 50 °C of water temperature inside the oxygen separator, a certain amount of energy must be spent. In the following analysis the hydrogen surplus produced thanks to the hot standby is compared with the amount of hydrogen that can be produced with the energy consumed to implement a 50 °C hot stand-by. In order to evaluate the energy consumed for hot standby, the heat flux needed by the oxygen-water separator to reach or keep the 50 °C is assumed to be provided by an electric resistance dissipating all the electric energy into heat via Joule effect. Heat losses from the oxygen separator to the environment are modelled as in section 2.3.
Two scenarios are considered; in the first scenario when the system is switched off the oxygen tank is completely filled with water from the deionized water tank (assumed to be at least at 50 °C) and the electric resistance keeps the oxygen-water separator temperature at 50°C for a certain amount of hours (6 – 9 – 12). The power consumed by the electric resistance is set to be equal to 32 W_{el}. The comparison is performed evaluating an 'equivalent hydrogen' amount, equal to the hydrogen that would be produced by a certain amount of electrical energy, considering it to be produced with the maximum efficiency for each load. As it's possible to see in Table 4.7, it is almost never convenient to keep the oxygen-water separator in hot stand-by, unless the tank is thermally insulated in order to reduce the amount of electrical energy needed to keep the water inside the tank at 50 °C.

Table 4.7 – Hydrogen production increase and equivalent hydrogen spent for hot standby at different loads

Net load	**Hydrogen production increase**	**Equivalent hydrogen spent for the hot stand-by**		
		(6 h)	**(9 h)**	**(12 h)**
	[kg]*10^{-4}	[kg]*10^{-4}	[kg]*10^{-4}	[kg]*10^{-4}
100%	19 (+2.3%)	26 (655 kJ_{el})	40 (1000 kJ_{el})	54 (1346 kJ_{el})
80%	21 (+2.4%)	26	40	54
60%	30 (+3.2%)	26	40	54
40%	24 (+2.5%)	24	36	49
20%	15 (+3.0%)	14	22	30

In the second scenario the system is cold and the electric resistance heats up the oxygen separator exactly before the system starts operating (pre-heating), in order to reach 50 °C when the system starts operating, starting from an initial temperature of the oxygen separator equal to the ambient temperature (15 °C). It is evident that using energy from the grid for such operation would never be convenient, since warming-up 16 liters of water requires about 2500 kJ, equivalent to 53*10^{-4} kg of hydrogen produced with an efficiency (HHV based) of 30%, a value one order of amplitude bigger than any gain

reachable thanks to the hot standby itself. Thus, it is possible to conclude that in case of intermittent power sources it is convenient to insulate the oxygen-water separator and implement hot stand-by using a small electrical resistance, allowing to reach, for very short runs, an increase in the amount of hydrogen produced up to 3%.
Operating a pre-heating of the system starting from the cold system, is instead only convenient when it is available a free energy source, for instance when the electricity used to heat up the oxygen separator is too low to make the system run (e.g. lower than 15% of nominal power, i.e. 9 kW_{el}). A possible application of this strategy could be when coupling the electrolyzer with a solar photovoltaic power source. At the beginning of the daylight, the power produced is too low to make the system work (the value of the minimum power to make the system work is ~9 kW), but it's enough to provide sufficient electricity to heat up the water in the oxygen-water separator, in this way acting an extremely cheap energy storage in the form of low temperature heat accumulated in the oxygen-water separator. By coupling the system to a typical solar photovoltaic load at start-up (data are presented in section 3.1.2) and injecting into an electrical resistance the power produced by the photovoltaic plant in the first hour of operation (which is not sufficient to run the complete system) water temperature inside the oxygen-water separator can be heated up above the rated temperature of 55 °C. In the example represented in Figure 4.11 it is shown the power profile coming from a photovoltaic plant with a 1:1 power ratio with the electrolyzer in the early morning (namely, the peak power of the PV plant is 62 kW). This power is never sufficient to start the electrolyzer (< 15%) in the first hour of operation thus, in Figure 4.11 the power profile is matched to that of the water temperature in the oxygen – water separator resulting from the simulation, assuming this power to be used to heat a resistance placed inside the separator.

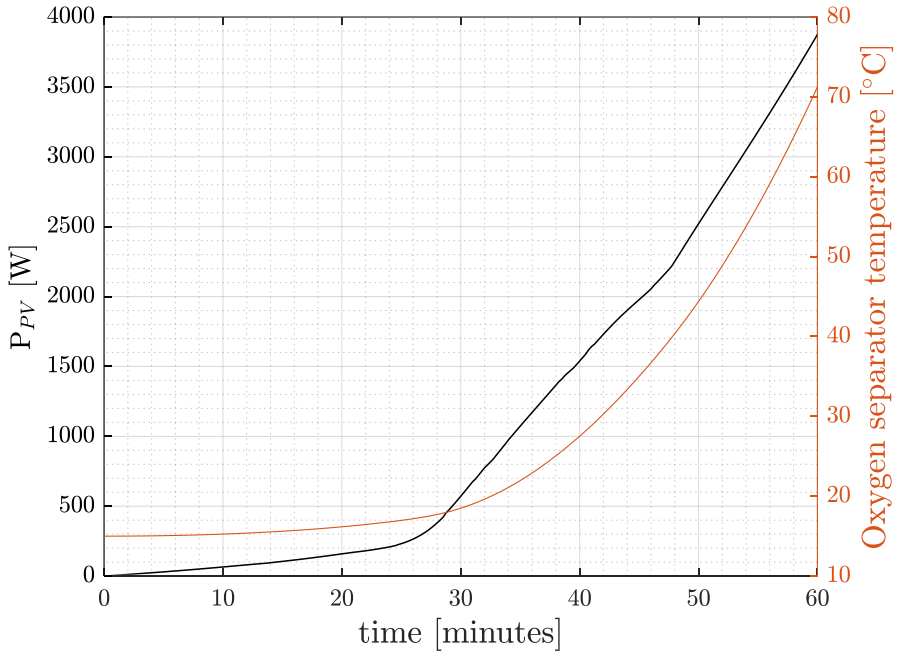

Figure 4.11 – Photovoltaic power and water temperature in the oxygen tank over time

Typically, electrolyzers are coupled to solar photovoltaic with a lower power ratio. The same simulation of Figure 4.11 is run but with a 1:3 power ratio between the electrolyzer nominal power and the PV peak power, so, figuring to have three power sources identical to the one in Figure 4.11. The first hour of operation is simulated with and without the resistance inside the oxygen – water separator, and results are illustrated in Figure 4.12.

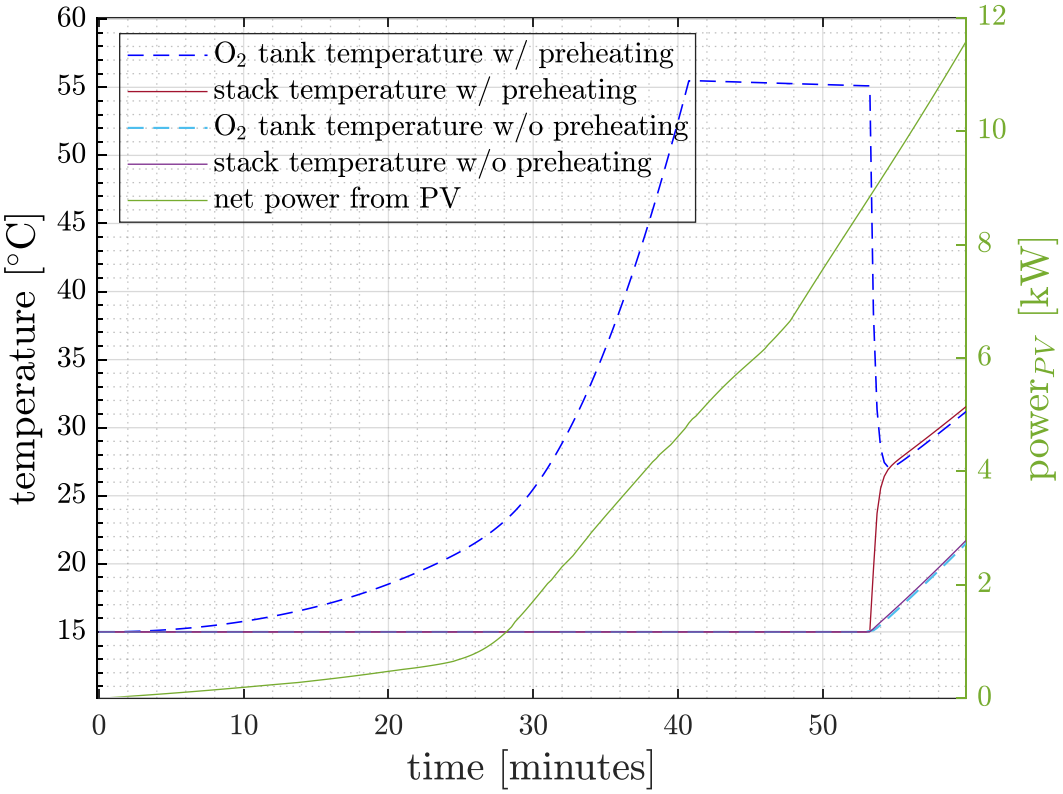

Figure 4.12 - Oxygen-water separator and stack temperature with and without preheating in the case of solar photovoltaic coupling

The system starts producing a positive net amount of hydrogen from 15% load, so in the case without preheating the energy from the first 50 minutes of operation is lost, while in the second case most of it is used to heat up the water inside the oxygen-water separator to 55 °C by means of a resistance. When the power from the photovoltaic is sufficient to run the system, in the case with pre-heating the stack temperature increases rapidly thanks to the water pre-heating in the oxygen water separator. This allows the system to reach the rated temperature more rapidly and to operate with a higher net efficiency, partly recovering the power from the photovoltaic not exploitable for direct hydrogen production.
Depending on the load and system characteristics, it is potentially possible to operate the system at maximum efficiency since the beginning of operation, by using the power from the renewable source either to pre-heat the water with an electrical resistance and to pre-heat the stack, activating the circulation pump in order to allow the water in the oxygen-water separator to exchange heat with the stack. In this last

case, the warm-up time reduces to zero, leading to the hydrogen production increase presented in Table 4.8.

Table 4.8 – Maximum gain in hydrogen production achievable with a complete stack preheating at 55 °C with respect to base case (T_{amb} = 15°C)

Net load	**Hydrogen production increase**	**Cumulative hydrogen production at the end of base case warm-up time**		**Warm-up time**	
				Base case	Stack preheating
	$*10^{-3}$ [kg]	base case $*10^{-3}$ [kg]	stack preheating $*10^{-3}$ [kg]		
100%	12.2 (+12.5%)	97.9	110.1	07’ 20”	00’ 00”
80%	12.1 (+10.8%)	112.6	124.7	10’ 20”	00’ 00”
60%	12.8 (+9.7%)	131.8	144.6	16’ 15”	00’ 00”
40%	11.6 (+9.3%)	124.9	136.5	25’ 00”	00’ 00”
20%	8.8 (+12.9%)	68.1	76.9	45’ 45”	00’ 00”

The high value of the relative increase in the hydrogen production at 20% of the full load is due to the fact that the absolute increase in the hydrogen production is not only proportional to the power, but also to the transient duration. These two effects act in opposite direction and therefore the relative increase of production has a point of inflection in correspondence of a load of about the 50%.

4.2 Part-load optimization

As already presented in paragraph 3.4.2, the system net efficiency at part-load drops dramatically (namely, the system specific consumption increases dramatically). In the same paragraph it’s shown that this efficiency drop is mainly due to hydrogen losses, which do not depend on the load and consequently have a much higher weight at low loads. Hydrogen losses are mainly attributable to the dryer adsorption beds regeneration and switching. This is a primary issue, considering the interest in coupling PEM electrolyzers with renewable power sources, which are fluctuating. Thus, this section deals with the strategies that can be implemented in order to decrease hydrogen losses, hence increasing the net efficiency of the system, especially at part-load.

4.2.1 Flexible adsorption beds regeneration

The main source of hydrogen loss is due to the PSA bed regeneration. The drying unit of the electrolyzer contains a batch system composed of two adsorption beds which

work alternatively; when the first bed is adsorbing water the second one is regenerated. Regeneration mainly consists in three phases: depressurization, purging and repressurization. Purging consists in the final desorption of the entrained moisture and is carried out at the lowest pressure of the bed, by means of a high purity stream of hydrogen coming from the active adsorption bed. The hydrogen stream is continuous and orifice driven (i.e. dependent only on pressure), nominally rated at 0.0744 kg_{H2}/h at 30 bar_g.

From the experimental data (section 3.1) it is possible to deduce that every 18 minutes there is a switching of active adsorption bed, independently from the load. Being the concentration of water contained in the wet hydrogen stream before the dryer only dependent on temperature and pressure (paragraph 2.2) it is independent from the load once steady state is reached. It is thus possible to compute the amount of water adsorbed by the bed which is only dependent on the wet hydrogen mass flow rated, which, in turn, depends on the useful current.
The idea is to keep switching the active bed every 18 minutes but dosing the hydrogen purge stream on the basis of the amount of water entrained in the saturated bed, which can be estimated by knowing the current entering the stack in the 18 minutes during which the bed was active, by closing a valve placed upstream the orifice.
Assuming the quantity of dried hydrogen necessary to regenerate a completely saturated adsorber as:

$$M_{H_2 loss}^{max} = \dot{m}_{orifice} \cdot t_{reg} \tag{4.2}$$

where $\dot{m}_{orifice}$ is the rated mass flow rate of pure hydrogen stream passing through the orifice (0.0744 kg_{H2}/h) and t_{reg} is the time between 2 regenerations (0.3 h) it is possible to determine the amount of pure hydrogen that must pass through the orifice when the system is not working at full load and therefore also for how long the valve placed upstream of the orifice must remain open. In fact, in the hypothesis of unitary Faradaic efficiency (conservative assumption) the amount of hydrogen produced by the electrolyzer is linearly proportional to the current, as modeled by the Faraday's law. This strategy allows to save a great amount of hydrogen when the system is operating at very low loads, since in 18 minutes and 50% of the nominal power the adsorber gets only half saturated and only 9 minutes are sufficient to completely regenerate the bed, saving the 50% of hydrogen loss due to dryer beds regeneration.

The system specific consumption implementing such strategy is compared to the original one in Figure 4.13. The system consumption strongly reduces at part load, up to 38 % reduction at 0.4 A/cm^2 of current density, i.e. ~20 % load (lower loads are not taken into account since no experimental data were available below 0.4 A/cm^2 and therefore that part of the curve is not properly validated). It is interesting to notice that the best efficiency point moves towards lower loads, around 1.2 A/cm^2 (~60 % of the nominal power vs. ~80 %). The disadvantage of such strategy is the need to install two new valves, in order to have a valve upstream of the orifice when any of the two beds

is in regeneration mode. Clearly, system specific consumption at full load doesn't change, since the purge stream sizing is based on full load data.

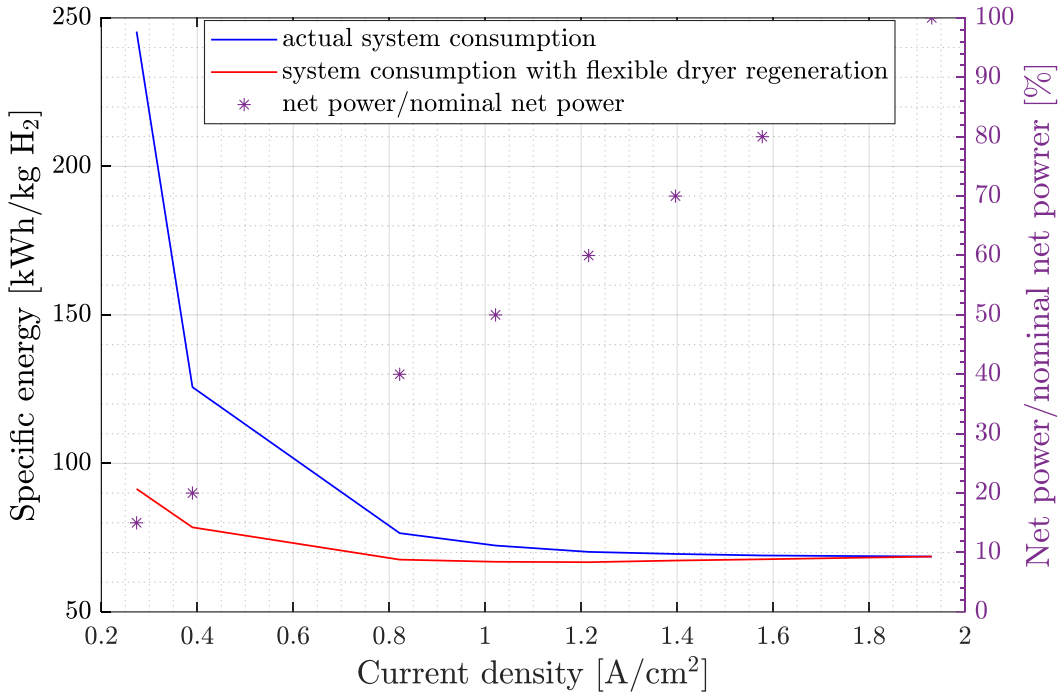

Figure 4.13 – Actual system specific consumption and system consumption implementing flexible regeneration

4.2.2 Flexible switching of active adsorption bed

Another measure that can be applied in order to reduce the hydrogen loss at part load is to increase the time between two regenerations instead of adopting a fixed time window. In fact, how explained in section 2.5, every time the active bed is switched into regeneration mode the hydrogen contained in it gets lost due to depressurization. This operation is currently done at regular intervals, every 18 minutes, but if the system is run at lower loads with respect to the nominal one, the amount of water entrained in the bed results to be less than the saturation value, de facto putting into regeneration mode the bed before it's needed, causing a useless loss of pure hydrogen. Assuming the maximum amount of water a single adsorber can soak up as:

$$M^{max}_{adsorbed H_2O} = \dot{m}^{full\ load}_{out,H_2 separator} \cdot t_{reg} \cdot x_{H_2O} \tag{4.3}$$

where $\dot{m}^{full\ load}_{out,H_2 separator}$ is the wet hydrogen mass flow rate coming out of the hydrogen-water separator when the system operates at full load and y_{H_2O} is the mass

fraction of water in it, it is possible to determine the time the active adsorber can be used without the need of regeneration at part load:

$$\frac{M_{adsorbed H_2O}^{max}}{\dot{m}_{out,H_2 separator}^{part\ load} \cdot x_{H_2O}} = t_{reg} \tag{4.4}$$

Eq. (4.4) considers, of course, constant power and steady state, for representation purposes, but by integrating the mass flow rate coming out of the hydrogen-water separator multiplied by the fraction of water, the control system can estimate the amount of water adsorbed by the adsorption bed and decide when it needs to be put into regeneration mode. As in the previous chapter, the mass flow rate doesn't need to be measured, but it's sufficient to record the current density, directly proportional to the mass flow rate exiting the stack, since the hydrogen is assumed to be saturated of water.
This allows to spread the hydrogen loss on wider time windows, reducing its impact on the global operation.

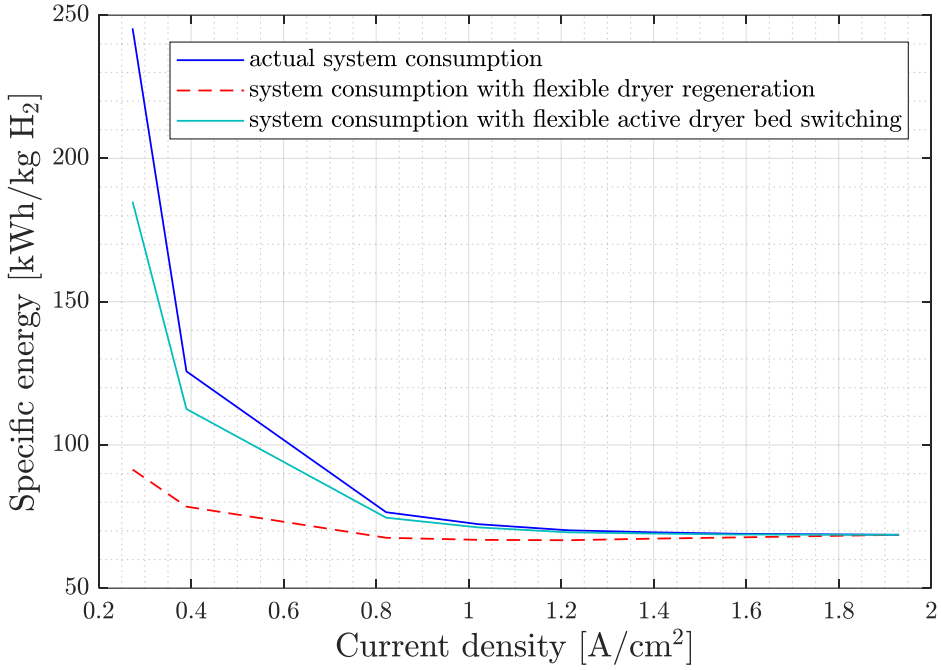

Figure 4.14 – Actual system consumption and system consumption when adopting flexible regeneration and flexible switching

As shown in Figure 4.14, such strategy can bring a sensible reduction in system consumption, but not as much as when adopting flexible regeneration (10% reduction in consumption vs. 38% at 0.4 A/cm^2). The advantage of this strategy is that it doesn't require any physical change to the system, but only a different setting of the control system.
By implementing both flexible switching and flexible regeneration it is possible to furtherly reduce the system consumption only if the purging of the regenerating bed

finishes before the active bed is saturated. In fact, in this case it is possible to close the valve upstream the orifice and continue to use the already active adsorber. On the contrary, if the active bed needs to be regenerated before the regenerating bed is completely regenerated the hydrogen stream purity would drop, causing the loss of that hydrogen, which needs to be vented. Thus, when designing this kind of systems it is of primary importance to ensure that the orifice slipstream is sufficient to completely regenerate a saturated bed even if the active bed is saturated in the shortest time possible. Anyway, in the case of study 18 minutes are sufficient to completely regenerate the saturated bed and the minimum time of use of the active bed is equal or higher than 18, thus this problem does not exist.
The system consumption resulting from the coexistence of both strategies is shown in Figure 4.15.

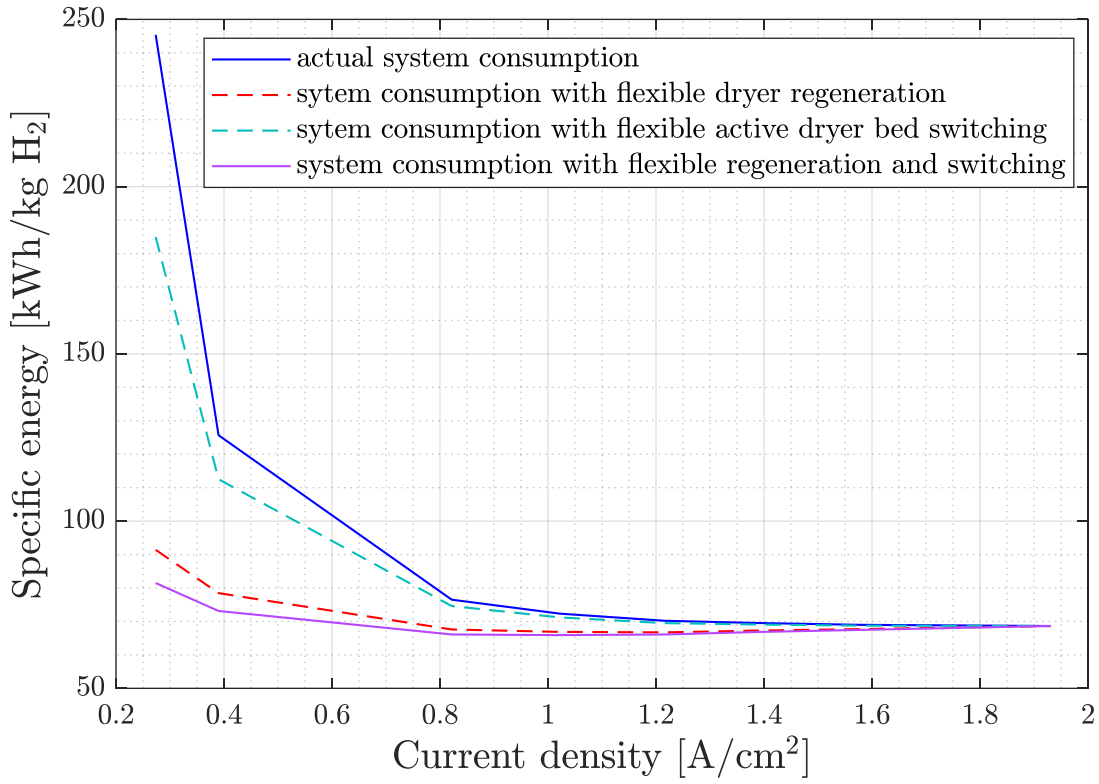

Figure 4.15 - Actual system consumption and system consumption when adopting flexible regeneration, flexible switching and both

The system consumption can be reduced up to 42% at 0.4 A/cm^2 (~20% load). The numerical results of the system consumption in the analyzed cases are shown in Table 4.9.

Table 4.9 – Specific energy consumption of the system in base case and adopting different drying unit management

	System consumption [kWh/kg H_2]			
Net load	**Actual**	**Flexible regeneration**	**Flexible switching**	**Flexible regeneration and switching**
15%	245.4	91.4	184.9	81.5
20%	125.7	78.5	112.5	73.1
40%	76.5	67.6	74.6	66.1
50%	72.3	66.9	71.2	65.9
60%	70.2	66.7	69.5	66.1
70%	69.5	67.3	69.1	66.9
80%	69.0	67.7	68.7	67.5
100%	68.6	68.6	68.6	68.6

Better results can be obtained only substituting the 2-beds drying unit with a 4-beds or more drying unit (see section 2.5). Assuming an ideal drying process involving zero hydrogen losses (not realistic), the system consumption reduces by 55% at ~20% load with respect to base case, 13%$_{pt.}$ less than the case with flexible switching and regeneration, while the system consumption at full load is reduced by 12%, as shown in Figure 4.16:

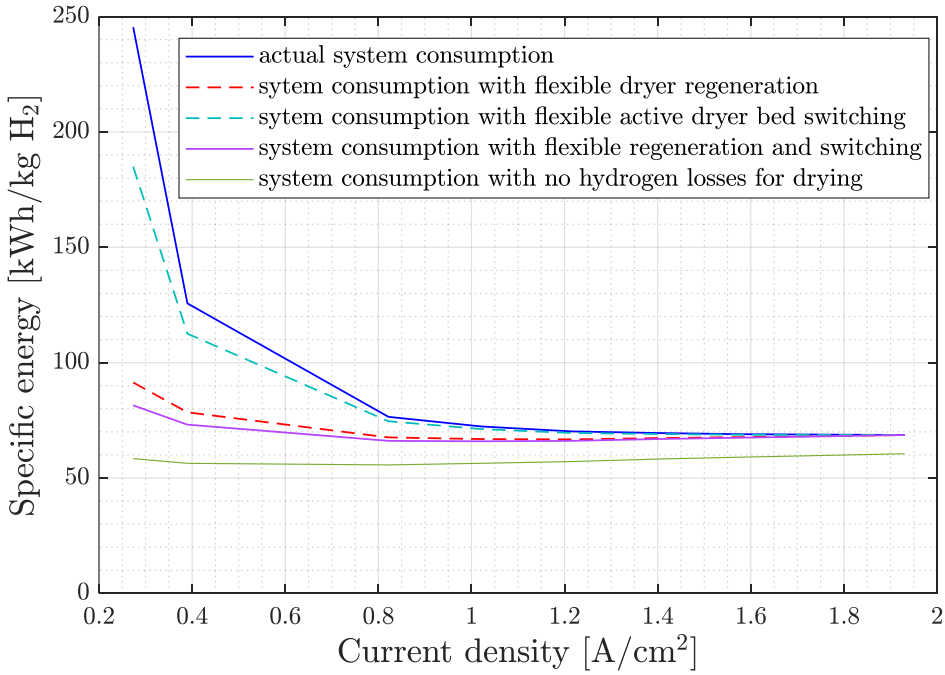

Figure 4.16 – Actual system consumption and system consumption when adopting flexible regeneration, flexible switching and both, compared to the case with no drying-related hydrogen losses

Therefore, it is possible to state that without heavy modifications of the system, hydrogen losses can be reduced up to reaching the 76% of the maximum efficiency improvement achievable at minimum load by acting on the PSA system. On the other hand, for higher loads implementing a flexible regeneration or switching can't bring to any improvement in system efficiency, since the amount of moisture the PSA has to remove reaches its maximum and active bed switching and purge flows need to be consequently maximized.

4.2.3 Auxiliaries optimization

As already discusses in section 3.4.2, auxiliaries consumption is the second cause of net efficiency reduction of the system at partial load since their consumption is approximately independent from the power at which the system is operating. In particular, the feed-in water pump (centrifugal pump) accounts for the 80% of the auxiliaries consumption (~2 kW over 2.5 kW), in order to provide a continuous flow rate of liquid water to the stack of 0.63 l/s. At nominal conditions water utilization factor is 0.4%, with a mass fraction of oxygen in the water exiting the anode equal to 0.35%. By introducing the use of a variable speed circulation pump it is possible to variate the mass flow rate of water entering the stack anode, hence reducing the consumption due to balance of plant at part load and keeping, at the same time, reduced values of the water utilization factor and of oxygen concentration in the water exiting the anode. In fact, a too high concentration of oxygen at the anode would generate oxygen bubbles, increasing concentration losses (see section 2.2). The system is simulated, as always, starting from power-off condition and in equilibrium with the ambient (ambient temperature equal to 15 °C), imposing a constant power input.
As the stack warms up the and voltage decreases, current density increases, increasing the amount of hydrogen and oxygen generated and consequently the oxygen concentration at the anode. Thus, maximum oxygen concentration at the anode is found at maximum temperature as shown in the example in Figure 4.17 where the oxygen mass fraction in recirculating water is computed over time:

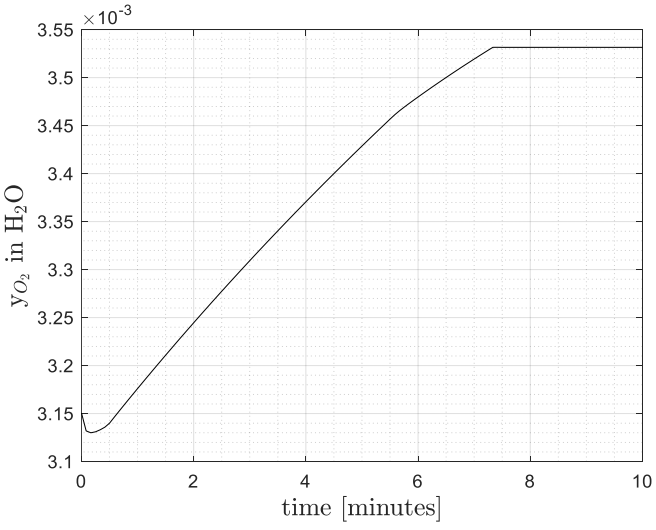

Figure 4.17 - Oxygen mass fraction in recirculating water over time at nominal power

Thus, the maximum oxygen concentration is obtained once steady state is reached. Anyway, it is important to verify if a fast reduction in the load, leading to a fast reduction in the pump speed might lead to some peaks in the oxygen concentration or water utilization. Thus, the system is simulated varying dynamically the load once steady state is reached, from 100% to 50% and from 100% to 20% in one minute, while the pump speed is continuously adjusted in order to vary the circulation water flow rate according to the current. The system has no issue in keeping the rated pressure and temperature when the load drops to 50%, while some problems may arise when the load drops to 20%, but only when the water refill of the oxygen-water separator is occurring (Figure 4.18).

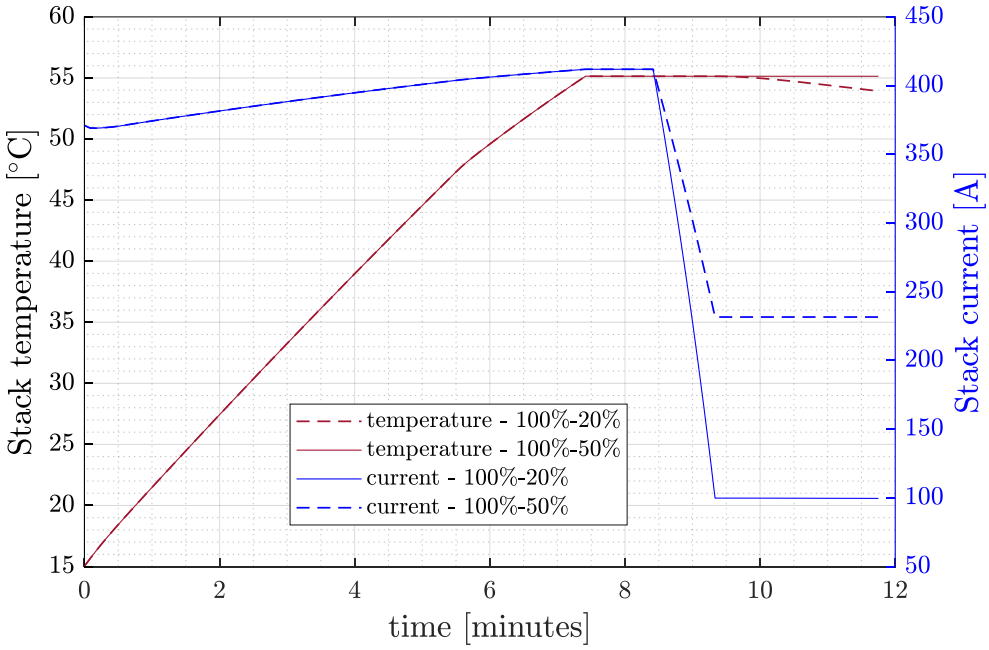

Figure 4.18 - Stack current and temperature over time

The oxygen concentration at the anode never exceeds the rated value of ~0.35%, and so does the water utilization, which never exceeds 0.4%, as shown in Figure 4.19.

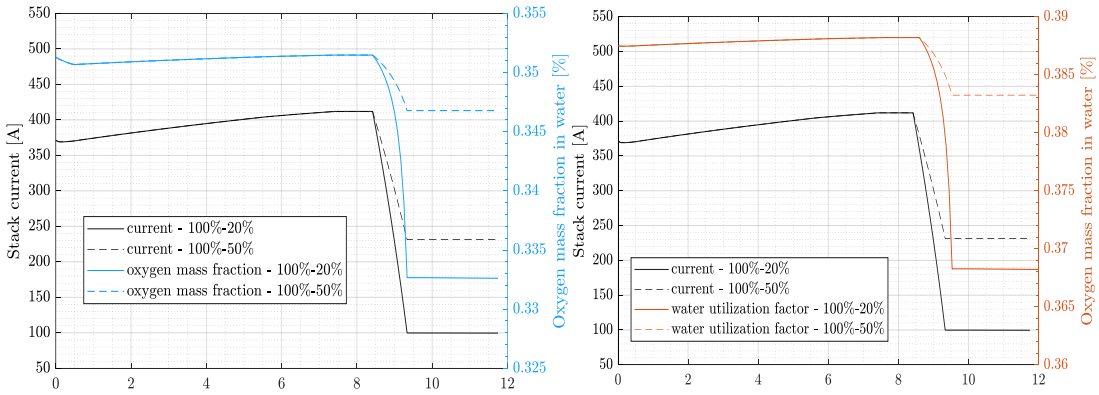

Figure 4.19 – Stack current and oxygen mass fraction in water at anode over time (left chart) and stack current and water utilization factor over time (right chart)

Verified that with this approach the dynamic variation of the load doesn't generate any increase in the oxygen concentration at the anode, it is possible to simulate every load and compute the new specific energy consumed for producing hydrogen. The system consumption once introducing a variable speed circulation pump is shown in Figure 4.20, allowing to reduce specific consumption at part load (20% and approximately 0.4 A/cm^2 of current density) by a 28%.

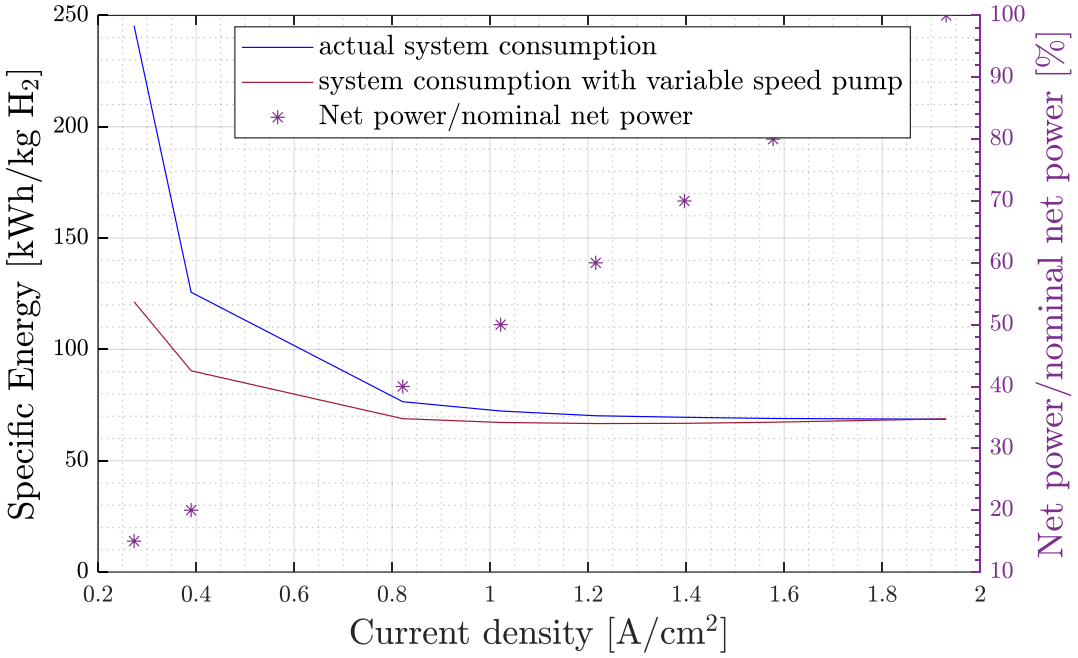

Figure 4.20 – Actual system consumption and system consumption with a variable speed circulation pump

4.3 High pressure operation

As introduced in section 1.4.2, it might be of interest to produce hydrogen at a pressure higher than the rated 30 bar$_g$ of the electrolyzer. This could be either for storage reasons, or for pipeline injection or similar. Thus, the purpose of this section is to investigate whether it is more convenient to use a compressor or produce hydrogen already compressed at the output of the electrolyzer. The analysis is purely on an energy point of view, but it is in the hope of the writer, that those who read can find useful information on the new consumption and on the changes to be made on the system so that those who are competent can quickly translate them into assessments of an economic nature. Three different pressures of the hydrogen are considered for the analysis, from a 70 bar$_g$ value, typical of natural gas pipelines, up to a 210 bar$_g$, typical of storage.

4.3.1 High pressure electrolysis

One of the main issues of high pressure electrolyzers is the hydrogen crossover through the membrane, which leads to a Faradaic efficiency reduction. This topic is treated in section 3.4.2, where a simplified method for the computation of the Faradaic efficiency is implemented. Anyway, at full load the Faradaic efficiency is so high that its variation at full load is neglected in this first analysis. The value of the hydrogen purge flow for dryer's adsorption beds regeneration is blocked to the rated value at 30 bar_g during simulations. In fact, it would make no sense to run the actual system at such pressures without changing the orifice characteristics, since hydrogen losses would dramatically increase pointlessly. The values of the system specific consumption and chiller energy consumption increase compared to the base case are reported in Table 4.10, computed assuming a constant COP of the chiller equal to 3 and a constant Faradaic efficiency.

Table 4.10 – System specific consumption and hydrogen production resulting from simulations at nominal net load (62 kW) and different cathode pressures

Hydrogen pressure	**System specific consumption**	**Chiller heat duty**	**Chiller consumption**	**Hydrogen net production**
[bar_g]	[kWh/kg H_2]	[kW_{th}]	[kW_{el}]	[kg/s]
30 (base case)	68.7	15.48	5.161	$2.505*10^{-4}$
70	69.1 (+0.6%)	15.72(+1.6%)	5.239	$2.492*10^{-4}$
140	69.4 (+1.0%)	15.84(+2.3%)	5.281	$2.481*10^{-4}$
210	69.6 (+2.3%)	15.91(+2.8%)	5.302	$2.475*10^{-4}$

4.3.2 Hydrogen post-compression

A high pressure of hydrogen can also be obtained by compressing it by means of a compressor. In this case, the hydrogen is considered to be produced at 30 bar_g and sent to a multi-stage intercooled compressor that compresses it to the desired pressure. The electrical power required for the compression is computed assuming a polytropic process, with a polytropic efficiency $\eta_{p,c}$ constant and equal to 75%:

$$P_{c,el} = \frac{\dot{m}_{H_2} c_{p,H_2} T_{H_2,in} \left(\beta_{stage}^{\frac{\gamma-1}{\gamma \cdot \eta_{p,c}}} - 1 \right)}{\eta_{el} \cdot \eta_{mec}}$$

where $\gamma = c_{p,H_2}/c_{V,H_2}$, β_{stage} is the compression ratio of a single stage of the compressor and η_{el} and η_{mec} are the electrical and mechanical efficiencies, equal to 0.99 and 0.98 respectively. For the case with compression to 70 bar_g the compressor is assumed to be a single stage compressor, for the case with compression to 140 bar_g a two stage compressor is used, while for the case with compression to 210 bar_g the compressor is a three stage compressor. In any of this cases a refrigeration of the

hydrogen gas to 25 °C after each compression stage is assumed to be required. Each compression stage is assumed to have the same compression ratio, computed as:

$$\beta_{stage} = \beta_c^{\frac{1}{N_{stages}}}$$

where β_c is the total compression ratio of the compression process. Thus, the maximum temperature the hydrogen reaches in the first compressor (compression up to 70 bar_g) is equal to 135 °C, in the second (compression up to 140 bar_g) to 124 °C and in the third (compression up to 70 bar_g) to 114 °C. Refrigeration is assumed to be carried out by a cooler with a COP of 3. Eventually, it is possible to compute the system specific energy consumption for producing hydrogen at different pressures (Table 4.11).

Table 4.11 – Compressor and overall (electrolyzer + compressor) system consumption at different hydrogen pressures using a compressor

Hydrogen pressure	Compressor consumption	Pressure ratio	Chiller heat duty	Chiller consumption	H_2 net production
[bar_g]	[kW_{el}]	[-]	[kW_{th}]	[kW_{el}]	[kg/s]
30 (base case)	-	-	15.48	5.161	$2.505*10^{-4}$
70	0.409	2.3	15.87	5.290	$2.505*10^{-4}$
140	0.737	2.1	16.19	5.397	$2.505*10^{-4}$
210	0.911	1.9	16.36	5.453	$2.505*10^{-4}$

4.3.3 Final comparison and conclusion

The overall system consumption for producing hydrogen at different pressures resulting from the two cases analyzed at full load, namely producing hydrogen at high pressure directly in the electrolyzer (High Pressure Electrolysis – HPE) or producing it at 30 bar_g and then post-compressing it (compressor consumption is included) are shown in Figure 4.21. High pressure electrolysis consumption is shown both keeping a constant Faradaic efficiency (blue, continuous line) and assuming a variable Faradaic efficiency (blue, dashed lines). The two cases with variable efficiency are subject to a Faradaic efficiency loss of 0.5%$_{pt.}$ every 70 bar (case 1) and of 1%$_{pt.}$ every 70 bar (case 2) at nominal current density. These values are considered to be realistic by observing experimental data on the effect of hydrogen partial pressure on hydrogen cross permeation rate in Nafion-117 membranes [62]. It is important to stress that too high hydrogen permeation rates would lead to safety issues due to a too high hydrogen content in oxygen. Anyway, this is an early analysis that neglects this aspect and just

aims at a first raw evaluation of system performances on an energy perspective. The base case (30 bar_g) is obviously not subject to changes in the Faradaic efficiency.

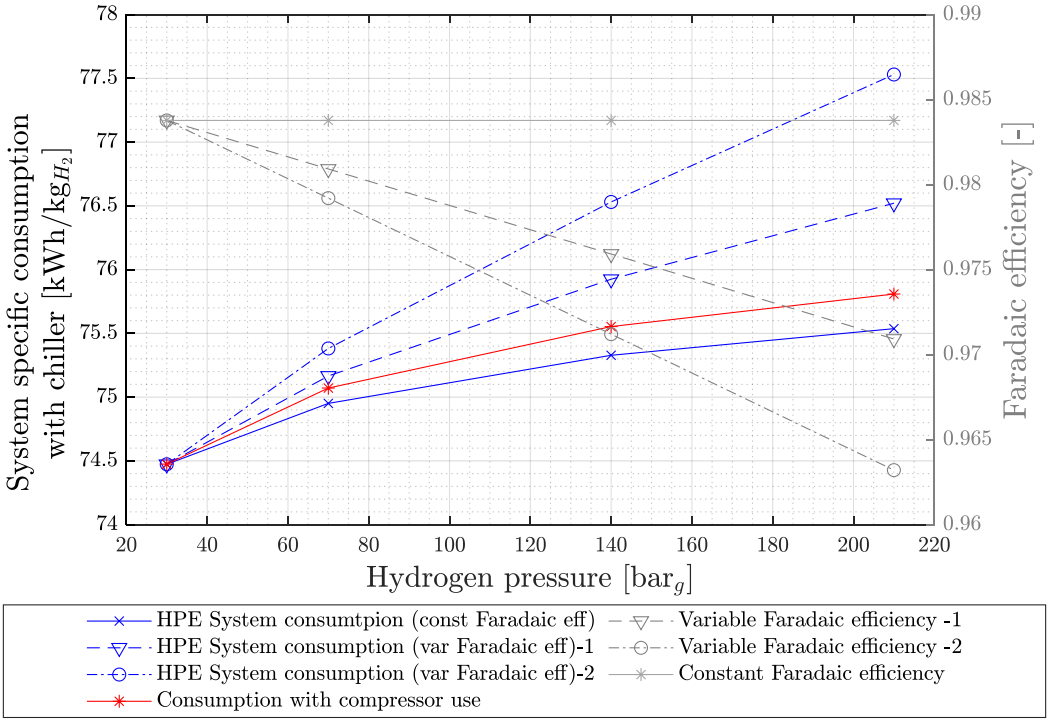

Figure 4.21 – Overall system consumption (y-axis) for producing hydrogen at different pressures (x-axis) adopting a post-compression or producing pressurized hydrogen inside the electrolyzer at full load

It is possible to conclude that high pressure electrolysis should certainly be investigated as an alternative to the use of compressors for the production of hydrogen at high pressures, since it may result convenient on a specific energy consumption point of view. In any case, the increase of the hydrogen crossover through the membrane at high pressures on the hydrogen side, accompanied by a reduction in Faradaic efficiency is a fundamental discriminating parameter for the choice of one or the other system. In fact, from these preliminary simulations it appears that it exists a value of Faradaic efficiency loss at full load (0.2%$_{pt.}$ every 70 bar, i.e. 0.0029 %$_{pt.}$/bar) beyond which it is no more convenient to adopt high pressure electrolysis and it's better to use a compressor station to produce hydrogen at high pressure.

As it's possible to deduce from the treatment in paragraph 3.4.2 on the Faradaic efficiency, it's value is dependent on the current with a law that can be roughly described by the Eq. (3.13), which imposes that to a certain reduction in the Faradaic efficiency at full load corresponds a higher reduction at part load. In fact, Eq. (3.13) is characterized by a constant value *a* that, in the base case is assumed to be equal to 0.03113 A/cm^2. By finding the new constant that leads to the new Faradaic efficiency (at higher pressure) it is possible to find the corresponding Faradaic efficiency at part-load (Figure 4.22). In the first scenario (Faradaic efficiency loss of 0.5 %$_{pt.}$ for a

cathode pressure increase of 70 bar) the *a* coefficient increase is equal to $1.37*10^{-4}$ A/cm^2/bar while in the second scenario (Faradaic efficiency loss of 1 %$_{pt.}$ for a cathode pressure increase of 70 bar) the *a* coefficient increase is equal to $2.19*10^{-4}$ A/cm^2/bar.

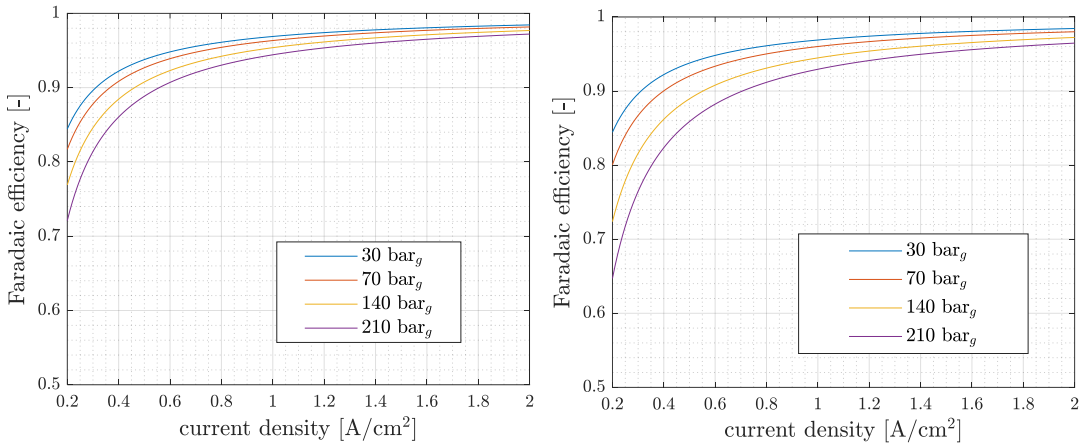

Figure 4.22 – Value of the Faradaic efficiency over the current density at different values of the pressure of the hydrogen delivered assuming a 0.5%$_{pt.}$ of Faradaic efficiency loss at full-load (figure on the left) and a 1%$_{pt.}$ of Faradaic efficiency loss at full-load (figure on the left)

The determination of the variability of the *a* coefficient allows to compare the full load operation with the part load, in fact, a realistic value of the Faradaic efficiency at all the currents can be known, availing of the same assumptions made until now. The model is run at 50% of the nominal power (31 kW) at different pressures considering the first and the second scenario for the variability of the Faradaic efficiency. On the contrary, the chiller COP and the compressor efficiency are assumed to be constant at part-load. The results are shown and compared in Figure 4.23 and reported in detail in Table 4.12 to Table 4.15. At 50% of the load, the results of the simulations show that the overall consumption of the system assuming high pressure electrolysis with constant Faradaic efficiency is almost identical to the consumption assuming the use of a compressor and electrolysis at 30 bar$_g$ while assuming a reduction of the Faradaic efficiency high pressure electrolysis results to be no longer convenient. Thus, the use of a compressor in order to reach the desired pressure becomes more convenient when operating at partial load. This is motivated by the fact that, as shown in section 3.2.1, the cell efficiency is more impacted by the pressure increase when it works with lower current densities, while the efficiency of the compressor is assumed to be constant with the load. Furthermore, as already widely discussed, the electrolyzer system efficiency strongly decreases in partial load operation, and in the computation of the specific energy consumption the electrolyzer system consumption has a lower weight when the compressor use is assumed, with respect to the case of the sole use of the electrolyzer. However, the reader is reminded that the purpose of this paragraph is not to give a definitive answer as to which strategy is best, but to determine whether there may be an interest and in which direction future research should be directed. Certainly, the answer will be case dependent and in particular will depend on technology and characteristics of the compressor and the type of use of the electrolyzer (for instance,

high number of hours of use at full load or most of time at part load etc.) and, in addition, the final assessment should also include economic considerations, including CAPEX as well as OPEX. For sure it is possible to state that producing hydrogen at high pressure directly into PEM electrolyzers is a strategy that should be furtherly investigated in future researches as it has all the characteristics of a promising strategy.

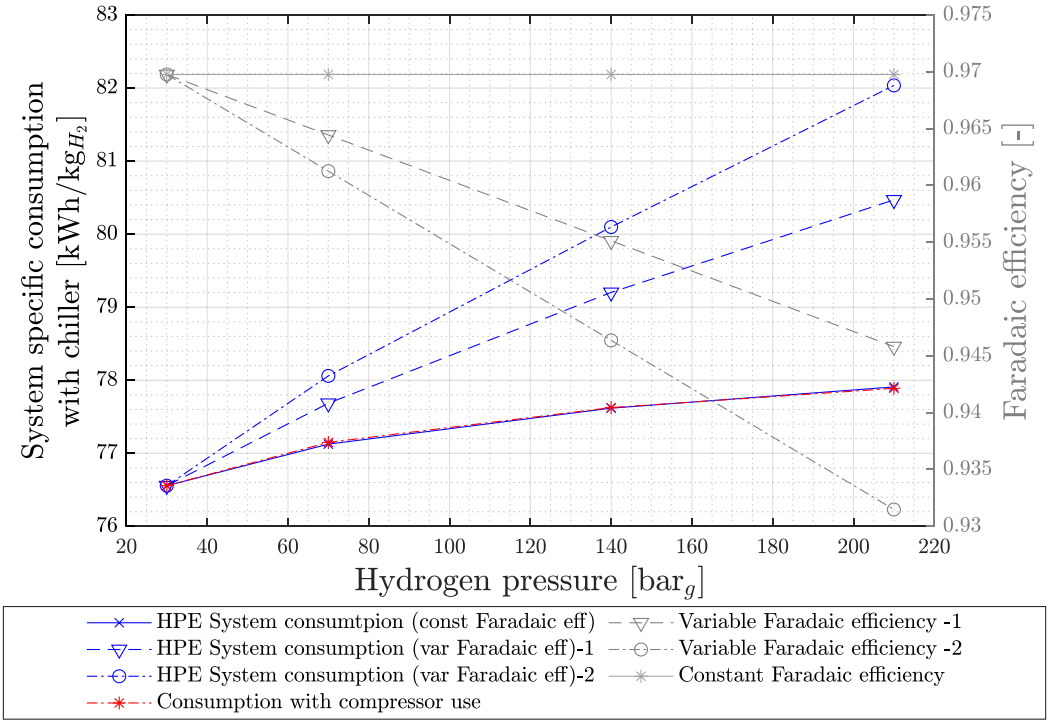

Figure 4.23 – Overall system consumption (y-axis) for producing hydrogen at different pressures (x-axis) adopting a post-compression or producing pressurized hydrogen inside the electrolyzer at part-load (50%)

Table 4.12 – System specific consumption and hydrogen production resulting from simulations at 50% of the nominal load and different cathode pressures (constant Faradaic efficiency)

H_2 delivery pressure	**System specific consumption**	**Chiller heat duty**	**Chiller consumption**	**H_2 net production**
[bar$_g$]	[kWh/kg$_{H2}$]	[kW$_{th}$]	[kW$_{el}$]	[kg/s]
30 (base case)	71.5	6.61	2.20	$1.205*10^{-4}$
70	72.0 (+0.7%)	6.75(+2.1%)	2.25	$1.197*10^{-4}$
140	72.4 (+1.3%)	6.84(+3.5%)	2.28	$1.190*10^{-4}$
210	72.6 (+1.5%)	6.89(+4.2%)	2.30	$1.186*10^{-4}$

Table 4.13 – System specific consumption and hydrogen production resulting from simulations at 50% of the nominal load and different cathode pressures

H_2 delivery pressure	**System specific consumption**	**Chiller heat duty**	**Chiller consumption**	**H_2 net production**
[bar_g]	[kWh/kg_{H2}]	[kW_{th}]	[kW_{el}]	[kg/s]
30 (base case)	71.5	6.62	2.21	$1.205*10^{-4}$
70	72.4 (+1.3%)	6.84(+3.3%)	2.28	$1.190*10^{-4}$
140	73.6 (+2.9%)	7.09(+7.1%)	2.36	$1.170*10^{-4}$
210	74.6 (+4.3%)	7.30(+10.3%)	2.43	$1.154*10^{-4}$

Table 4.14 – System specific consumption and hydrogen production resulting from simulations at 50% of the nominal load and different cathode pressures

H_2 delivery pressure	**System specific consumption**	**Chiller heat duty**	**Chiller consumption**	**H_2 net production**
[bar_g]	[kWh/kg_{H2}]	[kW_{th}]	[kW_{el}]	[kg/s]
30 (base case)	71.5	6.62	2.21	$1.205*10^{-4}$
70	72.7 (+1.7%)	6.90(+4.2%)	2.30	$1.185*10^{-4}$
140	74.3 (+3.9%)	7.24(+9.4%)	2.42	$1.159*10^{-4}$
210	75.9 (+6.2%)	7.55(+14.1%)	2.52	$1.135*10^{-4}$

Table 4.15 – Compressor and overall (electrolyzer + compressor) system consumption at different hydrogen pressures using a compressor

H_2 delivery pressure	**Compressor consumption**	**Pressure ratio**	**Chiller heat duty**	**Chiller consumption**	**H_2 net production**
[bar_g]	[kW_{el}]	[-]	[kW_{th}]	[kW_{el}]	[kg/s]
30	-	-	6.62	2.21	$1.205*10^{-4}$
70	0.197	2.3	6.81	2.27	$1.205*10^{-4}$
140	0.354	2.1	6.96	2.32	$1.205*10^{-4}$
210	0.438	1.9	7.05	2.35	$1.205*10^{-4}$

A summary of all the results on consumption obtained can be found in the Table 4.16.

Table 4.16 - Summary table containing all the consumption results in the different configurations analyzed

	kWh/kg_{H2}	**H_2 delivery pressure**			
		bar_g	bar_g	bar_g	bar_g
	$\eta_{eff,loss}$	30	70	140	210
Full load	*0.00 $\%_{pt.}$/70 bar*	74.47	74.95	75.33	75.54
	0.50 $\%_{pt.}$/70 bar	74.47	75.17	75.92	76.52
	1.00 $\%_{pt.}$/70 bar	74.47	75.38	76.53	77.53
	LPE + compressor use	74.47	75.01	75.55	75.81
50% load	*0.00 $\%_{pt.}$/70 bar*	76.56	77.12	77.62	77.91
	0.93 $\%_{pt.}$/70 bar	76.56	77.68	79.20	80.47
	1.49$\%_{pt.}$/70 bar	76.56	78.06	80.10	82.04
	LPE + compressor use	76.56	77.15	77.63	77.89

5

CHAPTER 5 – CONCLUSIONS

In the first part of this work, the dynamic model of a PEM electrolyzer has been improved, completed and validated. Improvements in the electrolysis stack model involved the electrochemical behavior of the cells, the introduction of heat losses toward the external environment, and the estimation of the stack thermal capacity. Conversely, on a system level, the main model improvements consisted in the introduction of a simplified model of the hydrogen drying system.

As for the stack model, the use of the Tafel equation in the electrochemical model to estimate the activation overpotential has been proven to be valid only for high current densities, thus it has been substituted with another expression derived from the Butler – Volmer equation, leading to a significative error reduction on the evaluation of the cell voltage at low current density. A considerable improvement in the estimation of the voltage dependence from the temperature has been obtained by introducing the variability of the exchange current density from the temperature, leading to an error reduction on the voltage particularly significant at high current densities. Overall, these changes led to a reduction of the maximum error on voltage from 13 % to 3.9 %, over the entire current and operating temperature range. Two trends have been identified in the voltage error: firstly, going towards high temperatures, the model voltage shows a slight overestimation with respect to the experimental data, while for low temperatures it is slightly underestimated, secondly, the error on the voltage presents a direct dependence with the current. Both trends suggest that there is still room for possible model improvements in the prosecution of this work. In the first case, the error is probably related to the evaluation of the activation overpotential dependence on the temperature, thus, improvements could regard the evaluation of the exchange current density, while in the second case, the error seems to lie in the evaluation of the membrane resistance to the flow of protons, probably a more accurate evaluation of the membrane thickness is needed. It should also be considered that the zero dimensional approach for the stack modelling, adopted because of the integrated system complexity, is not suitable for describing detailed internal phenomena (i.e., non-uniform distribution of flows and temperature profiles). The obtained error is considered anyway reasonable for the specific application of this model.

The validation of the polarization curves dependence on the pressure has not been possible because of the lack of data regarding the operation of the system at pressures significantly different from the rated one but, by comparison with the literature, it has been possible to determine that, even though the voltage variation with pressure is not only dependent on the open circuit voltage (OCV), but also on other factors which pressure dependence is not caught by the model, the sole OCV variation with pressure well approximates the polarization curves dependence on pressure. Anyway, a more detailed model for the computation of the concentration losses, taking into account the concentration of the chemical species at the anode and the cathode, by means of the Nernst equation, is proposed. Hydrogen crossover has been modelled by means of a simplified model of the Faradaic efficiency, thus, this phenomena has no influence in the polarization curves model. While in the first approximation, considering the sole OCV variation with pressure seems an acceptable approximation of the polarization curves behavior at different pressures, future researches are necessary in order to properly model the system behavior when variating the pressure, considered the great interest in high pressure electrolysis aiming at avoiding the use of compressors.

On a system level, the model has been proven to be able to follow dynamic loads and to simulate properly temperature and pressure transients, with a maximum error on the temperature during start-up of 3.66%, evaluated with the fitting stack thermal capacity of 165 kJ/K, and a maximum error on cathode pressurization time of 15 seconds. According to the experimental results, the simulated system performances have shown that hydrogen losses are the main source of loss during the electrolyzer operation, followed by the BoP consumption. In particular, the efficiency of the system is all the more severely impaired, the lower the operating load, mainly due to an inflexible BoP and hydrogen losses in the drying system, with a system net efficiency decaying from 57.5%, at full load operation, to 16% at minimum load (15 % of the rated power). Such a decline in performance strongly reduces the average efficiency of the system, when coupled with renewable sources, as they rarely operate at rated power. Furthermore, the intermittent nature of this sources makes it fundamental to find ways to make this system's start-up time as short as possible.

The second part of this work allowed, exploiting the validated model, to identify methods for improving the system performances when coupled with variable renewable energy sources. By delaying the oxygen – water separator refill with fresh water it was possible to reduce the system warm – up time in the range of 6 – 20 %, depending on the operating load of the system. Anyway, the benefit on the efficiency was always negligible, with increased average efficiency after one hour from the start-up always well below 1 $\%_{pt.}$. By exploiting the increase in the stack efficiency with the temperature, the hot standby, when performed with a full oxygen – water separator, has been demonstrated to be a better strategy for improving the system start-up performances, with a warm-up time reduction in the range of 16 – 28 % and an average efficiency improvement of at least 2 $\%_{pt.}$ at the end of the warm-up. Hot standby has been demonstrated to be capable of making the system operate at asymptotic average efficiency several minutes before the base case in most of cases. From a comparison

of the benefit in terms of hydrogen production increase thanks to the hot standby with the energy expenditure required for its implementation, it was possible to determine that hot standby is only convenient when the oxygen – water separator is well thermally isolated. Furthermore, the same beneficial effects of hot standby can be obtained by means of pre-heating, exploiting waste/unusable ('free') power, as a power input too low to be used for electrolyzing, to heat up (or keep hot) the oxygen – water separator tank. Taking to the extreme the concept of pre-heating, assuming for instance the possibility of using the 'free' energy source to activate the pump and pre-heat the stack too, it's been possible to evaluate the maximum potential of this strategy in terms of produced hydrogen. Results have shown that the maximum hydrogen production increase, with respect to the base case, during the warm-up standard period, ranged from 9% to 13%, depending on the load.

By implementing a flexible regeneration of the PSA beds , introducing a valve in order to control the hydrogen purge flow to the minimum needed for regeneration, the system net consumption at partial load has been notably improved, reaching a 38% reduction when the system is operated at 20% of the rated power. Another strategy for the reduction of the hydrogen losses connected to the drying system has been identified in the flexible switching of the adsorption beds, by implementing a dynamic control of the time between one regeneration and the other based on the evaluation of the saturation level of the active bed (i.e., without the need to make any changes to the system). This measure alone has been demonstrated to allow a reduction in the system net consumption at partial load up to 10% (evaluated at 20% of the nominal power). Since these two strategies can be implemented independently, their combination can lead to a reduction in system net consumption up to 42%, corresponding to a 76% of the maximum potential efficiency improvement achievable by reducing hydrogen losses in the drying system.
Efforts to optimize the consumption of the BoP components at partial load focused on the centrifugal pump that controls the flow of water supplied to the stack, as it accounts for the 80% of the auxiliaries components electrical consumption. By the introduction of a variable speed pump, regulating the stack feed-in water mass flow rate on the basis of the stack current, it is possible to reduce the pump consumption and to keep, at the same time, water utilization factor and oxygen concentration at the anode below the design value. The benefit has been quantified as a reduction in consumption up to 28%, but it may not be convenient if the system is operated mainly between 50% and 100% of the nominal power, as its benefit is low in this load range. Thus, the replacement of the fixed speed pump with a variable speed pump must be the result of a trade-off taking into account the cost of the variable speed pump and the typical load at which the system will be operated.

Finally, high pressure operation has been investigated. The system consumption to deliver hydrogen at 70, 140 and 210 bar_g has been evaluated. Two scenarios were assessed: the production of hydrogen at delivery pressure directly within the electrolyzer, and the production at 30 bar_g with subsequent compression up to delivery pressure by means of an inter-refrigerated displacement compressor. The results at full

load have shown a higher efficiency when producing hydrogen at delivery pressure directly in the electrolyzer, but only for very limited Faradaic efficiency losses, up to a 0.2 %pt. loss every 70 bar of pressure increase. The advantage in producing pressurized hydrogen directly in the electrolyzer reduces progressively with the load, because of the higher cell efficiency loss caused by the pressure increase at low load, and due to the higher weight of the electrolyzer consumption on the overall consumption evaluation with respect to the case with compressor use, as the compressor is assumed to operate at constant efficiency. Below the 50% of the net power input, it results to be more convenient to post-compress the hydrogen into the compressor at any of the delivery pressures studied, even in the hypothesis of no Faradaic efficiency loss. Clearly, this break-even point is higher than 50% if considering the effects of the pressure increase, leading to increased hydrogen crossover through the membrane, negatively impacting the Faradaic efficiency.

It is possible to conclude that the convenience of high-pressure electrolysis over post-compression is highly case dependent, and the evaluation must take into account the characteristics of the compressor, the Faradaic efficiency decay with pressure and the typical load at which the system is forecasted to operate. In particular, the Faradaic efficiency has been shown to be a fundamental parameter to be taken into account when the pressure of the system varies. Therefore, possible future developments of this work could be the modelling of the behavior of the polarization curves at different pressures and the modelling and validation of the faradaic efficiency dependence on the pressure.
It also emerges to be of fundamental importance that electrolysis system designers take into account the use that will be made of their systems when designing the BoP components and the membrane. Not all the BoP components improvements proposed in this work might be convenient: the efficiency improvements if the system is operated mainly at high loads might not justify the investment increase, a trade-off must be done. Likewise, a thicker membrane means greater ohmic losses, leading to lower efficiency at high loads, but higher efficiency at low load, due to reduced hydrogen crossover through the membrane. Vice versa, a thinner membrane leads to higher efficiency when the system operates at high load, but low partial load efficiency.

BIBLIOGRAPHY

[1] International Energy Agency, “Renewables 2019 - Analysis and forecast to 2024,” 2019.

[2] O. M. Babatunde, J. L. Munda, and Y. Hamam, “Power system flexibility: A review,” *Energy Reports*, vol. 6, pp. 101–106, 2020, doi: 10.1016/j.egyr.2019.11.048.

[3] European Parliament, *European Parliament Resolution of May 19th (2021) on an European strategy for hydrogen*, no. 3. EU, 2021, p. 6.

[4] T. D. Hutty, S. Dong, and S. Brown, “Suitability of energy storage with reversible solid oxide cells for microgrid applications,” *Energy Convers. Manag.*, vol. 226, no. May, p. 113499, 2020, doi: 10.1016/j.enconman.2020.113499.

[5] J. M. Stansberry and J. Brouwer, “Experimental dynamic dispatch of a 60 kW proton exchange membrane electrolyzer in power-to-gas application,” *Int. J. Hydrogen Energy*, vol. 45, no. 16, pp. 9305–9316, 2020, doi: 10.1016/j.ijhydene.2020.01.228.

[6] P. Olivier, C. Bourasseau, and P. B. Bouamama, “Low-temperature electrolysis system modelling: A review,” *Renew. Sustain. Energy Rev.*, vol. 78, no. May, pp. 280–300, 2017, doi: 10.1016/j.rser.2017.03.099.

[7] M. Ni, M. K. H. Leung, and D. Y. C. Leung, “Energy and exergy analysis of hydrogen production by a proton exchange membrane (PEM) electrolyzer plant,” *Energy Convers. Manag.*, vol. 49, no. 10, pp. 2748–2756, 2008, doi: 10.1016/j.enconman.2008.03.018.

[8] T. Thampan, S. Malhotra, J. Zhang, and R. Datta, “PEM fuel cell as a membrane reactor,” *Catal. Today*, vol. 67, no. 1–3, pp. 15–32, 2001, doi: 10.1016/S0920-5861(01)00278-4.

[9] B. Yodwong, D. Guilbert, M. Phattanasak, W. Kaewmanee, M. Hinaje, and G. Vitale, “Faraday’s efficiency modeling of a proton exchange membrane electrolyzer based on experimental data,” *Energies*, vol. 13, no. 18, pp. 1–14, 2020, doi: 10.3390/en13184792.

[10] R. G. Cunningham, “Orifice Meters with Supercritical Compressible Flow.” pp.

625–638, 1951.

[11] "UC Irvine injects P2G green hydrogen into campus power supply," *Fuel Cells Bulletin*, vol. 2017, no. 1, p. 10, 2017.

[12] M. Santarelli, P. Medina, and M. Calì, "Fitting regression model and experimental validation for a high-pressure PEM electrolyzer," *Int. J. Hydrogen Energy*, vol. 34, no. 6, pp. 2519–2530, 2009, doi: 10.1016/j.ijhydene.2008.11.036.

[13] C. March and S. E. E. L. Page, "Corrected 18 march 2011; see last page," no. October 2010, pp. 356–360, 2011.

[14] "Global Energy Review 2020," *Glob. Energy Rev. 2020*, 2020, doi: 10.1787/a60abbf2-en.

[15] IEA, "Outlook for biogas and biomethane. Prospects for organic growth. World Energy Outlook Special Report.," p. 93, 2020.

[16] International Energy Agency, "Status of Power System Transformation 2018 - Advanced Power Plant Flexibility," *Status Power Syst. Transform. 2018*, 2018, [Online]. Available: https://doi.org/10.1787/9789264302006-en.

[17] California Hydrogen Business Council, "Power-to-Gas : The Case for Hydrogen," *White Pap.*, pp. 1–17, 2015.

[18] European Commission, "European Clean Hydrogen Alliance | Internal Market, Industry, Entrepreneurship and SMEs," pp. 1–2, 2020, [Online]. Available: https://ec.europa.eu/growth/industry/policy/european-clean-hydrogen-alliance_en.

[19] IRENA, "Power-to-X solutions," *Innov. Landsc. a renewable-powered Futur. Solut. to Integr. Var. renewables*, pp. 1–8, 2019, [Online]. Available: https://irena.org/-/media/Files/IRENA/Agency/Topics/Innovation-and-Technology/IRENA_Landscape_Solution_11.pdf?la=en&hash=2BE79AC597ED18A96E5415942E0B93232F82FD85.

[20] F. R. Bianchi and B. Bosio, "Operating principles, performance and technology readiness level of reversible solid oxide cells," *Sustain.*, vol. 13, no. 9, 2021, doi: 10.3390/su13094777.

[21] R. d'Amore-Domenech, Ó. Santiago, and T. J. Leo, "Multicriteria analysis of seawater electrolysis technologies for green hydrogen production at sea," *Renew. Sustain. Energy Rev.*, vol. 133, no. July, 2020, doi: 10.1016/j.rser.2020.110166.

[22] ITM Power, "Hydrogen Refuelling Infrastructure," no. February, p. 30, 2017,

[Online]. Available: http://www.level-network.com/wp-content/uploads/2017/02/ITM-Power.pdf.

[23] S. P. S. Badwal, S. S. Giddey, C. Munnings, A. I. Bhatt, and A. F. Hollenkamp, "Emerging electrochemical energy conversion and storage technologies," *Front. Chem.*, vol. 2, no. SEP, pp. 1–28, 2014, doi: 10.3389/fchem.2014.00079.

[24] M. Carmo, D. L. Fritz, J. Mergel, and D. Stolten, "A comprehensive review on PEM water electrolysis," *Int. J. Hydrogen Energy*, vol. 38, no. 12, pp. 4901–4934, 2013, doi: 10.1016/j.ijhydene.2013.01.151.

[25] A. Buttler and H. Spliethoff, "Current status of water electrolysis for energy storage, grid balancing and sector coupling via power-to-gas and power-to-liquids: A review," *Renew. Sustain. Energy Rev.*, vol. 82, no. February 2017, pp. 2440–2454, 2018, doi: 10.1016/j.rser.2017.09.003.

[26] D. Bessarabov, H. Wang, H. Li, and N. Zhao, *PEM Electrolysis for Hydrogen Production*. CRC Press, 2016.

[27] S. A. Grigoriev, V. I. Porembskiy, S. V. Korobtsev, V. N. Fateev, F. Auprêtre, and P. Millet, "High-pressure PEM water electrolysis and corresponding safety issues," *Int. J. Hydrogen Energy*, vol. 36, no. 3, pp. 2721–2728, 2011, doi: 10.1016/j.ijhydene.2010.03.058.

[28] European Energy Research Alliance, "Joint Research Programme on Research Grouping of the Fuel Cells and Hydrogen Joint Undertaking (FCH JU)," pp. 2020–2030, 2020.

[29] IRENA, *Global energy transformation: A roadmap to 2050 (2019 edition)*. 2019.

[30] F. Alshehri, V. G. Suárez, J. L. Rueda Torres, A. Perilla, and M. A. M. M. van der Meijden, "Modelling and evaluation of PEM hydrogen technologies for frequency ancillary services in future multi-energy sustainable power systems," *Heliyon*, vol. 5, no. 4, 2019, doi: 10.1016/j.heliyon.2019.e01396.

[31] IEA, "The Future of Hydrogen," *Futur. Hydrog.*, no. June, 2019, doi: 10.1787/1e0514c4-en.

[32] IRENA, *Green Hydrogen Cost Reduction: Scaling up Electrolysers to Meet the 1.5 C Climate Goal*. 2020.

[33] D. Fraile, J.-C. Lanoix, P. Maio, A. Rangel, and A. Torres, "Overview of the market segmentation for hydrogen across potential customer groups, based on key application areas," 2015.

[34] "IEA (2020), Hydrogen, IEA, Paris." https://www.iea.org/reports/hydrogen.

[35] O. Schmidt, A. Gambhir, I. Staffell, A. Hawkes, J. Nelson, and S. Few, "Future cost and performance of water electrolysis: An expert elicitation study," *Int. J. Hydrogen Energy*, vol. 42, no. 52, pp. 30470–30492, 2017, doi: 10.1016/j.ijhydene.2017.10.045.

[36] C. Wulf, P. Zapp, and A. Schreiber, "Review of Power-to-X Demonstration Projects in Europe," *Front. Energy Res.*, vol. 8, no. September, pp. 1–12, 2020, doi: 10.3389/fenrg.2020.00191.

[37] "H2FUTURE Green Hydrogen Project." https://www.h2future-project.eu/news.

[38] "REFHYNE – Clean Refinery Hydrogen for Europe." https://refhyne.eu/.

[39] "CORDIS - Clean Refinery Hydrogen for Europe/REFHYNE project." https://cordis.europa.eu/project/id/779579/it.

[40] "RECHARGE News, World's largest green-hydrogen plant inaugurated in Canada by Air Liquide." https://www.rechargenews.com/transition/worlds-largest-green-hydrogen-plant-inaugurated-in-canada-by-air-liquide/2-1-952085.

[41] "Climate Council." https://www.climatecouncil.org.au/south-australia-hits-50-as-the-march-to-renewables-continues/.

[42] Governemnt of South Australia, "Eyre Peninsula Gateway Project." http://www.renewablessa.sa.gov.au/topic/hydrogen/hydrogen-projects-south-australia/hydrogen-green-ammonia-production-facility.

[43] "Hybridge project plan." https://www.hybridge.net/Project/Plan/.

[44] E. Crespi, S. Molho, G. Guandalini, and S. Campanari, "Dynamic modelling and simulations of a PEM electrolysis system for flexible operation," in *Proceedings EFCF 2021, Low-Temperature Electrolysers, Fuel Cells & H2 Processing*, 2021, pp. 175–184, [Online]. Available: www.Zenodo.org.

[45] V. Liso, G. Savoia, S. S. Araya, G. Cinti, and S. K. Kær, "Modelling and experimental analysis of a polymer electrolyte membrane water electrolysis cell at different operating temperatures," *Energies*, vol. 11, no. 12, 2018, doi: 10.3390/en11123273.

[46] W. Wagner and A. Pruss, "International Equations for the Saturation Properties of Ordinary Water Substance. Revised According to the International Temperature Scale of 1990," *J. Phys. Chem. Ref. Data*, vol. 22, no. 3, 1993, doi: 10.1063/1.555926.

[47] T.E. Springer, "Polymer Electrolyte Fuel Cell," *J. Electrochem. Soc.*, vol. 138,

no. 8, p. 2334, 1991, doi: 10.1149/1.2085971.

[48] Z. Abdin, C. J. Webb, and E. M. Gray, "Modelling and simulation of a proton exchange membrane (PEM) electrolyser cell," *Int. J. Hydrogen Energy*, vol. 40, no. 39, pp. 13243–13257, 2015, doi: 10.1016/j.ijhydene.2015.07.129.

[49] D. B. and P. Millet, *PEM Water Electrolysis*. 2017.

[50] H. Görgün, "Dynamic modelling of a proton exchange membrane (PEM) electrolyzer," *Int. J. Hydrogen Energy*, vol. 31, no. 1, pp. 29–38, 2006, doi: 10.1016/j.ijhydene.2005.04.001.

[51] P. Medina and M. Santarelli, "Analysis of water transport in a high pressure PEM electrolyzer," *Int. J. Hydrogen Energy*, vol. 35, no. 11, pp. 5173–5186, 2010, doi: 10.1016/j.ijhydene.2010.02.130.

[52] S. Dutta, S. Shimpalee, and J. W. Van Zee, "Numerical prediction of mass-exchange between cathode and anode channels in a PEM fuel cell," *Int. J. Heat Mass Transf.*, vol. 44, no. 11, pp. 2029–2042, 2001, doi: 10.1016/S0017-9310(00)00257-X.

[53] F. Marangio, M. Santarelli, and M. Calì, "Theoretical model and experimental analysis of a high pressure PEM water electrolyser for hydrogen production," *Int. J. Hydrogen Energy*, vol. 34, no. 3, pp. 1143–1158, 2009, doi: 10.1016/j.ijhydene.2008.11.083.

[54] D. Grazia and I. Fabio, *Lezioni di Fisica Tecnica Trasmissione del calore*. 2001.

[55] R. Fernández-Prini, J. L. Alvarez, and A. H. Harvey, "Henry's constants and vapor-liquid distribution constants for gaseous solutes in H2O and D2O at high temperatures," *J. Phys. Chem. Ref. Data*, vol. 32, no. 2, pp. 903–916, 2003, doi: 10.1063/1.1564818.

[56] J. Cooper and R. Dooley, "Guideline on the Henry's Constant and Vapor-Liquid Distribution Constant for Gases in H2O and D2O at High Temperatures," *Int. Assoc. Prop. Water Steam*, no. September, pp. 1–19, 2008, [Online]. Available: http://www.iapws.org/relguide/seawater.pdf%5Cnhttp://www.iapws.org/relguide/Obsolete/kd.pdf%5Cnhttp://scholar.google.com/scholar?hl=en&btnG=Search&q=intitle:Release+on+the+IAPWS+Formulation+2008+for+the+Thermodynamic+Properties+of+Seawater#0.

[57] The Linde Group, "Hydrogen Recovery by Pressure Swing Adsorption," *Engineering*, pp. 4–8, 2010.

[58] B. Han, S. M. Steen, J. Mo, and F. Y. Zhang, "Electrochemical performance modeling of a proton exchange membrane electrolyzer cell for hydrogen energy," *Int. J. Hydrogen Energy*, vol. 40, no. 22, pp. 7006–7016, 2015, doi:

10.1016/j.ijhydene.2015.03.164.

[59] ScienceDirect, “The Basic Properties of Building Materials,” 2011.

[60] B. Bensmann, R. Hanke-Rauschenbach, I. K. Peña Arias, and K. Sundmacher, “Energetic evaluation of high pressure PEM electrolyzer systems for intermediate storage of renewable energies,” *Electrochim. Acta*, vol. 110, pp. 570–580, 2013, doi: 10.1016/j.electacta.2013.05.102.

[61] M. Schalenbach, M. Carmo, D. L. Fritz, J. Mergel, and D. Stolten, “Pressurized PEM water electrolysis: Efficiency and gas crossover,” *Int. J. Hydrogen Energy*, vol. 38, no. 35, pp. 14921–14933, 2013, doi: 10.1016/j.ijhydene.2013.09.013.

[62] M. Bernt, J. Schröter, M. Möckl, and H. A. Gasteiger, “Analysis of Gas Permeation Phenomena in a PEM Water Electrolyzer Operated at High Pressure and High Current Density,” *J. Electrochem. Soc.*, vol. 167, no. 12, p. 124502, 2020, doi: 10.1149/1945-7111/abaa68.